Aramco

Journal of Technology

FALL 2022

The *Aramco Journal of Technology* is published quarterly by the Saudi Arabian Oil Company, Dhahran, Saudi Arabia, to provide the company's scientific and engineering communities a forum for the exchange of ideas through the presentation of technical information aimed at advancing knowledge in the hydrocarbon industry.

Editor

William E. Bradshaw
william.bradshaw.1@aramco.com.sa
tel: +966-013-876-0498

Production Coordination

Richard E. Doughty
Corporate Publications, Aramco Americas

Design

Graphic Engine Design Studio
Austin, Texas, U.S.A.

The *Aramco Journal of Technology* gratefully acknowledges the assistance, contribution and cooperation of numerous operating organizations throughout the company.

ISSN 1319-2388

Contents

Colloidal NaSil Squeeze Operation to Successfully Isolate Water Zone in Horizontal Well

Dr. Ayman M. Al-Mohsin, Mohamed H. Sherief, Mohammed I. Alabdrabalnabi and Ahmad Muhammad

Abstract /

Various chemical solutions have been historically used to address undesired water or gas production from oil producing wells. Among such solutions is colloidal silica, which has been field-tested for water shut-off applications with a variable success rate. Nowadays, colloidal silica nanoparticles (NaSil) are considered to be a good in-suite agent for overcoming the limitations associated with rival water shut-off chemicals, thereby addressing the challenges related to reservoir engineering problems such as unwanted water production.

This article will discuss in detail the steps of developing a water shut-off technology from lab-scale to a successful field implementation. Via the synergies of the reservoir engineering knowledge, diagnostic workflow, and historical treatments coupled with the service company's treatment engineering technologies and local ability to deploy and enhance existing chemical shut-off fluids, we exercised a systematic evaluation of a new methodology using our novel NaSil as a water shut-off chemical agent in a horizontal well.

The fluid optimization in the lab, the process of candidate well selection, and the treatment job designs will be presented. A systematic approach was implemented to assess the previous unsuccessful experiences reported in the literature, and therefore, proposing adjustments to conventional treatments using a NaSil-based water shut-off fluid system for water control. The objective of this work is to selectively squeeze NaSil particles with coil tubing (CT) units in a horizontal well, and to partially or totally seal inflow control devices (ICD) with water dominance flow profile. This process was successfully implemented in the field based on the NaSil's unique thermal properties by fine-tuning the gelation time — pumping rate, stage volumes, and total pumping duration.

The new trend of using eco-friendly chemicals in water control applications is a breakthrough in the oil industry. This emphasizes the significant role of nanotechnology because it can help minimize unwanted fluids from producing wells, and subsequently meet the oil production target.

Introduction

Horizontal wells can typically attain five to 10 times productivity over vertical wells[1]. Horizontal wells may possibly decrease coning tendencies in reservoirs with bottom water of low-pressure drawdown near the wellbore[2, 3]. Nevertheless, this advanced technology has encountered some challenges due to reservoir heterogeneity as flowing in an elongated wellbore may lead to an uneven pressure drop from heel to toe, which can cause uneven fluid entry along the horizontal section of the wellbore, Fig. 1.

In the 1990s, the wide application of the Hele-Shaw 2D model helped to experimentally investigate the performance of horizontal wells in reservoirs with bottom water. Permadi's (1995)[4] (1997)[5] research revealed that water cresting will present at the heel of the horizontal segment; then it would gradually move toward the toe. To control unwanted water in horizontal wells, mechanical inflow control devices (ICD) were developed to equalize reservoir inflow along the interval of the horizontal wellbore[6].

The ICD is mounted as part of the well completion and is usually paired with the zonal isolation packer. In the past decades, there have been exertions of using multiple inflow equalizer designs that proved the ability of this technology to delay water breakthrough. Consequently, this technology fails to deal with a breakthrough such as depicted in Fig. 2, where oil production is impaired by water breaking into the middle section of the horizontal wellbore.

Therefore, controlling and eliminating unwanted water influx into oil or gas wells is one of the major objectives in the petroleum industry. Water shut-off techniques can generally be categorized into two main groups: mechanical and chemical methods. The mechanical methods are known to be most appropriate for wellbore related problems. The most common mechanical water shut-off used in the industry may include but not be limited to mechanical plugs and packers, patches, cement and/or sand[7]. Chemical methods on the other hand have been traditionally used to remediate reservoir or formation character issues related to heterogeneity.

Typically, a slurry is squeezed into the formation to form a gel at formation temperature blocking the water

Fig. 1 *The irregular pressure drawdown along the horizontal wellbore (heel to toe effect).*

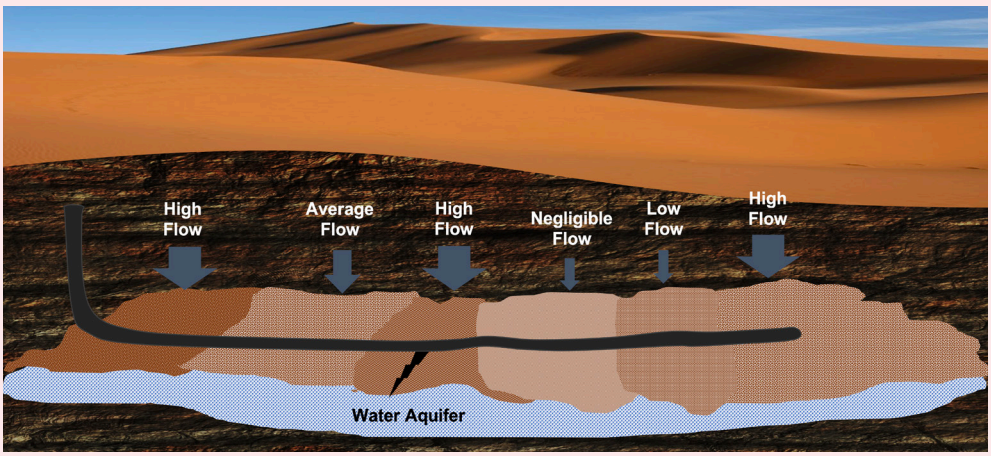

Fig. 2 *The inflow profile of a horizontal well, completed with an ICD, with water encroachment.*

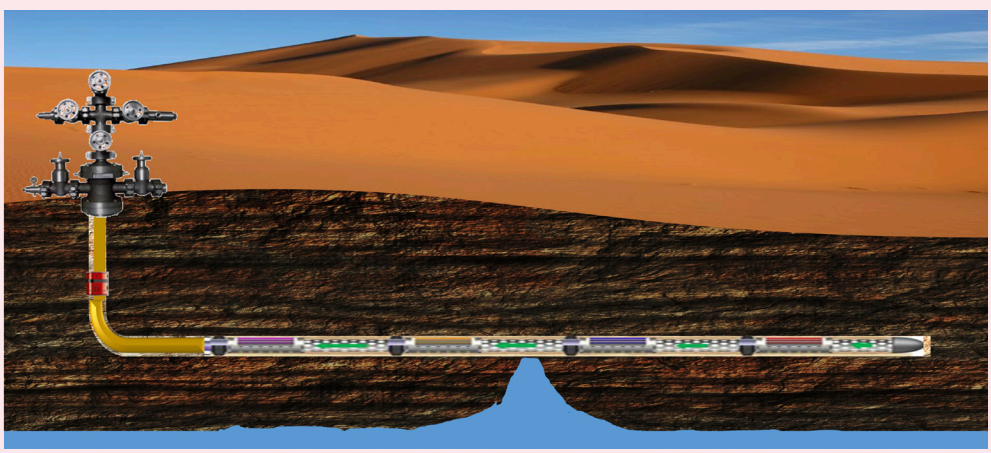

influx. The appropriate identification of the water producing source and the mechanism by which it breaks through the wellbore plays a significant role to the success of the treatment. In 1998, Baylocq et al. (1998)[8] pointed out that the worldwide success rate is roughly 55% to 60% due to poor candidate selection, inadequate gelation, or failure to place the gel at the correct wellbore location.

Nowadays, nanotechnology applications are becoming more popular in the petroleum industry. Silica nanoparticles (NaSil) have morphological characteristics and high surface area, enabling superb plugging of pore throats. Almohsin et al. (2018)[9] showed promising results using silicon dioxide nanoparticles along with aluminum dioxide nanoparticles on emulsion stability utilized for EOR applications. Another major application of NaSil is to improve the gas production of gas wells suffering from condensate banking in retrograde gas condensate reservoirs. A nanosilica-based fluid system has shown promising results, including controllable gelation time, low initial viscosity; and therefore, deep penetration into the reservoir with excellent pressure resistance[10, 11].

This article presents a novel rigless water shut-off application with NaSil applied to the middle section of a horizontal wellbore completed with an ICD. First, a novel colloidal NaSil-based aqueous solution was developed. When NaSil is combined with hydrolysable esters, it slowly hydrolyzes into corresponding alcohols and carboxylic acids, which will gel the NaSil particles at formation temperature. The developed system can be squeezed into the target formation zone as a single fluid with low initial viscosity. Under formation conditions, the activator will initiate the gelation of NaSil and plug the targeted zone. Second, the target zone was identified. Third, the effect

of the type and/or the concentration of the activator was experimentally studied at the target zone near an exact range of temperatures. The optimum chemical formulation was then yard tested to compare in situ gel strength development with experimental results from previous steps prior to actual field treatment. As a result of this elaborate workflow, the oil production conformance across the wellbore was regained right after the treatment.

NaSil Development

This article consists of research using NaSil; the new developed fluid system is an inorganic gel-based system. It could be used for water shut-off application with temperatures up to 350 °F. To develop a proper water shut-off treatment for such conditions, fluids should have the following design parameters: be environmentally friendly, have initial low viscosity for good injectivity, a controllable gelation time, the ability to withstand high temperatures, and be able to hold differential pressure for a long time.

Having a nanometric particle size (14 nm) and a low viscosity (usually < 10 cP), the NaSil fluid could easily penetrate the pore matrix of the formation that is producing unwanted water, where they undergo physical transformation from a solids-free squeezable liquid to a highly viscous or rigid material.

Figure 3 is a schematic representation of the gelling process. The fluid system presented in this article comprises two components: modified NaSil particles and an activator. It is easy to pump as a single low viscosity solution, and upon placing it into the targeted zones, the gelation process is activated/triggered by the formation temperature and time. By varying the concentration of the activator, the gelation could be delayed to allow sufficient working time for placement operation.

Some of the main highlights and benefits of the novel nanosilica technology:

- The ability to customize the thermal and rheological properties of nanosilica to fit the purpose of treatment from partial impairment to full annular isolation as well as fracture bridging.
- A wide temperature application ranging from ambient up to 350 °F.
- A low viscosity solution into the targeted formation zones (5 cP).
- A tough gel formed after curing — tested on both matrix and fracture that can withstand more than 5,000 psi.
- A fast, safe, and cost-effective novel deployment method invented based on this proprietary chemical to eliminate risk of getting stuck in-hole during the operations compared to rival technologies.
- An eco-friendly fluid and 100% reversible.

Lab Experiments

Materials

Aqueous dispersion of NaSil contains approximately 40 wt% solids. The NaSil dispersion is sterically stabilized and the amorphous silica nanoparticles carry a negative surface charge. Those silica nanoparticles are discrete, and have a smooth, spherical shape. A FPIA-3000 (Malvern) particle size analyzer was used to determine the particle size distribution of NaSil, Fig. 4. The water shut-off system based on the new composition incorporates two main components: NaSil and the temperature activated activator.

Gelation Time Study

The fundamental definition of "gelling time" is that the transformation of an ideal liquid solution to a state of solid gel. A reasonable "gelation time" must be comprehended to permit safe pumping operation of the fluid through the tubular and into the target zone at the desired depth of penetration. In this study, we used a high-pressure, high temperature (HPHT) viscometer by observing the drastic change in solution viscosity during measurement. This method is more precise and dependable and was adapted for use in this study.

Figure 5 shows the viscosity time curve used in measuring the "gelation time" of the fluid and the picture of a completely gelled NaSil-based fluid system. The

Fig. 3 *A schematic representation of the gelation process for the NaSil system.*

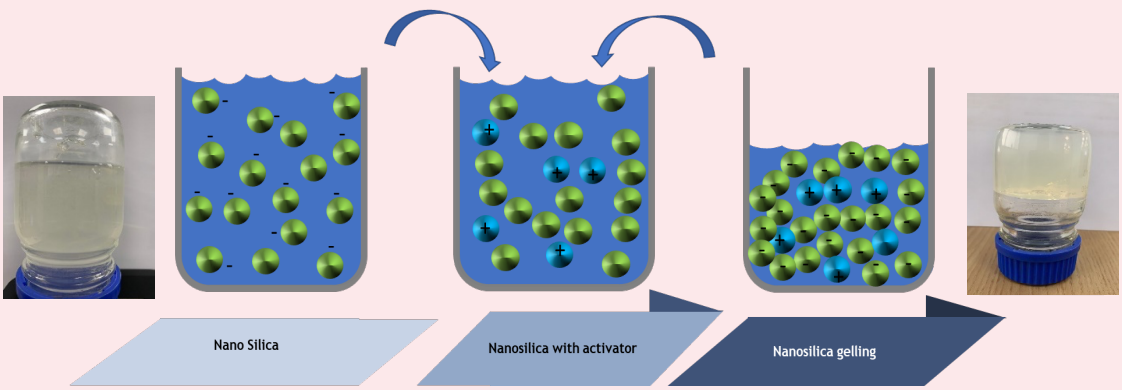

Fig. 4 *The nanoparticle characterization using the Sysmex FPIA-3000 (Malvern) nanoparticle distribution analyzer.*

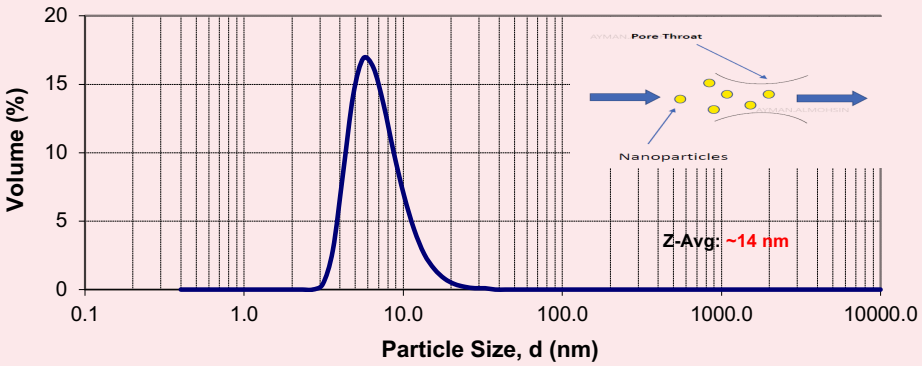

Fig. 5 *The typical gelation time curve for the for NaSil system using a viscometer (at 180 °F).*

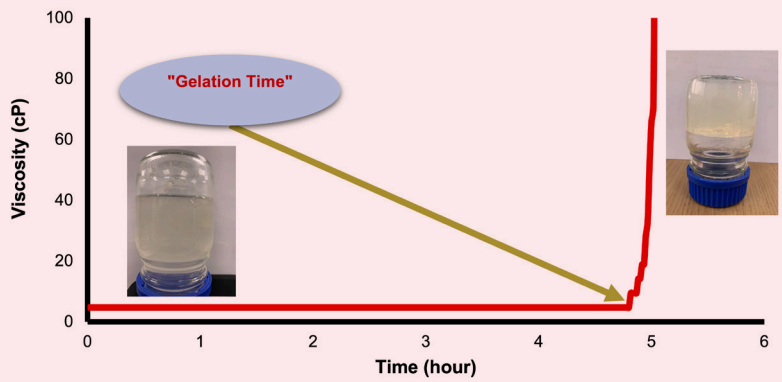

sample viscosity changes were monitored as a function of time at a given constant shear rate.

Coreflood Study

A core flow test was implemented to evaluate the injectivity of the treatment into the formation and the ability of the NaSil fluid system for water shut-off application. To achieve that, the coreflooding experiments were run in different modes of operation, Fig. 6. In the first stage, the injectivity was measured using the pre-flush fluid containing the clay surfactant at a constant flow rate. This was followed with the main treatment injection containing the NaSil-based fluid system with close monitoring of the pressure drop across the core.

Following that, the coreflooding was stopped to allow the chemical to cure and build the required mechanical strength for several hours. The initial injectivity after the chemical curing is to assess the ability to shut-off the treated matrix. This was followed with endurance testing by exposing the core plug to high differential pressure for an extended period to ensure that the shut-off material will not fatigue with time. The pre-flush fluid was used to measure initial injectivity and endurance testing after curing.

Breaker Tests

In case the water shut-off gel is solidified in the wellbore, a contingency plan has to be made to break the gel system. Therefore, we deliberate the ability to break the NaSil gel system at a fixed reservoir temperature equivalent to 210 °F. We prepared and optimized breaker solutions by dissolving non-damaging breaker particles in field water at varied breaker concentrations.

Yard Test

The objective of this test was to evaluate the designed and up-scaled treatment from the batch mixer to the lab-scale formulation. Yard testing was essential to gauge the required time to mix NaSil to get a quality mixture that matches the experimental data. This will assist in designing the pumping schedule.

Lab Test Results and Discussions

Gelation Time Test

One of the key parameters in a water shut-off operation, specifically for in situ gels, is the gelation time (setting time). During water shut-off injection into a targeted zone, the reservoir temperature will be significantly reduced and influence the treatment gelation time,

Fig. 6 *A schematic of the coreflooding experiment.*

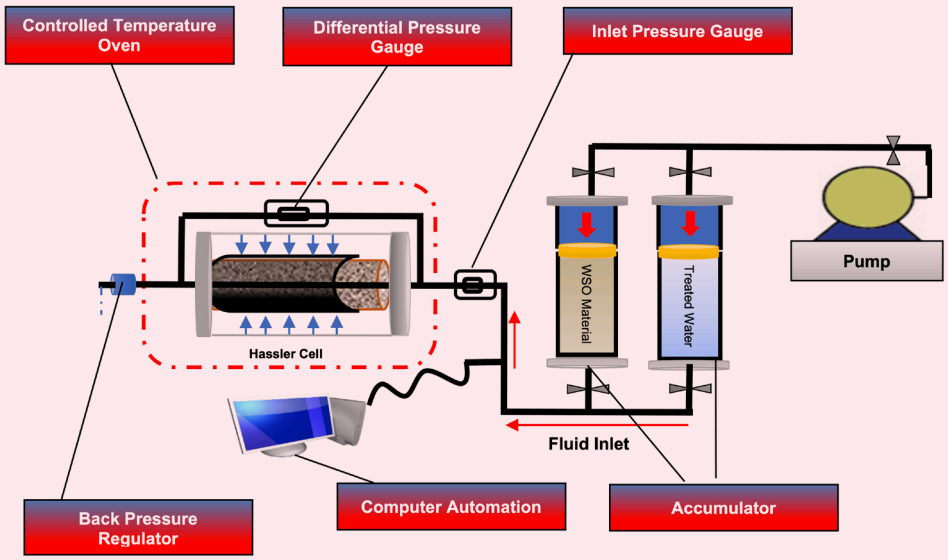

where the temperature reduction is more pronounced at a higher rate and volume.

The gelation time depends on two main factors for this nanofluid system: (1) temperature, and (2) activator. The gelation time can be tuned from minutes to several hours, or even days by varying the activator concentration and temperature. Figure 7 exhibits the variations in the gelation time of different fluid samples with respect to different temperatures: 140 °F, 160 °F, 170 °F, 180 °F, 190 °F, and 200 °F, respectively. Also seen in Fig. 7, the gelation time for a definite system, i.e., a system with a concentration of 25% activator, decreases with an increasing temperature. The higher the temperature, the lower the zeta potential of the system.

Consequently, the colloidal system becomes less stable and the gelation process is activated. Figure 8 depicts the viscosity vs. time for different formulations at 200 °F. The change in activator concentration greatly affects the gelation time. As can be seen with the same NaSil, as the activator concentration increased from 22.5% to 25% and 30%, the gelation time decreased from ~500 minutes to 140 minutes and 50 minutes, respectively. The shortest gelation time occurred within ~25 minutes using 40% of activator concentration.

Coreflooding Studies

Matrix Injectivity and Chemical Injection

A limestone outcrop plug having 24% porosity was used in this work. The absolute permeability, pore

Fig. 7 *The effect of temperature on the gelation time of different NaSil fluid samples.*

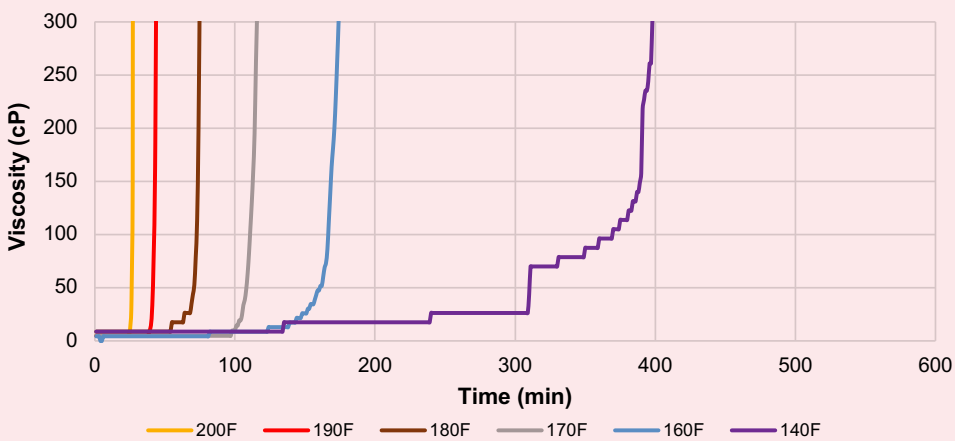

Fig. 8 *The effect of activator concentration on gelation time.*

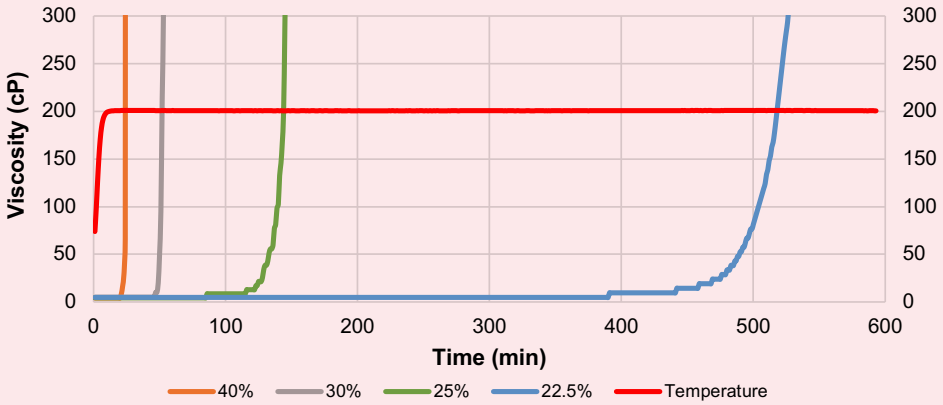

Fig. 9 *The matrix injectivity and chemical injection flow test.*

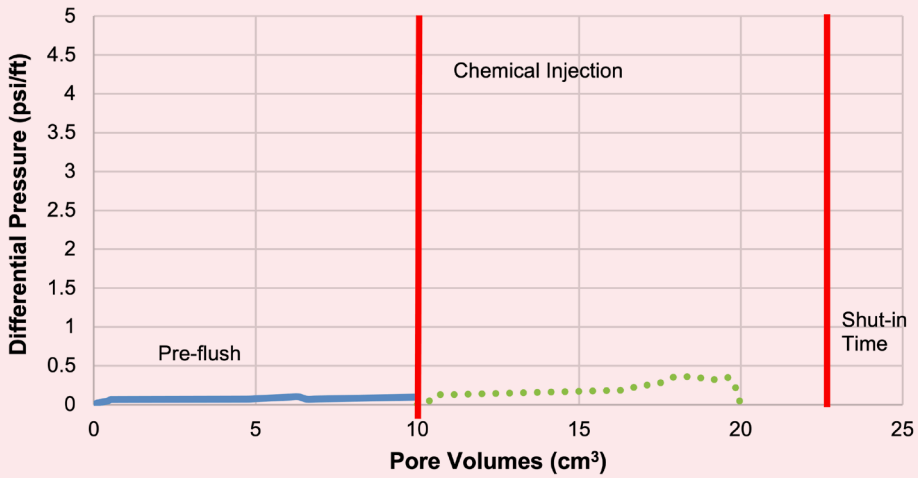

volume (PV), and porosity of the core were determined by routine core analysis. A surfactant was added as pre-flush to pre-condition the reservoir and improve injectivity of the water shut-off material. Porous media tests are essential for laboratory determination of the NaSil system's injectivity.

Figure 9 shows the matrix injectivity outcome for a 1½" diameter and a 3½" length limestone outcrop core, with a 25 ml PV and 2,400 mD absolute liquid permeability. The NaSil fluid system consists of 77.5 wt% NaSil and 22.5 wt% activator at 7 hours gelation time, which was injected at a 1 ml/min rate at 210 °F. During this stage, 10 PV of the NaSil fluid system was injected in 4.2 hours, with little increase in injection pressure, 0.35 psi. This indicated fluid propagation into the porous media without injectivity issues.

Endurance Test (Extended Constant Pressure Test)

After a water shut-off system was injected, the flow test was ceased for curing time — 30 hours. Then, the treated water was then injected to evaluate the performance of the NaSil for water shut-off applications. Figure 10 illustrates the pressure drop measurements through different stages with respect to time. As can be seen in the figure, there was a drastic increase in injection pressure with a total differential pressure of 500 psi at the primary injectivity test once the chemical became gelled. The measured differential pressure is corresponding to 1,714.3 psi/ft holding pressure for the treated matrix by this water shut-off material.

Then, the endurance test, initiated at a constant differential pressure, held at 480 psi for 18.5 hours. Furthermore, the pressure was gradually increased by adjusting the pump until we reached almost ~3,000 psi. This was followed with a prolonged period of 317 hours at a differential pressure of 3,000 psi with minimal leakoff through the treated core plug. The averaged measured leakoff rate during this period was 0.0018 cm^3/min.

Fig. 10 *The durability test to evaluate the performance of the NaSil system shut-off material.*

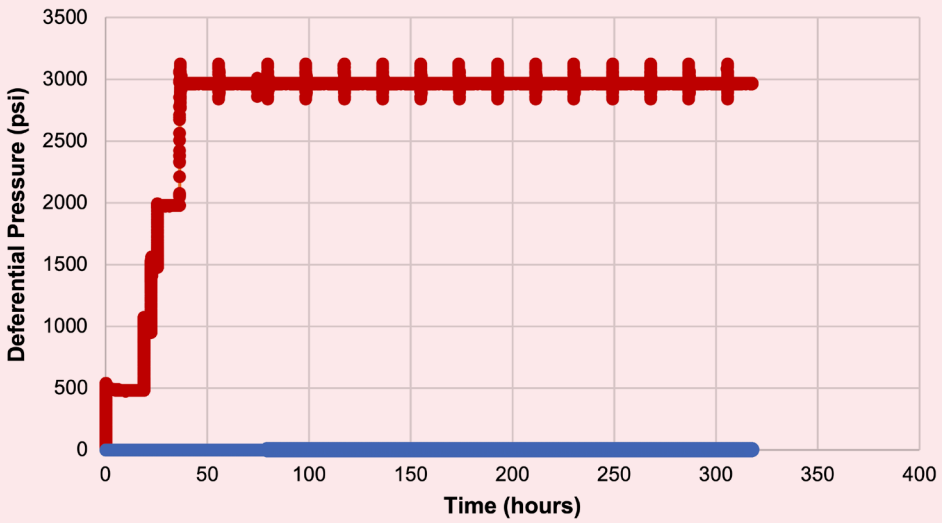

The equivalent drawdown pressure that the core was able to withstand is 10,285.7 psi (3,000 psi/ft × 3½" core plug length) with no evidence of flow through in the plug sample.

Yard Test Results

Figure 11 represents the layout of a batch mixing unit of 50 bottles. The batch mixing initially starts by filling the tank with the required volume of NaSil fluid followed by the activator. After that, we collected a NaSil sample from the batch mixer after 15 minutes of blending. Then, we measured the properties of the sample and benchmarked it with a baseline, which was prepared earlier in the lab. The measurements incorporates viscosity, density, and pH at ambient conditions.

As shown in Table 1, both samples have almost the same fluid properties. Additionally, we compared the gelation time of the baseline and yard sample by conducting a rheology experiment using a HPHT rheometer at bottom-hole temperature ~210 °F. As presented in Fig. 12, the gelation time of the yard sample (with 25% of activator) is nearly 60 minutes, which almost matches the gelation time of the baseline sample, which is approximately 70 minutes. This confirms how accurate the batch mixing was for the yard testing.

As for QA/QC in the field-testing, we divided this into two parts. The first one is associated with blending procedures, and the second one is linked to fluid as explained in the yard test.

The QA/QC of the blending was as follows:

- Ensure that all mixing equipment were clean and

Fig. 11 *A typical batch mixer for oil field applications.*

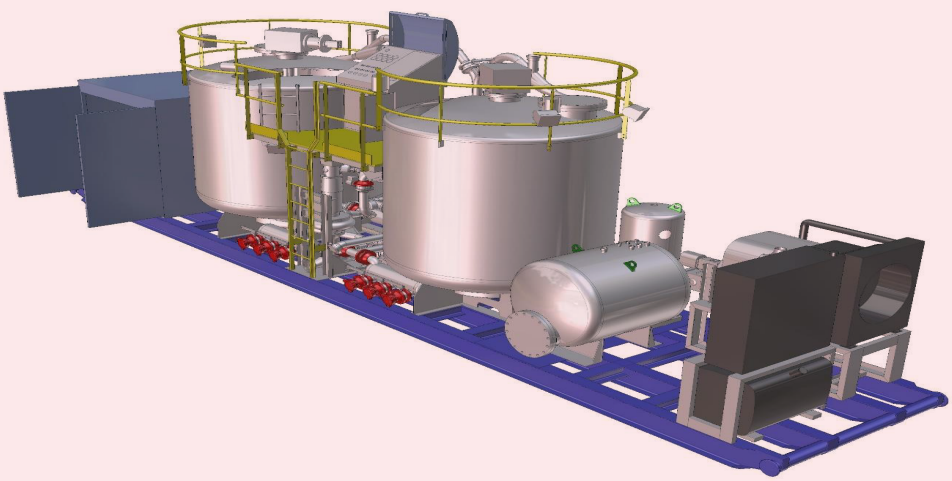

Table 1 Both samples used here have almost the same fluid properties.

NaSil Fluid Properties (25% Act.) at 70 °F	Baseline	Yard Test
pH	11.7 – 12.0	11.78
Density (g/cc)	1.29 – 1.30	1.302
Viscosity (cP)	5 – 6	6

Fig. 12 The gelation time validation between the baseline and yard samples.

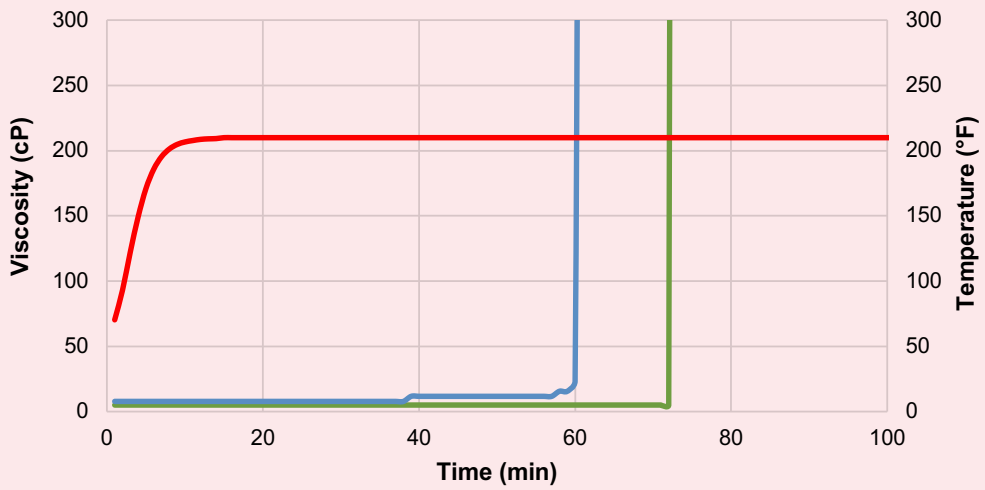

free of iron.

- Conduct water analysis on each frac tank before mixing.
- Use new hoses.
- Ensure that all drums and IBCs/totes are not leaking.
- Mix each batch volume separately in a batch tank.
- Collect samples periodically.

Breaker Test Results

As a contingency plan, we have looked into testing the ability to break the matured NaSil gel. Out of this experiment, we managed to select the optimum breakage time and breaker concentration at 210 °F to mimic downhole conditions. The experiment was conducted by preparing NaSil with 20 wt% of activator. Then, we collected 50 ml of NaSil and poured it into a glass bottle. After that, the glass bottle was placed in a water bath for the NaSil to gel at 210 °F.

Figure 13a shows the NaSil was gelled and fully matured. Next, we mixed an equivalent volume (50 ml) of breaker sample using field water and 30 wt% of active breaker. After that, the breaker solution was poured in the glass bottle on top of the gelled NaSil at 210 °F. The bottle was placed again in the water bath. Then, we started recording the time and observing the reaction every 30 minutes. We noticed that after two hours, the NaSil gel broke down completely, Fig. 13b.

Field Application and Results

It is essential to understand the fluid dynamics within the wellbore. A typical horizontal cased well completion may consist of a pre-perforated liner, ICDs, or inflow control valves. There are different designs

Fig. 13 A snapshot of two beakers: (a) represents the matured NaSil gel, and (b) represents the broken gel.

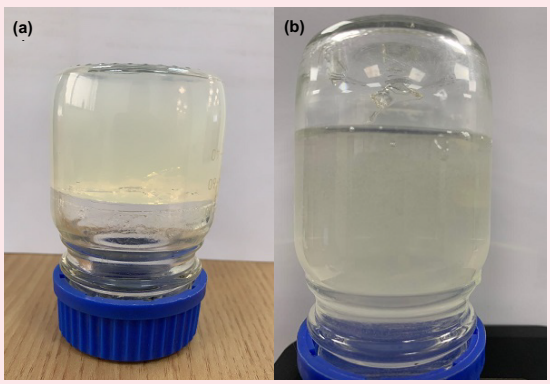

and acronyms for these broad completion types but in common, the wellbore is segmented in a way to produce a uniform flow from each segment and reduce production of unwanted phases. This can be achieved by the choice of the right design as well as a good annular isolation with either mechanical or swell packers.

Even with the right design, equipment may fail and a remedial job becomes essential. Chemical shut-off treatments are considered as a last resort if repair jobs fail or cannot be executed since in most cases it is a localized plug and abandoned in nature. A valid question at that point would be, is this the right thing to do and how would it affect the well performance? The answer to this question goes back again to the importance of understanding the fluid dynamics within the wellbore prior to making a serious decision to abandon one or multiple segments for the right motives.

The well selected for the first field application of NaSil is a horizontal cased hole with over 3,000 ft of reservoir contact. It is segmented into seven compartments of which a heavily fractured section is blank piped. The well is equipped with a total of 38 ICDs. The well was surveyed with a flow meter, noise, and temperature diagnostic logs. The middle compartment was found producing excessive water in addition to compromised mechanical packers leading to cross-flow behind the pipe, Fig. 14. Prior to deciding on any action plan, multiple steady-state flow simulations were conducted to match log results to identify factors that may affect the wellbore dynamics.

First, the water producing middle compartment dominated the other five producing segments. The compartment is 500 ft in length and is equipped with six ICDs. The mechanical packer below the treatment depth was sealing while the one above was leaking from the annulus to the shallower compartments based on the noise and temperature logs. Next, a set of steady-state simulations were conducted to assess the impact of reducing the number of active ICDs in the middle compartment as well as other compartments, Fig. 15.

Last, a review of rigless mechanical and chemical shut-off techniques were evaluated. Expandable patches and mechanical straddles were not fit since they may eliminate fluid ingress to the wellbore and wouldn't solve the crossflow behind the pipe. Resin and polymer-based gels are too thick and wouldn't provide enough penetration into the fracture system. Making them thinner wouldn't have solved the issue since it would take longer to gel and they may fail due to dissipation within the fracture system. In addition, abandoning the lower section of the well or post-job milling operation to regain access to the last two compartments was not acceptable. Only the NaSil provided reasonable pumping rate and time as well

Fig. 14 *A diagram showing the well diagnostics (open hole electrical image log, flow meter, spectral noise and temperature).*

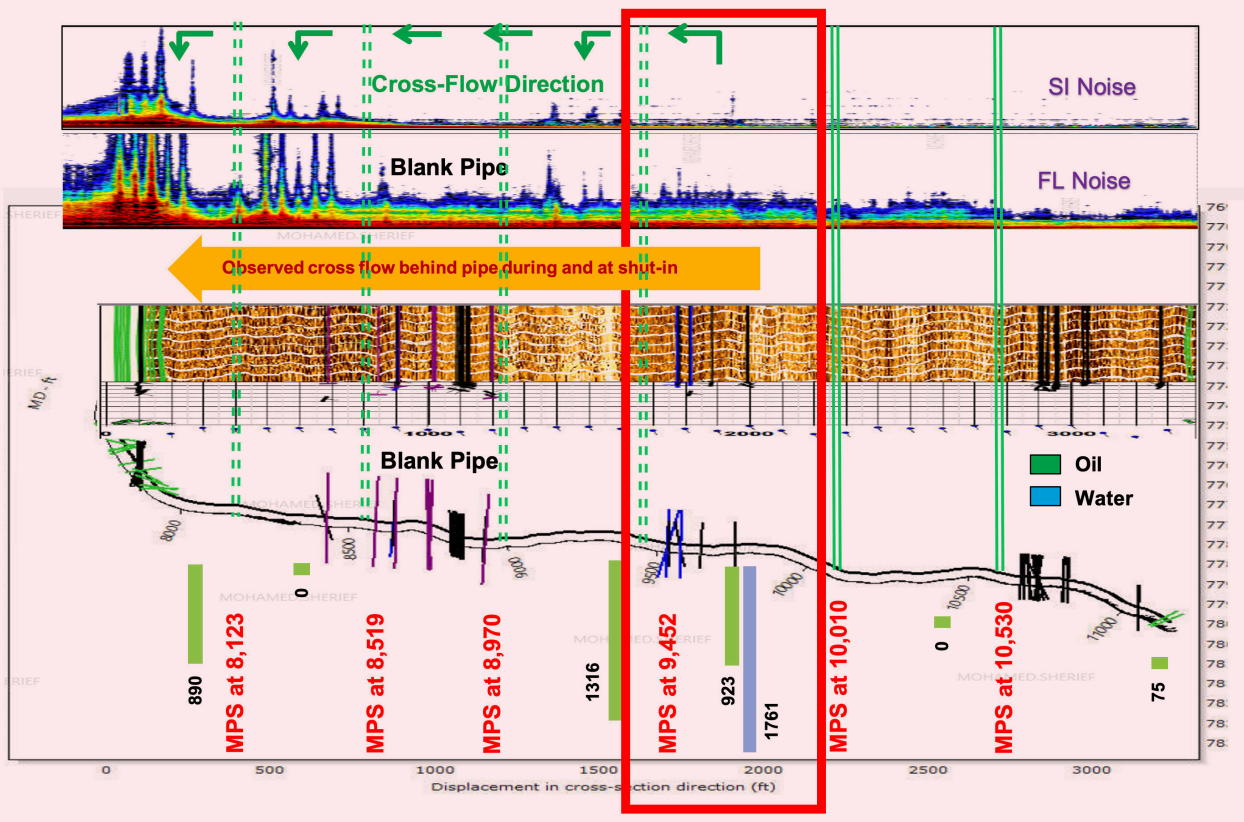

Fig. 15 *The matched ICD contribution based on flow meter data. Below, the estimated inflow after reducing the contribution from the middle compartment with the NaSil treatment.*

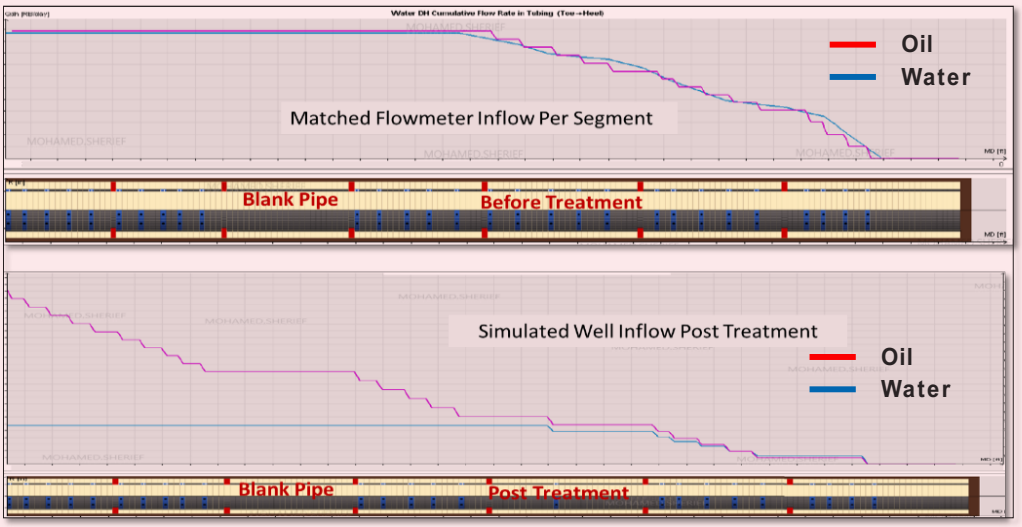

as fast gelling to ensure pumping enough volume to reduce the contribution from this compartment.

The squeeze job was conducted by setting a retrievable inflatable bridge plug in between the location of the last ICD in the highlighted compartment and the mechanical packer just below it, Fig. 16.

A retrievable production packer was set in between the first ICD and loose mechanical packer just above it. The NaSil was pumped through coil tubing (CT) and the retrievable production packer against the bridge plug to go through the six ICD ports into the annulus to the formation. Once the treatment equipment and CT were retrieved and rigged down, the well was put back on production and another survey of flow meter, noise and temperature was conducted.

The post-job evaluation, Fig. 17, showed an 80% reduction of the treated section productivity, an increase of contribution from the other five producing segments in addition to complete elimination of the behind pipe crossflow.

Summary and Conclusions

A novel NaSil was developed as a water shut-off technology and offers competitive advantages over the current technologies:

- By composition, the NaSil is eco-friendly and environmentally acceptable.
- As a water thin liquid phase, it can be injected easily and deeply in a single pumping stage.
- It has a substantial pressure increase after gelation with extreme effective plugging performance during extended coreflood experiment with great stability at high temperatures.
- Easy to mix components; NaSil and activator.

The first successful application was to: (1) Restore

Fig. 16 *Retrievable production packer and bridge plug used during the NaSil squeeze operation.*

Fig. 17 *The post-job well diagnostics (flow meter, spectral noise, and temperature).*

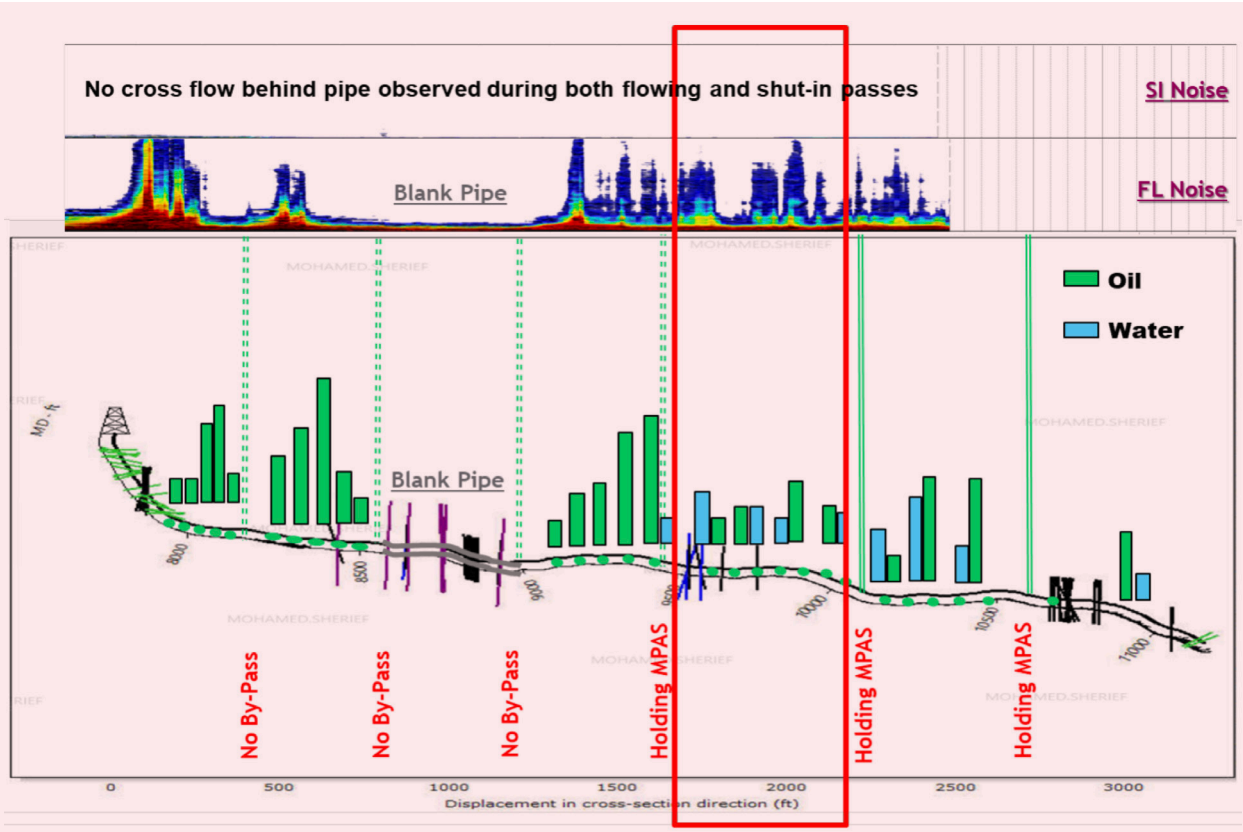

the annular isolation across a 500 ft cased hole compartment in the middle of a horizontal oil producer and eliminate annular cross flow, (2) Reduce the contribution from six ICDs within one compartment, and (3) Improve the overall well inflow performance and reduce water production.

References

1. Javid, K., Mustafa, H., Chitre, S., Anurag, A., et al.: "Comprehensive ICD/ICV Completion Design Workflow Practiced in Green Oil Field Offshore, Abu Dhabi," SPE paper 192645, presented at the Abu Dhabi International Petroleum Exhibition and Conference, Abu Dhabi, UAE, November 12-15, 2018.
2. Reiss, L.H.: "Production from Horizontal Wells After 5 Years," *Journal of Petroleum Technology*, Vol. 39, Issue 11, November 1987, pp. 1411-1416.
3. Joshi, S.D.: *Horizontal Well Technology,* PennWell Publishing Co.: Tulsa, Oklahoma, 1991, 535 p.
4. Permadi, P., Lee, R.L. and Kartoatmodjo, R.S.T.: "Behavior of Water Cresting under Horizontal Wells," SPE paper 30743, presented at the SPE Annual Technical Conference and Exhibition, Dallas, Texas, October 22-25, 1995.
5. Permadi, P., Wibowo, W., Alamsyah, Y. and Pratomo, S.W.: "Horizontal Well Completion with Stinger for Reducing Water Coning Problems," SPE paper 37464, presented at the SPE Production Operations Symposium, Oklahoma City, Oklahoma, March 9-11, 1997.
6. Cao, M., Wu, X., An, Y., Han, G., et al.: "A Novel Inflow Control Device Design Philosophy of Optimizing Horizontal Well Performance," SPE paper 180286, presented at the SPE Deepwater Drilling and Completions Conference, Galveston, Texas, September 14-15, 2016.
7. Joseph, A. and Ajienka, J.A.: "A Review of Water Shutoff Treatment Strategies in Oil Fields," SPE paper 136969, presented at the Nigeria Annual International Conference and Exhibition, Tinipar-Calabar, Nigeria, July 31-August 7, 2010.
8. Baylocq, P., Fery, J.J. and Grenon, A.: "Field Advanced Water Control Techniques Using Gel Systems," SPE paper 49468, presented at the Abu Dhabi International Petroleum Exhibition and Conference, Abu Dhabi, UAE, November 11-14, 1998.
9. Almohsin, A.M., Alabdulmohsen, Z., Bai, B. and Neogi, P.: "Experimental Study of Crude Oil Emulsion Stability by Surfactant and Nanoparticles," SPE paper 190440, presented at the SPE EOR Conference at Oil and Gas West Asia, Muscat, Oman, March 26-28, 2018.
10. Almohsin, A.M., Huang, J., Alabdrabalnabi, M. and Sherief, M.: "A Nano Method for a Big Challenge: Nanosilica-Based Sealing System for Water Shutoff," SPE paper 204840, prepared for presenting at the SPE Middle East Oil and Gas Show and Conference, event canceled, November 28-December 1, 2021.

11. Alabdrabalnabi, M., Almohsin, A.M., Huang, J. and Sherief, M.: "Experimental Investigation of a Novel Nanosilica for Blocking Unwanted Water Production," SPE paper 205820, presented at the SPE/IATMI Asia Pacific Oil and Gas Conference and Exhibition, virtual, October 12-14, 2021.

About the Authors

Dr. Ayman M. Al-Mohsin

Ph.D. in Petroleum Engineering, Missouri University of Science and Technology

Dr. Ayman M. Al-Mohsin joined Saudi Aramco in 2014 as a Research Engineer. He is currently a Petroleum Engineer working in Smart Fluid Focus Area in the Production Technology Division of Saudi Aramco's Exploration and Petroleum Engineering Center – Advanced Research Center (EXPEC ARC). Ayman's research interests include water and gas shutoff using chemical means.

He received his B.S. degree in Mechanical Engineering from the University of New Haven, West Haven, CT; his M.S. degree in Petroleum Engineering from New Mexico Tech, Socorro, NM; and his Ph.D. degree in Petroleum Engineering from Missouri University of Science and Technology, Rolla, MO.

Mohamed H. Sherief

B.S. in Chemical Engineering, Cairo University

Mohamed H. Sherief is a Petroleum Engineering Specialist working in the Shaybah Unit of Saudi Aramco's Southern Area Reservoir Management Department. He has more than 22 years of experience in oil and gas exploration, field development planning, and production operations.

Prior to Saudi Aramco, Mohamed worked for major IOC/NOC players, including an international reservoir engineering studies consulting firm.

He is a member of the Saudi Council of Engineers and a member of the Society of Petroleum Engineers (SPE), and a Certified Petroleum Engineer.

Mohamed received his B.S. degree in Chemical Engineering from Cairo University, Giza, Egypt.

Mohammed I. Alabdrabalnabi

B.S. in Chemical Engineering, King Fahd University of Petroleum and Minerals

Mohammed I. Alabdrabalnabi joined Saudi Aramco in August 2015 as a Petroleum Engineer with the Production Technology Division of Saudi Aramco's Exploration and Petroleum Engineering Center – Advanced Research Center (EXPEC ARC).

His research interests include fracturing fluids, water shutoff fluid systems, sand control, and condensate banking.

Mohammed received his B.S. degree in Chemical Engineering from King Fahd University of Petroleum and Minerals (KFUPM), Dhahran, Saudi Arabia.

Ahmad Muhammad

M.S. in Petroleum Engineering and Project Management, French Petroleum Institute

Ahmad Muhammad joined Saudi Aramco in 2019 and currently works as a Senior Production Engineer in the Shedgum Production Engineering Unit of Saudi Aramco's Southern Area Production Engineering Department. He has about 20 years of technical and operational experience across different countries (Angola, Nigeria, the Netherlands, and Oman) in the disciplines of production optimization, well integrity, well completions and intervention.

Ahmad received his B.S degree in Petroleum Engineering from the University of Ibadan, Ibadan, Nigeria, and his M.S degree in Petroleum Engineering and Project Management from the French Petroleum Institute, Paris, France.

Enhanced Injection Fluid Performance for EOR by Alternative Sulfate Removal Technique

Dr. Peter Birkle, Dr. Yunjiao Fu, Dr. Anaam H. Al-ShaikhAli, and Dr. Shouwen Shen

Abstract /

The injection of seawater into petroleum reservoirs is a well-established method utilized for enhanced oil recovery (EOR) to maintain reservoir pressure. The incompatibility between injection water and formation water (FW) requires cost intensive treatment methods to prevent scaling and clogging of pore space. The present study's main approach is to optimize the composition of injection water through the precipitation of barite ($BaSO_4$) and other sulfate minerals prior to subsurface injection. Sulfate (SO_4^{2-}) enriched, untreated seawater was mixed with barium (Ba^{2+}) enriched FW to trigger mineral precipitation, coupled with subsequent microfiltration of flocculated particles.

Geochemical analyses of major, minor, and trace elements on fluid phases and mineralogical analysis on solid precipitates were coupled with thermodynamic modeling and laboratory experiments to define optimum mixing ratios for commingled produced water reinjection during waterflooding. Geochemical reactive modeling with thermodynamic data for aqueous species and mineral phases revealed that variations in injection water chemistry could significantly alter saturation conditions for the mineral's scaling.

Therefore, optimum residual SO_4^{2-} concentrations below 100 mg/L in the commingled fluid is achieved by a fluid mixing ratio of 10:90 between seawater and FW. Depending on the modeled mixing ratio between seawater and FW, a total mass between 1.6 g and 5.5 g of sulfate and carbonate minerals will precipitate per liter of commingled fluids. Per liter of mixed water, a peak removal of 1.1 g of celestine ($SrSO_4$) and 0.5 g $BaSO_4$ is achieved for mixing ratios of 40:60 and 10:90, respectively, between seawater and FW.

Laboratory experiments with mixed solutions resulted in the immediate increase of fluid turbidity by coagulation flocculation of suspended particles in the two-component fluid, and its complete sedimentation within a few hours to a 24 hour period. X-ray diffraction (XRD) analyses revealed that precipitates mainly consist of sulfate minerals, including $BaSO_4$ (67 wt%), $SrSO_4$ (10 wt%), and gypsum ($CaSO_4 \cdot 2H_2O$) (14 wt%) with a minor presence of halite (9 wt%). Solid particles, as shown by environmental scanning electron microscopy (ESEM) and energy-dispersive X-ray microanalysis (EDS) analyses, are relatively homogeneous, agglomerated oval-shaped with an average size of 2.5 µm.

The proposed treatment technique represents a cost-effective alternative to the energy intensive nanofiltration technology for the removal of sulfates from seawater without adding chemicals. Nonreactive characteristics of the desulfated fluid mix product will contribute to minimize the scaling of operational wells and to enhance the performance of EOR projects. Additionally, the potential utilization of FW as an injection fluid component will reduce the amount of produced wastewater and economize the cost of treatment.

Introduction

The injection of seawater into the petroleum reservoir represents the principal method for enhanced oil recovery (EOR) to maintain reservoir pressure[1]. The contact and mixing of seawater with formation water (FW) during EOR is a commonly described process[2], but little is known about the mixing mechanisms in the affected reservoir[3]. Injection water can either displace or mix with connate water from the oil leg zone or with overlying aquifer water[2]. The chemical incompatibility between injection water and original FW is considered the principal cause of potential hydrogeochemical reactions and scale formation in the reservoir[4].

Chemical and physical processes during a fluid injection cannot be standardized or generalized due to the compositional heterogeneity of FW, aquifer water, and reservoir host rocks. Produced water composition is strongly dependent on whether the injection will occur into the oil leg or aquifer zone. In general, the salinity of pore water in sedimentary basins is highly heterogeneous and can range from 5,000 mg/L to 300,000 mg/L[5].

The concentration of sulfate (SO_4^{2-}) in FW is relatively low and rarely exceeds 1,000 mg/L due to reduced conditions in deep reservoirs. In contrast, SO_4^{2-} is abundant in seawater with average concentrations of 2,700 mg/L, and even higher SO_4^{2-} concentrations under restricted circulation conditions in isolated basins with enhanced evaporation processes, i.e., Arabian Gulf.

These heterogeneous factors require variable mixing ratios between FW and injection water for successful sulfate removal in each specific case.

Objectives

This article presents the outcome of a feasibility study of an alternative technology to optimize the composition of injection fluids for waterflooding and EOR. The basic target is to control production losses and reservoir souring by scaling through the mitigation of SO_4^{2-} ions prior to fluid injection. The presented method investigates the mixing of two incompatible fluids — sulfate-rich seawater with barium (Ba) rich FW — coupled with microfiltration technology, as an economically feasible technique to trigger the precipitation of barite ($BaSO_4$) and other sulfate minerals.

As a novelty in comparison to previous studies, the research task was approached by a combination of multidisciplinary methods to quantify optimum mixing ratios between injection water and FW:

- Geochemical analyses of major, minor, and trace elements of different fluid types (ion chromatography (IC), inductively coupled plasma mass spectrometry (ICP-MS), and inductively coupled plasma optical emission spectrometry (ICP-OES)).
- Mineralogical analysis (X-ray diffraction (XRD), wavelength dispersive X-ray fluorescence (WDXRF), and environmental scanning electron microscopy (ESEM) and energy dispersive X-ray microanalysis (EDS)) on residual precipitates.
- Numerical modeling to define optimum mixing ratios between both fluid types for the compositional optimization of injection fluid.
- Laboratory experiments to reconstruct fluid mixing and mineral precipitation.
- The numerical results are tested and verified by laboratory experiments and vice versa.

Scaling by Sulfate Minerals

The technical concept of sulfate removal through the mixing of two operational fluid types is founded on the premise of thermodynamic incompatibility between FW and seawater. The mixing of Ba^{2+} enriched FW with SO_4^{2-} enriched seawater causes the immediate precipitation of solid sulfate minerals as a consequence of its oversaturation stage, Eqn. 1:

$$\underset{\text{FW}}{Ca^{2+}\,(\text{or } Ba^{2+} \text{ or } Sr^{2+})} + \underset{\text{Seawater}}{SO_4^{2-}} \leftrightarrow \underset{\text{Precipitate}}{CaSO_4\,(\text{or } BaSO_4 \text{ or } SrSO_4)} \quad (1)$$

The velocity of $BaSO_4$ precipitation can be influenced by the following parameters[1, 6]:

- Supersaturation
- Overall salt concentration (total dissolved solids (TDS))
- Temperature and pressure
- pH
- Shear rate (as a measure for the flow conditions)
- Contact surface
- Crystallization nuclei
- Molar ratio $n(Ba^{2+})/n(SO_4^{2-})$

The common deposition of sulfate minerals causes severe problems regarding scaling and formation damage in upstream operations that are generally considered an irreversible process due to their extremely low solubility[7]. $BaSO_4$ is one of the most common scale minerals that can cause a considerable reduction in oil and gas production by coating perforations, casing, production tubulars, valves, pumps, and downhole completion equipment.

For the specific case of the Girassol field in Angola, Vu et al. (2000)[8] calculated the possible formation of 320 g $BaSO_4$ per m^3 of coproduced water during waterflood operation. Mineral precipitation was caused by the contact of injection seawater with FW, with elevated concentrations of 2,800 mg/l in SO_4^{2-} for the first, and 230 mg/l of Ba^{2+} and Sr^{2+} for the latter water type. Just 50 ppm of precipitation from 10,000 bpd of produced water equates to over 33 tons per year of scale products[9]. Sr-$BaSO_4$ minerals are frequently formed in oil fields when incompatible waters, such as injection water and FW, are mixed in the reservoir[4].

From the thermodynamic point of view, $BaSO_4$ precipitation is an unavoidable process when mixing sulfate-rich seawater with barium-bearing FW in the reservoir during seawater injection. SEM micrographs from coreflooding experiments with injection water and FW in porous sandstone revealed the dominant formation of $BaSO_4$[10].

Scale Modeling

Mathematical models for sulfate scaling are generally based on equations for reactive flow in porous media[11, 12] and the law of active masses[13, 14]. Thermodynamic scale prediction modeling suggests a most critical scaling potential for a mixing proportion with 20% to 60% of seawater[15]. Laboratory experiments by mixing injection water with FW caused a permeability decline from 5% to 19% by the formation of $BaSO_4$ in porous sandstone cores, depending on brine composition, initial permeability, temperature, differential pressure, and brine injection period[10].

The scale prediction with thermodynamic models revealed a dependence between different sulfate minerals in the simultaneous competitive co-precipitation of $BaSO_4$, $CaSO_4$ and celestine ($SrSO_4$) from brines[16]. The oil/water displacement and impact of injection water/FW mixing mechanisms on $BaSO_4$ scaling were simulated with numerical tools by Sorbie and

Mackay (2000)[2]. The simulation was focused on the vertical and spatial water cut development with heterogeneities in fluid displacement by banking effects in heterogeneous reservoirs.

Variations in the chemistry of produced water were not considered for this large-scale waterflood displacement of injection water/connate water/aquifer water. Well injectivity can be affected by precipitation within a radius 10 to 20 times larger than the well radius[17].

The same authors derived a mathematical model for the co-injection of low sulfate seawater with barium containing produced water, including specifications of produced water — seawater ratios and maximum allowed SO_4^{2-} concentration in seawater after treatment, plus a prediction for injectivity decline.

Scaling Avoidance

To avoid scaling and to control production losses and reservoir souring in upstream operations, the formation of sulfate minerals, especially $BaSO_4$, has to be mitigated. As a standard procedure prior to injection, a costly treatment of primary seawater is performed to remove SO_4^{2-} from the injection fluid, which will avoid the potential precipitation of sulfate minerals during the injection process. Membrane treatment technologies, mainly nanofiltration, are currently applied as a standard and cost intensive method to reduce the elevated SO_4^{2-} concentration of primary seawater[9, 18].

The nanofiltration technology can reduce the SO_4^{2-} concentration from 2,700 mg/L in seawater to less than 100 mg/L, but with elevated costs for nanofiltration membranes, operation, and maintenance. Polyamide thin-film composite membranes reduced the seawater SO_4^{2-} concentration on the Brae "A" Platform (Gulf of Mexico) from an average of 2,650 mg/L to less than 50 mg/L[9]. Bader (2007)[19] proposes a combination of pressure-driven membranes, i.e., nanofiltration and reverse osmosis, with liquid-phase precipitation or compressed-phase precipitation to solve inherent sulfate scale problems in treating seawater for the selective removal of SO_4^{2-}.

As an alternative, scale inhibitor squeeze treatment is performed concurrently during the injection stage by pushing the scale inhibitor solution into a producing formation and fixing the inhibitor in the formation[20]. The kinetic modeling of the scale inhibition mechanism leads to predictive capabilities and framework for interpretation of experimental work[21]. Several studies were performed to calibrate and validate chemical flooding simulators through history matching oil displacement coreflooding results[22-24].

Methods

The sequence of applied methods is divided into pre-experimental, experimental, and post-experimental stages, Fig. 1.

Stage 1: Pre-Experiment

- **Sampling and geochemical analysis of fluid endmembers**

  Two fluid samples with elevated Ba^{2+} concentrations of 305 mg/L and 806 mg/L, and low SO_4^{2-} concentrations below 100 mg/L, were selected to be representative endmembers for FW from a clastic reservoir formation. Due to the limited volume of the FW samples, a synthetic FW (FW-syn) solution was prepared to mimic the chemical composition of FW for use throughout the lab experiments. To form the synthetic FW sample, 59,485.56 mg of sodium chloride (NaCl), 35,191.88 mg of calcium chloride ($CaCl_2*2H_2O$), 2,848.62 mg of strontium chloride ($SrCl_2*6H_2O$), and 710.21 mg of barium chloride ($BaCl_2$) were added to 600 g of distilled water.

  Samples SW-1 and SW-2 of seawater were taken from the Arabian Gulf in Abu Dhabi[25] and Saudi Arabia (present study), respectively. The hydrochemical analysis of major ions (sodium [Na^+], calcium [Ca^{2+}], potassium [K^+], magnesium [Mg^{2+}],

Fig. 1 The workflow for designing an optimum mixing ratio between injection fluid and FW.

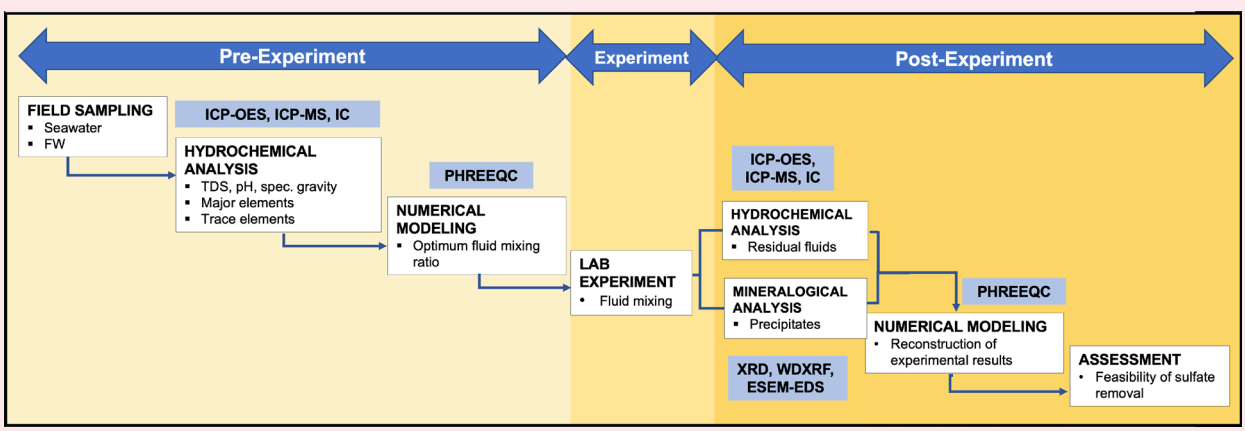

chloride [Cl^-], bicarbonate [HCO_3^-], and SO_4^{2-}) and selected minor and trace elements (aluminum [Al^{3+}], boron [B^{3+}], barium [Ba^{2+}], lithium [Li^+], iron [Fe^{2+}], strontium [Sr^{2+}], and total dissolved silica [Si^{4+}]) of seawater, FW, FW-syn, and experimental fluid residuals was performed by IC, ICP-MS, and ICP-OES at the Chemistry Analysis Unit (Research & Development Center) of Saudi Aramco.

- **Numerical modeling of optimum fluid mixing ratio**

  Geochemical computing codes have the capability to: (1) perform speciation and saturation index calculations of aqueous species, (2) to calculate batch reaction and 1D transport, such as the mixing of solutions, and (3) to perform inverse modeling of mineral and gas mole transfers to trace differences in water composition[26]. A detailed description of available numerical tools for geochemical modeling is given by Birkle (2012)[27].

  Standard geochemical and speciation methods can be used to simulate the mass conversion of water-rock-gas interactions for various mixing ratios between seawater and FW in the presence of reactive reservoir minerals and gas components. The developed model is based on the law of conservation of mass and charge as well as on the thermodynamics of chemical equilibrium. The thermodynamic database, *phreeqc.dat*, was utilized as an input data set for the present case study.

  The Pitzer aqueous model (*pitzer.dat* database) was applied for high salinity waters that are beyond the range of application for the Debye-Hückel theory[28]. First, the modeling was performed between both water endmembers (untreated injection water and FW) to achieve minimum SO_4^{2-} concentrations in the residual fluid. Then, both endmembers were mixed at various volume ratios to determine optimum commingled fluid ratios for the lab experiments.

Stage 2: Lab Experiment

- **Mixing injection water with FW-syn**

  A volume of 400 g of injection water was added to 600 g of FW-syn into a separating funnel to induce the precipitation of solids from the mixed solutions. Although the flocculation of suspended solids in the solution occurred within a few minutes after fluid mixing, the gravitational settling of all residuals to the bottom of the funnel or beaker required a repose time of the experiment for several days.

  The mineralogical analysis (XRD, WDXRF, ESEM-EDS) of precipitates requires a minimum solid mass of 5 g, therefore, the discussed experiment was repeated three times with a total fluid volume of four liters to recover the requested mass of precipitated solids. After five days of gravitational settling, the settled sludge was separated from the residual fluid and dried in the incubator at 45 °C for three days for subsequent mineralogical analysis.

Stage 3: Post-Experiment

- **Analysis of residual fluids and precipitates**

  Post-experimental fluids were analyzed on their hydrochemical composition, as described in Stage 1. ESEM-EDS, XRD, and WDXRF spectrometry techniques were utilized by the Advanced Analytical Unit (R&DC, Saudi Aramco) to determine the elemental, mineralogical, and chemical composition of newly formed precipitates after mixing injection water with FW-syn.

  An ESEM integral with EDS system was utilized to determine the microstructure and composition of the provided residuals. The solids were mounted on SEM aluminum stub holders using double-sided conductive carbon tape and then were inserted into the ESEM sample chamber with operating conditions of 20 kV, easy pressure mode and 10 mm working distance. Compositional backscattered electron images and EDS microanalyses in spot area analysis mode were acquired from different areas of the materials.

  For XRD and WDXRF, the precipitate sample was homogenized and manually grounded by an agate mortar and a pestle for several minutes to achieve fine particle size. For XRD analysis, the fine powder was mounted into the XRD sample holder by back pressing. For WDXRF analysis, 4 g of powder was mixed well and homogenized with 0.9 g of binder (Licowax C micro powder PM (Hoechstwax)). The powder was pressed with 20 tons into a pellet with a 31 mm diameter. The SALAM 014 and Omnion 27 were used for the XRD and WDXRF analysis, respectively.

  The XRD pattern of the sample was compared with every calculated pattern in the Powder Diffraction File (PDF) database from the International Center for Diffraction Data (ICDD). All crystalline phases were identified by using search-match capabilities of the XRD software JADE 9.1+ and the ICDD-PDF database. The quantification of the data was performed using the whole pattern fitting method.

- **Numerical modeling of precipitation processes**

  Results from the lab experiments were tested and verified by numerical calculations with thermodynamic data for aqueous species and mineral phases, and vice versa. This strives to quantitatively demonstrate whether geochemical modeling can reproduce the main chemical and physical processes observed during lab experiments.

  Based on the experimental and modeled results, the treatment process can be designed by defining an optimum mixing ratio to achieve minimum concentrations of SO_4^{2-} residuals in the injection fluid.

Results

Hydrochemical Fluid Composition

Pre-experiment: The analyzed chemical composition of two types of seawater from the Arabian Gulf (SW-1 and SW-2), two samples of representative FW (FW-1

and FW-2), and FW-syn with an average composition between FW-1 and FW-2 are given in Table 1.

Seawater is characterized by a Na-Mg-Cl-SO_4 water type under neutral to alkaline pH conditions, but its salinity can locally differ from 44,000 mg/L (sample SW-1) to 59,900 mg/L (sample SW-2). As common for natural FW regimens, samples present a spatial compositional variation with a TDS between 111,100 mg/L (sample FW-1) and 154,000 mg/L (sample FW-2) of hypersaline, Na-Ca-Cl type. Notably, the utilized seawater samples are relatively enriched in SO_4^{2-} (3,420 mg/L to 4,920 mg/L) and Mg^{2+} (1,560 mg/L to 2,350 mg/L) under slightly alkaline conditions (pH = 7.8 to 8.2), while FW is relatively abundant in Ca^{2+} (11,560 mg/L to 16,120 mg/L), Ba^{2+} (305 mg/L to 806 mg/L) and Sr^{2+} (1,070 mg/L to 1,530 mg/L) ions.

The FW-syn sample was reconstructed with an intermediate composition between FW-1 and FW-2, as shown by TDS concentrations of 135,000 mg/L.

Numerical Modeling

Numerical modeling was performed to determine mixing ratios between both water endmembers (untreated seawater and FW) to achieve optimum SO_4^{2-} concentrations in the residual fluid (used for EOR). Both endmembers were mixed at various volume ratios. The modeling results show that the SO_4^{2-} concentration of the mixed fluids decreases with decreasing seawater proportions. The lowest SO_4^{2-} concentrations in the residual fluid (to be used for EOR injection) are achieved by a seawater proportion of less than 10%, Fig. 2. The original SO_4^{2-} concentration of 4,920 mg/L for seawater (Table 1: SW-2) could be reduced to values below 100 mg/L with the proposed mixing ratios of approximately 10 vol% seawater and 90 vol% FW.

In the case of sample SW-1, the highest amount of total precipitates — 1.4 g per liter of mixed water — can be achieved by mixing 40% of untreated seawater with 60% of FW, Fig. 3.

$SrSO_4$ and $BaSO_4$ are the most affecting scale minerals for more than 90% of the precipitates. $SrSO_4$ has its maximum precipitation potential with a seawater/FW mixing ratio of 40:60, while $BaSO_4$ is most abundant with a seawater/FW ratio of 10:90. This result is consistent with scale prediction[16] performed for brines with diverse ion concentrations. From there, $BaSO_4$ precipitation tends to be most severe at low mixing ratios between injected seawater and FW, while $SrSO_4$ has the highest scaling potential for two fluid types with similar mixing contributions. Oversaturated conditions for gypsum ($CaSO_4 \cdot 2H_2O$) and iron hydroxide ($Fe(OH)_3$) are exclusively given at seawater/FW mixing ratios of 70:30 to 80:20 (for $CaSO_4 \cdot 2H_2O$), and 30:70 to 0:100 (for $Fe(OH)_3$).

In contrast, local variations in the seawater composition, e.g., by limited water circulation and enhanced evaporation by enclosed conditions of the Arabian Gulf, will affect the saturation state of seawater during mixing with FW. The performed simulation with a more salinized sample (SW-2 with TDS of 59,900 mg/L) resulted in a general increase of the total precipitation amount to a maximum of 5,800 mg/L at a fluid ratio of 70:30, Fig. 4.

For the purpose of SO_4^{2-} removal, the maximum peaks for $BaSO_4$ and $SrSO_4$ precipitates of 500 mg/L and 1,500 mg/l (per 1 L of mixed water), respectively, are very similar in intensity to the previous simulation with lower saline seawater.

Table 1 *The geochemical composition of primary fluid types before the lab mixing experiment, including seawater, FW, and FW-syn.*

Parameter	Seawater	Seawater	Formation Water	Formation Water	Formation Water
Sample ID (mg/L)	SW-1	SW-2	FW-1	FW-2	FW-syn
pH*	7.8	8.2	3.3	2.5	6.6
TDS	44,000	59,900	111,100	154,000	135,000
Ca^{2+}	600	695	11,560	16,120	15,240
Mg^{2+}	1,560	2,350	954	1,260	< 1.0
Na^{+}	13,900	19,895	30,520	39,230	38,080
K^{+}	n.a.	671	1,140	1,750	< 10
Cl^{-}	24,300	32,020	67,940	97,310	81,540
SO_4^{2-}	3,420	4,920	< 100	< 100	< 100
Ba^{2+}	n.a.	1	305	806	592
Sr^{2+}	n.a.	13	1,070	1,530	1,290

*pH = negative logarithm of hydrogen ion concentration; n.a. = not analyzed

Fig. 2 *Theoretical sulfate concentration in the residual fluid depending on the mixing ratio between seawater and FW, shown here as the proportion of seawater in the mixed fluid. The chemical composition of both initial components (SW-2 and FW) is shown in Table 1.*

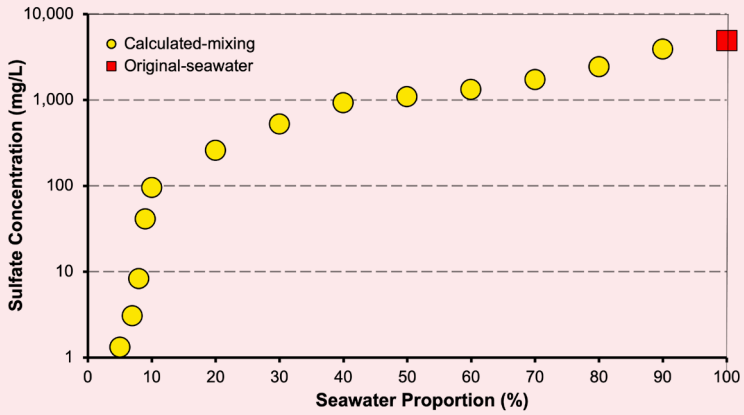

Fig. 3 *The numerical simulation of mixing FW with raw seawater and the resulting amount of total precipitates and individual minerals. Variations in the mixing ratio between FW-1 and SW-1 (TDS = 44,000 mg/L) are causing abrupt changes of oversaturated conditions.*

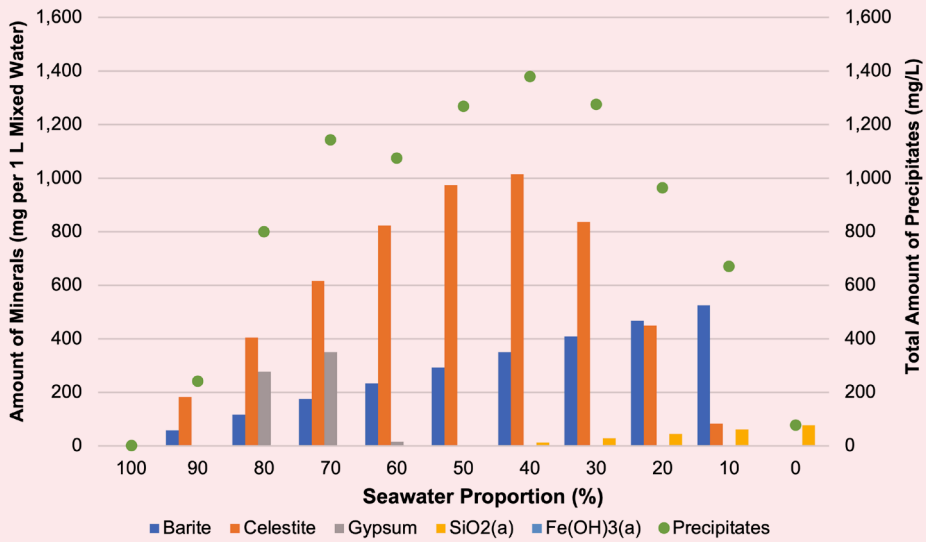

Laboratory Experiment

An optimum mixing ratio of 40 vol% and 60 vol% for natural seawater (sample SW-2) and FW-syn, respectively, was selected for the experiment based on numerical calculations. This strives to collect sufficient precipitates for their mineralogical analysis with XRD, WDXRF, and ESEM-EDS. Then, 400 g of untreated seawater was added to 600 g of FW-syn into a separating funnel.

The mixed solution turned immediately from an initial transparent consistency of FW, Fig. 5a, toward immediate turbidity by the flocculation of suspended particles, caused by the addition of 400 g of untreated seawater, Fig. 5b, which indicates the containment of suspended solid matter in the mixed fluid phase. White particles were also observed on the inner wall of the separatory funnel. Gravitational settling caused the accumulation and sedimentation of most precipitates at the bottom of the funnel within a time period of several hours, Fig. 5c, to 4 days, Fig. 5d.

Subsequently, the accumulated sludge-like precipitate, Fig. 6a, was dried for 24 hours in a lab oven at 60 °C, Fig. 6b. Oven-dried aggregates for 24 hours are flake-shaped with a diameter range between 0.1 mm to 1.0 mm, Fig. 6c. In contrast, the slow drying of the milky sludge for several days caused the crystallization of snowflake or star-shaped crystals with a diameter range from 1.5 mm to 6.0 mm, Fig. 6d.

Fig. 4 *The numerical simulation of mixing FW with seawater with a more elevated salinity (SW-2: TDS = 59,900 mg/L) in comparison to SW-1 seawater (TDS = 44,000 mg/L) from Fig. 3. Variations in the water composition cause abrupt changes of the saturation index for carbonate and sulfate minerals for alternate fluid mixing proportions.*

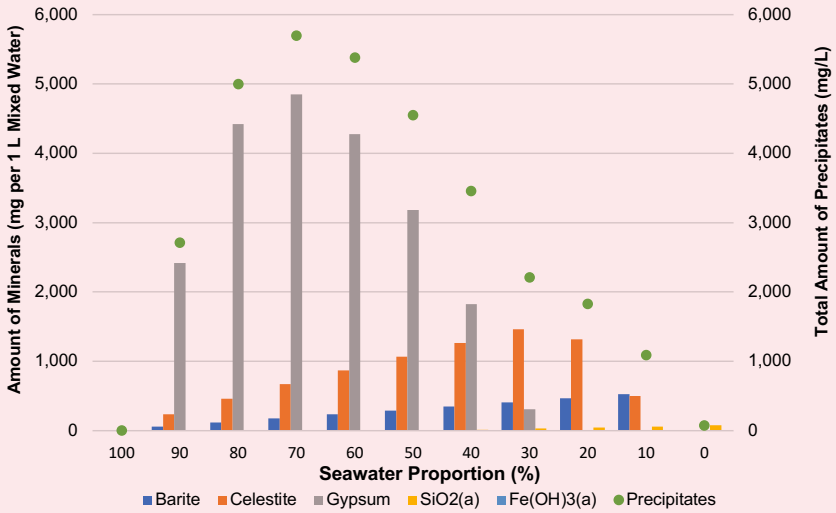

Fig. 5 *The transparency of FW-syn at the beginning of the experiment (a), with an immediate turbidity change by flocculation of suspended particles after adding seawater (b), and gravitational settling of most precipitates at the bottom of the funnel after several hours (c), and after sitting for four days (d).*

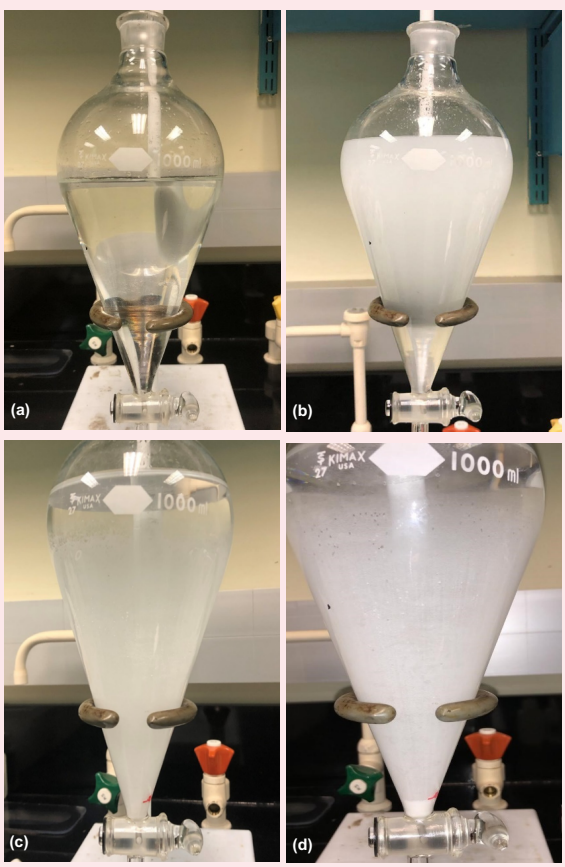

Fig. 6 *The precipitated solids from the fluid mixing experiment with different consistencies and scale: (a) original precipitate as residual sludge in a petri dish, (b) oven dried flakes with size of image "c," (c) flakes with a diameter range from 0.1 mm to 1.0 mm, and (d) snowflake or star-shaped crystals with a diameter range from 1.5 mm to 6.0 mm.*

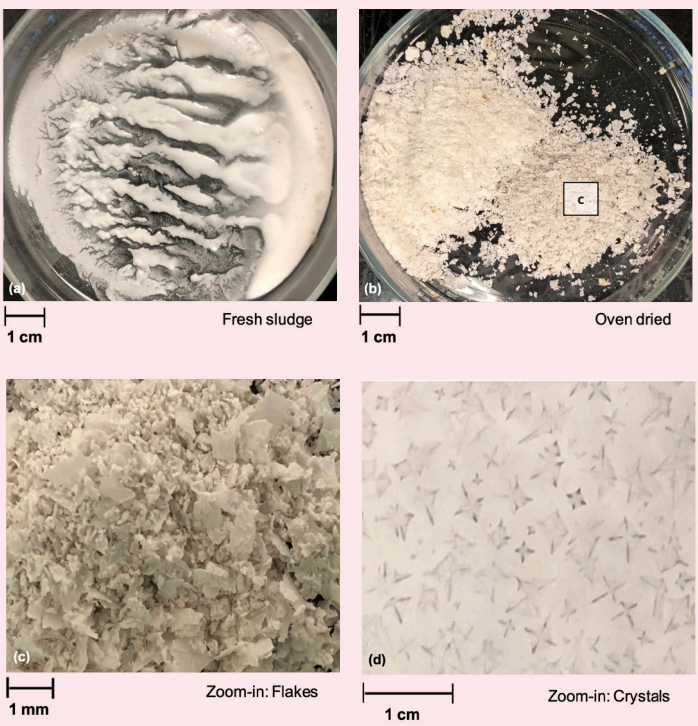

Post-Experimental Assessment

Fluid Geochemistry

For post-experimental fluids, the inert mixing between untreated SW-2 and FW-syn at a volumetric ratio of 40:60 should result in similar proportions for the abundance of aqueous species. Table 2 illustrates the post-experimental fluid's theoretically expected and measured chemical composition, respectively. Elements with decreasing or increasing concentrations during the experiment are marked in red or blue color, respectively.

As expected, specific elements, such as Na and Cl, show a nonreactive behavior during mixing, as reflected by a minor deviation of 0.6% and 3.6%, between the measured and calculated concentration. In contrast, secondary processes such as the precipitation of oversaturated species cause the depletion of several reactive elements in the residual fluid. The concentrations of Ba^{2+}, SO_4^{2-}, Mg^{2+}, and Sr^{2+} ions are 99.7%, 44.0%, 13.7%, and 12.4% lower, respectively, as expected by a purely inert process of fluid mixing.

The significant depletion of Ba^{2+} and SO_4^{2-} ions in the residual solution, respectively, implies their removal from the liquid phase through the precipitation of $BaSO_4$. A decrease of 12.4% for Sr^{2+} suggests a minor precipitation process for $SrSO_4$ and/or strontianite ($SrCO_3$). The flocculation of other salts, i.e., NaCl, MgCl, and KCl, and carbonates ($CaCO_3$) seems to be of minor magnitude.

Mineralogy of Precipitates

ESEM backscattered electron imaging reveals that both solid precipitate samples have an identical morphology consisting of agglomerated oval-like particles, Fig. 7. ESEM analysis shows that the precipitates have an

Fig. 7 *The ESEM images of precipitates at low and high magnifications reveal that both have an identical morphology consisting of agglomerated oval-like particles.*

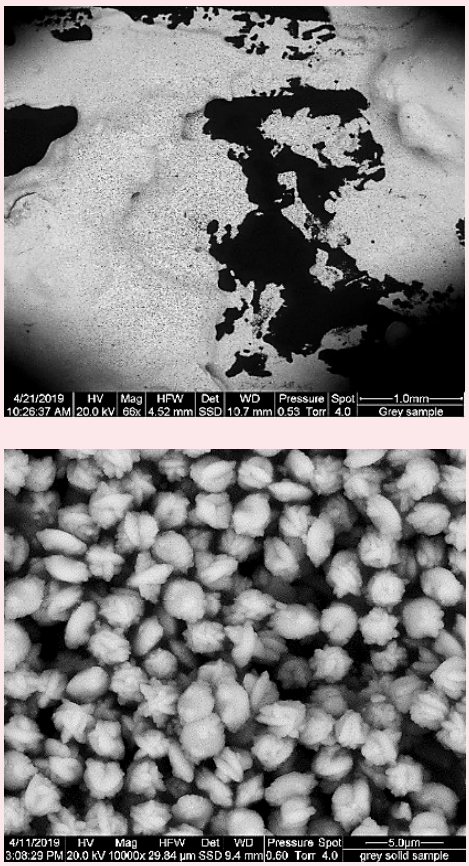

Table 2 *The comparison and difference (in %) between the theoretically expected fluid composition (after mixing SW-2 with FW-syn at a 40:60 ratio) and the actually measured post-experimental composition.*

Parameter	Post-Experiment Solution	Post-Experiment Solution	ΔPost - Theo
Sample ID (mg/L)	Theoretical	Measured	(%)
pH*	6.8	7.5	0.8
TDS	104,900	106,100	1.1
Ca^{2+}	9,420	9,600	1.9
Mg^{2+}	940	811	-13.7
Na^{+}	30,810	30,630	-0.6
K^{+}	274	250	-8.9
Cl^{-}	61,730	63,930	3.6
SO_4^{2-}	2,030	1,140	-44.0
Ba^{2+}	356	< 1.0	-99.7
Sr^{2+}	777	681	-12.4

*pH = negative logarithm of hydrogen ion concentration

Fig. 8 *The correlation of semi-quantitative analysis of precipitates measured by ESEM (wt% in upper table) with EDS of the precipitates, which was obtained after mixing seawater with FW. Spot area analysis mode SP2 (above) and SP3 (below).*

Element (wt%)									
C	O	Na	Mg	Sr	S	Cl	K	Ca	Ba
1.85	29.75	1.23	0.16	12.44	13.83	3.18	0.36	2.95	34.23
1.93	26.62	1.24	0.23	13.42	13.99	4.13	0.53	3.25	34.66
1.82	31.17	1.06	0.21	12.19	13.68	3.31	0.34	2.89	33.32
1.88	24.45	0.98	0.26	13.03	14.15	3.40	0.50	3.56	37.77
1.13	23.95	0.87	0.16	13.27	14.72	2.90	0.55	3.30	39.15
7.94	28.68	0.85	0.00	15.06	13.28	2.17	0.39	2.64	28.98
8.37	29.04	0.95	0.13	13.19	12.84	2.0	0.40	2.61	30.47
9.21	15.80	0.72	0.3	13.96	12.9	3.84	0.37	3.98	38.92
7.17	21.75	1.03	0.26	11.72	12.5	3.35	0.55	3.79	37.88
5.63	23.94	1.26	0.14	13.39	13.47	3.74	0.35	3.34	34.74

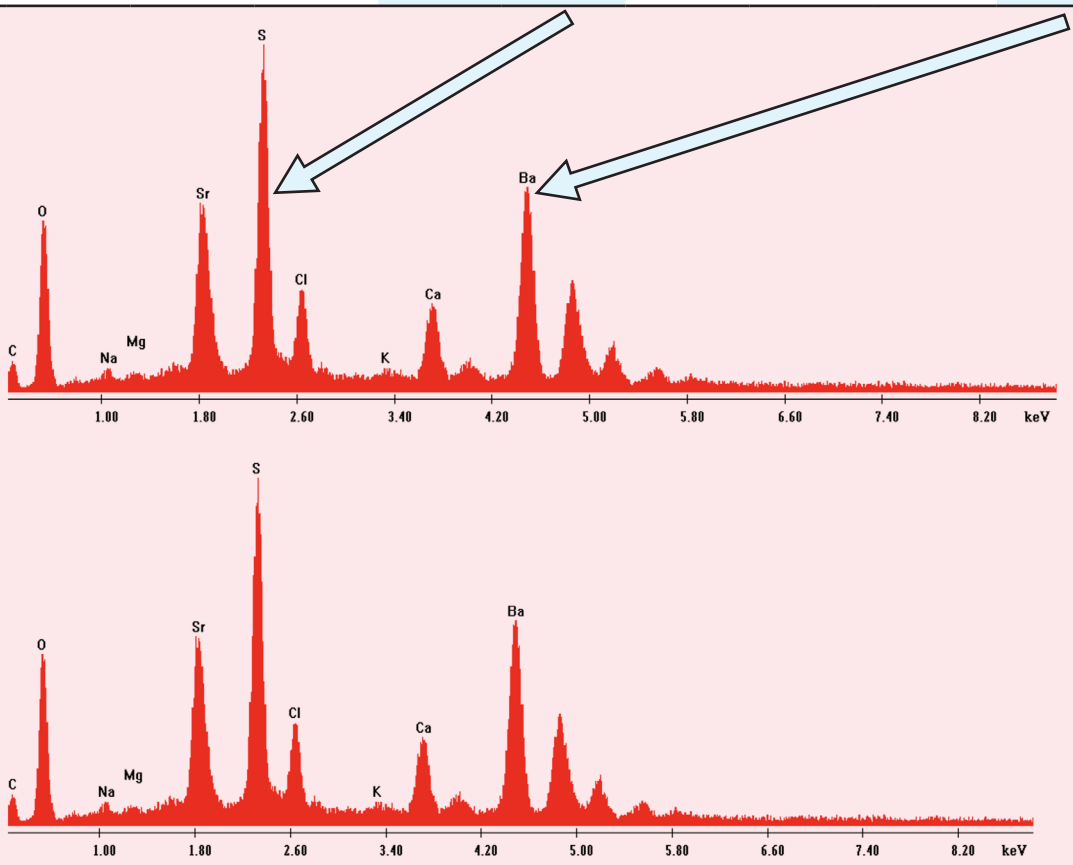

almost uniform grain size with an average diameter of 2.5 µm. The corresponding EDS measurements showed that these particles are mainly composed of O, S, Ba, Sr, and Ca with varying concentration levels of C, Cl, Na, and K.

Figure 8 illustrates two representative spot analyses of a total series of 10 EDS analyses. Due to an inconsistency in the obtained EDS data, multiple EDS measurements of five different spot analyses were acquired from each sample, and the data were averaged to minimize the statistical error. It must be clarified that the estimated error in the performed EDS analyses is ± 5% to 10% and higher for trace elements (less than 1 wt%). In addition, there are possible sources of errors

Table 3 *The semi-quantitative composition of precipitate solids collected after mixing injection water with the FW-syn measured by XRD.*

Compound	Weight Percentage (wt%)
$BaSO_4$	67
$SrSO_4$	10
$CaSO_4 \cdot 2H_2O$	14
NaCl	9

Table 4 *The chemical composition of the solid precipitates measured by WDXRF.*

Element	Wt%
O	31.2
Ba	29.4
S	14.0
Sr	12.1
Cl	5.4
Na	3.5
Ca	3.3
P	0.4
H	0.3
K	0.2
Si	0.1
Cs	0.1
Al	0.1
Mg	0.1

in the data due to peaks overlapping, absorption, and X-ray fluorescence.

The mineralogical and chemical composition of the solid precipitates were analyzed by XRD, Table 3, and WDXRF, Table 4, respectively. Relative approximate values were normalized to 100%. XRD analyses illustrate that precipitates mainly consist of sulfate minerals, including $BaSO_4$ ($Ba_{0.75}Sr_{0.25}SO_4$) with appreciable amounts of $CaSO_4 \cdot 2H_2O$, $SrSO_4$, and NaCl. A diffractogram with reference patterns of identified compounds is illustrated in Fig. 9. The WDXRF results confirmed the XRD findings with O (31.2%), Ba (29.4%), S (14.0%), and Sr (12.1%) as major elemental components.

$BaSO_4$ in the sample is not in an ideal formula, as Sr replaced some Ba in the structure. The precipitation of sulfate minerals caused the reduction of the initial

Fig. 9 *The XRD results of precipitate solids collected after mixing the injection fluid with the FW-syn.*

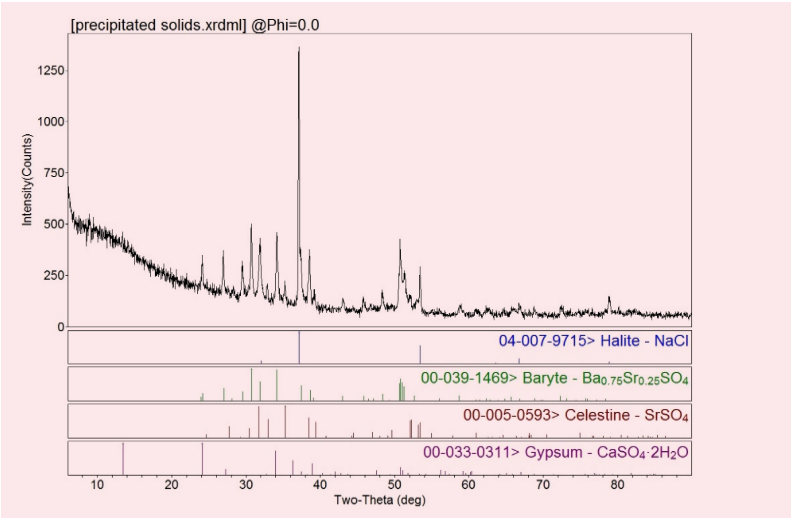

SO_4^{2-} concentration from 4,920 mg/L in primary seawater to 1,140 mg/L in the post-experimental, residual solution. The additional rinse of the precipitates could even lower the observed trace amounts for halite of 9 wt%, as detected by XRD. The precipitation of minerals took place immediately after mixing both endmember fluids, indicating that the kinetic inhibition on the precipitation of sulfate-bearing minerals is of minor impact.

Numerical Testing of Experimental Results

The results from the lab experiments were tested and verified by numerical calculations with thermodynamic data for aqueous species and mineral phases, and vice versa. This strives to quantitatively demonstrate whether geochemical modeling can reproduce the main chemical and physical processes observed during lab experiments.

Figure 10 shows the comparison of measured (from lab experiments) vs. simulated concentrations (from numerical modeling) of major elements (Cl^-, Na^+, Ca^{2+}, Mg^{2+}, and SO_4^{2-}) and minor elements (Sr^{2+}, K^+, and Ba^{2+}) of the residual fluid after the experiment. The measured and modeled results are within an acceptable range of less than 10%.

Figure 11 shows a good agreement between the measured and calculated abundance of SO_4^{2-} and Ca^{2+} in the residual precipitate. In contrast, the mass balance shows a molar Ba^{2+}/Sr^{2+} ratio of 0.60 in the precipitates, whereas the measured ratio is 1.55. This inconsistency could result from: (1) no-rinse of precipitates by using distilled water, and (2) a high TDS of FW that affects the calculation of water-rock interaction with the database *phreeqc.dat*. The Pitzer set of thermodynamic data[28] is commonly used for high saline water, but does not contain any barium-bearing minerals.

Potential variations of the geochemical composition

Fig. 10 *The comparison of experimental (yellow bars) vs. modeled concentrations (blue line) of major elements in the post-experimental, residual water solution. Primary injection fluid, 40 vol%, was mixed with 60 vol% of FW-syn to remove most sulfates from the injection phase.*

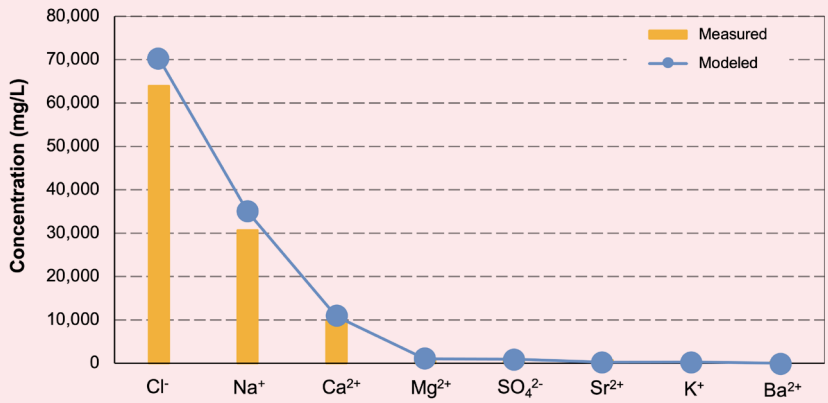

Fig. 11 *The comparison of experimental (yellow bars) vs. modeled concentrations (blue line) of Ba^{2+}, Sr^{2+}, S (in SO_4^{2-}) and Ca^{2+} in precipitates. Primary injection fluid, 40 vol%, was mixed with 60 vol% of FW-syn to precipitate most sulfates from the injection phase.*

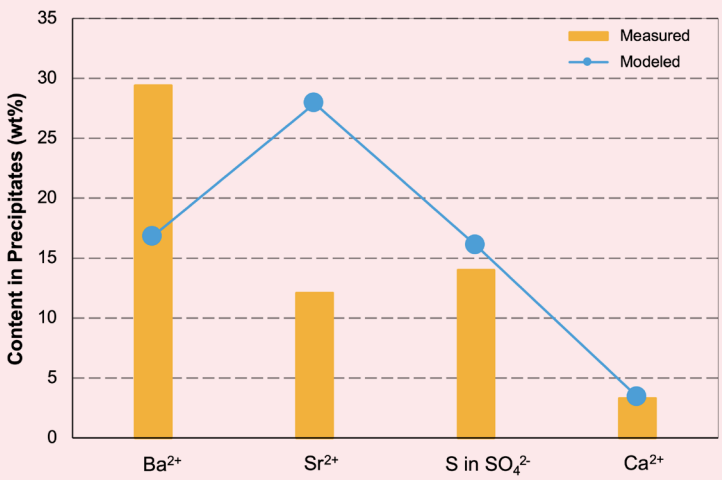

of FW during the lifetime of producing wells can be overcome by repeating numerical simulations with modified input parameters for the FW phase. Consequently, the mixing ratio between untreated injection water and FW has likely to be adjusted according to the simulation results. As the experimental outcome was calibrated by the initial numerical modeling, required changes in the mixing ratios — caused by the fluctuating geochemical composition of FW — can be addressed by repeated simulations. A second round of lab experiments is only required in case of substantial changes in the reservoir conditions and fluid parameters.

In terms of water chemistry and mineralogical composition of the precipitates, a good agreement between simulated and experimental results demonstrates the accuracy of performed lab experiments. In this case, geochemical software can quantitatively reproduce the main processes during the mixing of primary injection water with FW, and can be applied for any other scenario.

If the simulated and experimental results indicate a high potential for the precipitation of sulfate-bearing minerals, untreated seawater for EOR needs to be desulfated prior to injection. If the calculated results indicate no potential for the precipitation of sulfate-bearing minerals at all mixing ratios, desulfating is not required, therefore, no need for the pre-treatment of seawater to-be-injected.

Technology Practical Benefit

This article presents an effective method to remove

SO_4^{2-} via $BaSO_4$ precipitation through the mixing of two incompatible water types. The conducted lab experiment showed that the newly formed precipitate grains have an average diameter of 2.5 µm. Instead of nanofiltration, microfiltration could be applied as an effective method to separate fine $BaSO_4$ particles from the aqueous solution. Compared to nanofiltration, microfiltration has a higher recovery ratio of typically 90% to 98% (ratio of product per feed) than nanofiltration (75% to 95%), a higher permeate flux (liter/m^2/h), a lower energy cost, and less operating pressure (0.3 to 2.1 bar vs. of 5.2 to 8.6 bar) with a lower total cost per m^3 of aqueous fluids to be filtered, including capital and operational costs, in comparable systems[18].

As an economic advantage of the presented technology in comparison to commercially available treatment technologies, no additional chemicals are required to remove SO_4^{2-} ions from raw seawater. Only naturally occurring aqueous solutions — FW and seawater — are used for the proposed process. FW as a mixing additive represents a commonly abundant byproduct at oil, gas, and water separation facilities.

In addition to SO_4^{2-} ions, the presented method can lower the concentration of Ba^{2+}, Sr^{2+}, and Ca^{2+} ions in the mixed fluid compared to the original FW composition in the reservoir. Therefore, this process will reduce the potential of scale formation when injecting a combination of seawater with FW compared to the utilization of raw seawater. In the subsurface, FW is generally in equilibrium with the reservoir mineral assemblage. Removing these ions causes undersaturated conditions for specific minerals, i.e., $CaCO_3$ or $SrCO_3$, in the mixed fluid, which prevail during fluid injection under specific reservoir temperature and pressure conditions. Therefore, the injection of mixed fluids can cause the dissolution of calcite ($CaCO_{3(s)}$) and strontianite ($SrCO_{3(s)}$) minerals to a certain extent with a potential improvement of reservoir rock properties.

Besides drilling fluids and fracking fluids, produced FW from upstream operations contributes to wastewater that requires treatment. As a general trend, the volume of produced water constantly increases with the increasing maturity stage of the operating field. As an example, water production within several units from the Shell group has increased steadily from about 350,000 m^3/d in 1990 to over 1,000,000 m^3/d in 2003[29].

After treatment, reinjection of produced water into the reservoir is a common method to dispose of wastewater. For the Shell group, Khatib and Verbeek (2003)[29] reported treatment and disposal costs between \$0.15/m^3 to as much as \$15/m^3 for the produced water volume. The application of the present technology of mixing raw seawater with FW can significantly decrease the volume of wastewater to be disposed of, and therefore, reduce the cost of wastewater treatment. The final permeate can be used as low SO_4^{2-} water for reinjection as an essential part of the EOR or waterflooding process.

Conclusions

The application of EOR technology to maintain pressure conditions in oil fields requires cost-effective treatment methods to increase the quality of injected fluids. This article presents a technical feasibility study to desulfate injection fluids through the precipitation of sulfate minerals by mixing untreated seawater with FW in combination with microfiltration. The described process can guarantee the absence of precipitation of sulfate scale minerals during the commingled injection of mixed fluids into the target formation.

The combination of laboratory experiments with geochemical and mineralogical analysis of pre- and post-experimental samples and kinetic modeling proves that $BaSO_4$, $SrSO_4$, and $CaSO_4$ represent the principal precipitates induced by mixing sulfate-rich seawater with Ba^- and Sr^- bearing FW. A volumetric mixing ratio of 40:60 and 10:90 between seawater and FW was modeled to result in a maximum removal rate of $SrSO_4$ (1.1 g per liter of commingled fluids) and $BaSO_4$ (0.5 g per liter of commingled fluids) in the residual fluid.

The observed agreement between the experimental and modeled approach confirms the reproducibility of small-scale lab experiments for local field applications. Due to local variations in seawater and produced water composition, lab experiments and geochemical modeling have to be conducted with fluid characteristics and reservoir conditions for each specific case. As an additional step to introduce the designed fluid into field operation, the performance and pressure behavior throughout the injection process should be assessed through coreflooding experiments and by the preliminary testing of pilot wells.

The desulfated fluid mix will improve the quality of injection water and can be used to enhance the performance of waterflooding or EOR process with the following advantages:

- Well lifetime: Expansion of the lifetime for exploration and production wells by minimized scaling.
- Seawater treatment: Reduced amount of required raw seawater treatment though proposed commingled technique.
- Disposal of produced water: Minimized wastewater volume through the utilization of produced water for EOR purposes.
- Facility logistics: Ergonomic utilization of both fluid types — FW as a common byproduct of hydrocarbon production and seawater as principal injection fluid — as generally abundant fluids on EOR and waterflood sites.
- Energy savings: Fluid commingling and microfiltration are less costly as conventional, energy intensive methods of nanofiltration and chemical treatment for raw seawater.

Acknowledgments

The authors would like to acknowledge the performance of geochemical analysis of water samples by the Chemical Analysis Unit (R&DC: Saeed H. Shahrani, Ali M. Tawfiq and Nada S. Alghamdi), and thank Ibrahim Z. Atwah (EXPEC ARC) for review of the manuscript.

References

1. Bin Merdah, A.B. and Mohd Yassin, A.A.: "Barium Sulfate Scale Formation in Oil Reservoir during Water Injection at High Barium Formation Water," *Journal of Applied Science*, Vol. 7, Issue 17, December 2007, pp. 2393-2403.

2. Sorbie, K.S. and Mackay, E.J.: "Mixing of Injected, Connate and Aquifer Brines in Waterflooding and its Relevance to Oil Field Scaling," *Journal of Petroleum Science and Engineering*, Vol. 27, Issues 1-2, July 2000, pp. 85-106.

3. Baraka-Lokmane, S. and Hurtevent, C.: "Chemical Incompatibilities between Formation Water and Injection Water; Comparison between Modeling and Site Observations in Fields Operated by TOTAL," SPE paper 161314, presented at the Abu Dhabi International Petroleum Conference and Exhibition, Abu Dhabi, UAE, November 11-14, 2012.

4. van Berk, W., Fu, Y. and Schulz, H-M.: "Temporal and Spatial Development of Scaling in Reservoir Aquifers Triggered by Seawater Injection: Three-Dimensional Reactive Mass Transport Modeling of Water-Rock-Gas Interactions," *Journal of Petroleum Science and Engineering*, Vol. 135, November 2015, pp. 206-217.

5. Kharaka, Y.K. and Hanor, J.S.: "Deep Fluids in Sedimentary Basins," Chapter in *Surface and Groundwater, Weathering, and Soils, Treatise on Geochemistry Vol. 7*, 2nd edition, (eds.) Holland, H.D. and Turekian, K.K., Elsevier, 2014, pp. 471-515.

6. Canic, T., Baur, S., Bergfeldt, T. and Kuhn, D.: "Influences on the Barite Precipitation from Geothermal Brines," paper presented at the World Geothermal Congress, Melbourne, Australia, April 19-25, 2015.

7. Scogings, A.: "Drilling Grade Barite: The Global Outlook," *https://www.csaglobal.com/wp-content/uploads/2015/03/Drilling-grade-barite-the-global-outlook-IM-Mag-January-2015.pdf*, 2014.

8. Vu, V.K., Hurtevent, C. and Davis, R.A.: "Eliminating the Need for Scale Inhibition Treatments for Elf Exploration Angola's Girassol Field," SPE paper 60220, presented at the 2nd International Symposium on Oil Field Scale, Aberdeen, Scotland, U.K., January 26-27, 2000.

9. Heatherly, M.W., Howell, M.E. and McElhiney, J.E.: "Sulfate Removal Technology for Seawater Waterflood Injection," OTC paper 7593, presented at the Offshore Technology Conference, Houston, Texas, May 2-5, 1994.

10. BinMerdhah, A.B., Mohd Yassin, A.A. and Muherei, M.A.: "Laboratory and Prediction of Barium Sulfate Scaling at High Barium Formation Water," *Journal of Petroleum Science and Engineering*, Vol. 70, Issues 1-2, January 2010, pp. 79-88.

11. Philips, O.M.: *Flow and Reactions in Permeable Rocks*, Cambridge University Press, 1991, 296 p.

12. Bedrikovetsky, P.G.: *Mathematical Theory of Oil and Gas Recovery*, Vol. 4 of the *Petroleum Engineering and Development Studies* series, (ed.) Rowan, G., London/Boston: Kluwer Academic Publishers, 1994, 596 p.

13. Bethke, C.M.: *Geochemical Reaction Modeling*, Oxford University Press, 1996, 416 p.

14. Woods, A.W. and Parker, G.: "Barium Sulphate Precipitation in Porous Rock through Dispersive Mixing," SPE paper 80401, presented at the International Symposium on Oil Field Scale, Aberdeen, Scotland, U.K., January 29-30, 2003.

15. Daher, J.S., Gomes, J.A.T., Rosario, F.F., Bezerra, M.C., et al.: "Evaluation of Inorganic Scale Deposition in an Unconsolidated Reservoir by Numerical Simulation," SPE paper 95107, presented at the SPE International Symposium on Oil Field Scale, Aberdeen, Scotland, U.K., May 11-12, 2005.

16. Yuan, M., Todd, A.C. and Sorbie, K.S.: "Sulphate Scale Precipitation Arising from Seawater Injection: A Prediction Study," *Marine and Petroleum Geology*, Vol. 11, Issue 1, February 1994, pp. 24-30.

17. Bedrikovetsky, P.G., Mackay, E.J., Silva, R.M.P., Patricio, F.M.R., et al.: "Produced Water Re-Injection with Seawater Treated by Sulphate Reduction Plant: Injectivity Decline, Analytical Model," *Journal of Petroleum Science and Engineering*, Vol. 68, Issues 1-2, September 2009, pp. 19-28.

18. Zularisam, A.W., Ismail, A.F. and Sakinah, M.: "Application and Challenges of Membrane in Surface Water Treatment," *Journal of Applied Sciences*, Vol. 10, 2010, pp. 380-390.

19. Bader, M.S.H.: "Sulfate Removal Technologies for Oil Fields Seawater Injection Operations," *Journal of Petroleum Science and Engineering*, Vol. 55, Issues 1-2, January 2007, pp. 93-110.

20. Kan, A.T., Dai, Z. and Tomson, M.B.: "The State-of-the-Art in Scale Inhibitor Squeeze Treatment," *Petroleum Science*, Vol. 17, 2020, pp. 1579-1601.

21. Al-Roomi, Y.M. and Hussain, K.F.: "Potential Kinetic Model for Scaling and Scale Inhibition Mechanism," *Desalination*, Vol. 393, September 2016, pp. 186-195.

22. Farajzadeh, R., Matsuura, T., van Batenburg, D.W. and Dijk, H.: "Detailed Modeling of the Alkali/Surfactant/Polymer (ASP) Process by Coupling a Multipurpose Reservoir Simulator to the Chemistry Package PHREEQC," *SPE Reservoir Evaluation and Engineering*, Vol. 15, Issue 4, April 2011, pp. 423-435.

23. Delshad, M., Han, C., Veedu, F.K. and Pope, G.A.: "A Simplified Model for Simulations of Alkaline-Surfactant-Polymer Floods," *Journal of Petroleum Science and Engineering*, Vol. 108, August 2013, pp. 1-9.

24. AlSofi, A.M., Liu, J.S. and Han, M.: "Numerical Simulation of Surfactant — Polymer Coreflooding Experiments for Carbonates," *Journal of Petroleum Science and Engineering*, Vol. 111, November 2013, pp. 184-196.

25. Brown, R.: *The Content and Nature of Arabian Gulf Seawater*, Emirates Natural History Group, Bulletin 29, July 1986.

26. Parkhurst, D.L. and Appelo, C.A.J.: "Description of Input and Examples for PHREEQC Version 3 — A Computer Program for Speciation, Batch Reaction, One-Dimensional Transport, and Inverse Geochemical Calculations," *U.S. Geological Survey Techniques and Methods*, Book 6, Chapter A43, 2013.

27. Birkle, P.: "Advances in Geochemical Modeling for Geothermal Applications," Chapter 7 in (eds.) Bundschuh, J. and Zilberbrand, M., *Geochemical Modeling of Groundwater, Vadose and Geothermal Systems*, CRC Press: London, 2012, pp. 153-178.

28. Plummer, N., Parkhurst, D.L., Fleming, G.W. and Dunkle, S.A.: "A Computer Program Incorporating Pitzer's Equations for Calculation of Geochemical

Reactions in Brines," *Water Resources Investigations Report* 88-4153, U.S. Geological Survey, 1988.

29. Khatib, Z. and Verbeek, P.H.J.: "Water to Value — Produced Water Management for Sustainable Field Development of Mature and Green Fields," SPE paper 73853, presented at the SPE International Conference on Health, Safety and Environment in Oil and Gas Exploration and Production, Kuala Lumpur, Malaysia, March 20-22, 2002.

About the Authors

Dr. Peter Birkle

Ph.D. in Geochemistry and Hydrogeology,
Freiberg University of Mining and Technology

Dr. Peter Birkle is a Senior Geological Consultant with the Geology Technology Division of Saudi Aramco's Exploration and Petroleum Engineering Center – Advanced Research Center (EXPEC ARC). As a SME in inorganic geochemistry and leader of the Hydrotracks team, his major target is the development of an artificial intelligence-based Oil Field Water Expert System (OWES), to predict the type, provenance and hydraulic dynamics of formation water as a predictive tool to trace hydrocarbon migration and trapping. The main goal is to enhance exploration performance and operational productivity by preventing/reducing excess water, improving well control and resistivity prediction, and tracking fluid migration and reservoir compartmentalization.

Prior to joining Saudi Aramco in 2011, Peter worked as a scientist for the Secretary of Energy and PEMEX (Mexico) in the development of geothermal and oil fields, respectively, in several countries of Latin America.

He is active member of the Society of Petroleum Engineering (SPE), American Association of Petroleum Geologists (AAPG), and the Mexican Academy of Sciences (AMC). In 2004, Peter received the National Science Award in Engineering and Technology from AMC, the Saudi Aramco Excellence Award in 2017, and the Effective Publication Award from EXPEC ARC in 2021.

He has published more than 80 papers in peer-reviewed journals and conferences, three books and 12 book chapters (h-index = 20; i10-index = 30). Peter also has three patents to his credit. He has been the associate editor for *Applied Geochemistry* and *Revista Mexicana de Ciencias Geológicas*.

In 1993, Peter received his M.S. degree in Geology from the University of Tübingen, Tübingen, Germany. In 1998, he received his Ph.D. degree in Geochemistry and Hydrogeology from the Freiberg University of Mining and Technology, Saxony, Germany.

Dr. Yunjiao Fu

Ph.D. in Geochemistry,
Clausthal University of Technology

Dr. Yunjiao Fu worked as an Inorganic Geochemist with the Geology Technology Division of Saudi Aramco's Exploration and Petroleum Engineering Center – Advanced Research Center (EXPEC ARC). Her expertise was focused on reactive mass transport modeling of complex petroleum-rock-water-gas interactions to mitigate scaling, formation damage, and the formation of hydrogen sulfide. She left the company in December 2019.

Before joining Saudi Aramco in 2016, Yunjiao worked as postdoctoral researcher at the German Research Center for Geoscience (GFZ) in Potsdam.

She has published 17 papers in peer-reviewed journals, nine abstracts in conferences, and one patent (h-index = 12; i10-index = 15).

In 2007, Yunjiao received her B.S. degree and in 2010, her M.S. degree, both in Geoenvironmental Engineering from Clausthal University of Technology, Clausthal-Zellerfeld, Germany, and then in 2014, she received her Ph.D. degree in Geochemistry, from the same institution.

Dr. Anaam H. Al-ShaikhAli

Ph.D. in Chemical Science (Catalysis),
King Abdullah University of Science and Technology

Dr. Anaam H. Al-ShaikhAli joined Saudi Aramco in 2006, and is currently a Senior Lab Scientist in the Technical Services Division of Saudi Aramco's Research & Development Center (R&DC).

Throughout her career, Anaam has contributed with advanced analytical support to the R&DC and the Exploration and Petroleum Engineering Center – Advanced Research Center's (EXPEC ARC) research projects, and to root cause analysis investigations for downstream and upstream operations.

Currently, she is focusing in supporting catalysts development and evaluation, material failure studies, as well as corrosion investigations and mitigation technologies.

Anaam's work has been presented in 14 contributions to conferences and in five peer-reviewed journals. Her involvement in the development of novel technologies has resulted in the contribution to two patents.

Anaam is a member of the Society of Petroleum Engineers (SPE), the Microscopy Society of America (MSA), and the American Chemical Society (ACS).

She received her M.S. degree in Chemistry from the University of Manchester, Manchester, U.K., and her Ph.D. degree in Chemical Science (Catalysis) from King Abdullah University of Science and Technology, Thuwal, Saudi Arabia.

Dr. Shouwen Shen

Ph.D. in Petroleum Geology,
Chengdu University of Technology

Dr. Shouwen Shen was a Science Specialist in the Advanced Analysis Unit of Saudi Aramco's Research & Development Center (now retired). Before joining Saudi Aramco in 2006, he worked at Southwest Petroleum University in China as an Associate Professor, at the University of Miami as a Visiting Scientist and at Core Laboratories Canada Ltd. as an X-ray Specialist.

Shouwen studied the seismic facies, sedimentary facies and sequence stratigraphy of Jurassic formations in the Turpan-Hami basin of China. He used piezoelectric transducers to measure the sonic velocity of various dolomites from the Madison formation of Wyoming and Montana, and he developed an empirical formula to predict the sonic velocity of dolomite according to thin section description. Shouwen also developed new XRD methods in-house for quantitative mineral analysis of sandstone and successfully solved the problem caused by the Rietveld method limitation.

His specialties include sequence stratigraphy, clastics diagenesis, clay mineralogy and formation damage assessment, thin section description, X-ray fluorescence elemental analysis, X-ray powder diffraction phase identification and quantification, crystallite size determination, texture and residual stress analyses.

Shouwen received a B.S. degree from the China University of Geosciences, Beijing, China, in 1982 and a Ph.D. degree in Petroleum Geology from Chengdu University of Technology, Sichuan, China, in 1998.

Toward Sustainable Freshwater Conservation: Seawater-Based High Temperature Fracturing Fluids

Dr. Rajendra A. Kalgaonkar, Manar M. AlAhmari, Dr. Mohammed A. Bataweel and Mustafa A. Al-Khowaildi

Abstract /

Hydraulic fracturing uses water. A sustainable approach is to utilize seawater — abundantly available — for hydraulic fracturing applications.

Although seawater-based fracturing fluids are available in the industry, there is a limitation on their usage with seawater rich in sulfate. Under downhole conditions, when the pumped seawater mixes with formation water containing high salinity and hardness, scale can form and potentially cause formation damage. Scale inhibitors become ineffective at such high temperatures and salinities. Due to its high scaling tendency, seawater should be pretreated — to remove specific ions that contribute most significantly to scaling.

Typically, at high temperatures, the fracturing fluids used are based on metal crosslinkers that have a high shear degradation tendency. As the fracturing fluid is pumped downhole, the fluid experiences different shears, such as high shears due to tubulars, and low shear in the fracture. If the crosslinker shear degrades, the fracturing fluid will lose its ability to transport proppant effectively inside the fracture, which will result in near wellbore screen out. Therefore, it is of paramount importance to develop fracturing fluids that can be utilized with seawater, as well as demonstrate effective proppant carrying capability.

This article highlights the development of a new zirconium (Zr) crosslinked, polysaccharide-based fracturing fluid system that was formulated using nanofiltered seawater for temperatures of 300 °F and above. The fluid is formulated using a stabilizer package that imparts temperature as well as shear stability to the fracturing fluid by controlling the Zr crosslinker reaction kinetics. The rheological characterization comprising of shear resilience and shear recovery capabilities of the new fracturing fluid are demonstrated through various shear history profiling experiments.

The fluid maintained a viscosity of more than 300 cP at constant temperatures of 300 °F and above for 2 hours under various shear profiles, including multiple shear as well as constant shear. A proppant suspension test showed excellent proppant suspension capability of the fluid at elevated temperatures. Additionally, regain permeability results obtained using delayed breaker chemistries showcased excellent cleanup potential of the new fracturing fluid. Scaling tests performed with the nanofiltered seawater-based fluid demonstrated complete mitigation of scaling tendency at 300 °F, with an extremely low-scale inhibitor dosage.

The nanofiltered seawater-based fracturing fluid comprised of the stabilizer package imparts several key advantages, including providing a seawater-based fluid with a near zero scaling tendency, as well as with high shear and temperature stability.

Introduction

Demand for water used in hydraulic fracturing is continuously increasing[1-3]. The potential burden on the freshwater resources has motivated the industry to prepare hydraulic fracturing fluids with less ideal water sources, such as seawater[4]. Seawater typically contains high levels of total dissolved solids (TDS), and the main components of the dissolved solids include sodium, calcium, and magnesium salts. The combination of high salinity and hardness can be very damaging to many types of fracturing fluids, especially at high temperatures, that are commonly formulated with freshwater.

At high temperatures, e.g., 300 °F or more, it is challenging to develop stable fluids using seawater due to the damage caused by the high levels of salinity and hardness in the water[5, 6]. Fracturing fluid systems have therefore been highly desirable and required that can be formulated with high TDS seawater, and perform satisfactorily at high temperatures of 300 °F. To address this issue, a new fracturing fluid was developed using nanofiltered seawater. The business impact from this development will open up a new avenue for fracturing fluids that effectively utilize the seawater to reduce dependence associated with using freshwater in hydraulic

fracturing operations.

An intensive testing program was designed to evaluate the use of nanofiltered seawater-based fracturing fluid in hydraulic fracturing. The fluid comprised of metal crosslinked polysaccharide and a stabilizer package that provided shear stability and thermal stability at high temperatures of 300 °F. In a typical rheology test, the fluid viscosity stayed above 300 cP for at least 100 minutes at 300 °F. An encapsulated breaker was used to break the fracturing fluid effectively. Coreflood experiments showed that the retained permeability was > 85% following the injection of the broken nanofiltered seawater-based fracturing fluid filtrate. Compatibility tests of the nanofiltered seawater with formation water showed no scale formation at 300 °F.

Moreover, it is well-known that at high temperatures of 300 °F or more, polysaccharides undergo thermal degradation[7, 8]. Typically, utilization of oxygen scavengers can prevent thermal degradation in polysaccharides[9]. Additionally, as the fracturing fluid is pumped downhole in high temperature wells, the fluid is exposed to these elevated temperatures as well as multiple shear regimes.

Both temperature and high shear can act as degradation mechanisms for metal crosslinked fracturing fluid[10, 11]. Premature degradation of the fracturing fluid could lead it to losing its capacity to suspend and transport proppant. These degradation mechanisms contribute to the reduction in viscosity, causing near wellbore proppant screen out and treatment failures. Therefore, it is vital to incorporate additives in the fracturing fluid formulation to mitigate these degradation mechanisms[12, 13].

This article focuses on developing a high temperature hydraulic fracturing fluid system formulated with nanofiltered seawater for applications up to 300 °F, with stable rheology, controlled break, excellent regained permeability, and no scaling tendency. The formulation utilizes a stabilizer package that provides a dual advantage by imparting high temperature stability as well as shear stability. The excellent stability of the fluid is sufficient for reliable proppant transportation and suspension.

The promising results of this study demonstrate that freshwater usage in hydraulic fracturing can be alleviated by using nanofiltered seawater.

Table 1 *The recipe of the nanofiltered seawater-based high temperature fracturing fluid.*

Chemicals	Concentration
Water	
Gelling agent	CMHPG 45 – 50 pptg
Bioicide	0.5 gpt
Hydrating buffer	0.5 gpt
Microemulsion	1 gpt
Clay stabilizer	1 gpt
Surfactant	1 gpt
Stabilizer pack	10 – 20 gpt
Cross-linking buffer	1 – 2 gpt
Delayed Zr crosslinker	2 – 2.5 gpt
Delayed breaker (encapsulated)	6 pptg

Experimental Studies

Materials

Table 1 shows the recipe for the fluid. The seawater-based

Table 2 *The chemical composition of nanofiltered seawater — actual, synthetic and feed seawater.*

Ions	Feed Seawater (mg/L)	Nanofiltered Seawater (mg/L)	Synthetic Nanofiltered Seawater (mg/L)
Bicarbonate	150	151	103
Barium	< 1	< 1	0.0
Calcium	600	285	213
Chloride	31,589	2,4109	26,400
Magnesium	2,116	299	255
Sodium	17,485	13,733	16,280
Strontium	< 1	3	2.1
Sulfate	4,698	< 50	297
Potassium	789	918	519
TDS	56,638	38,627	44,088

fracturing fluid recipe was prepared using either synthetic nanofiltered seawater or actual nanofiltered seawater. The compositions for the raw seawater, synthetic nanofiltered seawater, and actual nanofiltered seawater are given in Table 2.

Rheology Testing

Linear Gel Hydration Testing

Effective, well-understood, and predictable hydration of the gelling polymer is an important factor in the development of fracturing fluids. This article details the hydration behavior of the selected polymer for use in nanofiltered seawater for the targeted hydraulic fracturing conditions. Linear gel fluids were prepared with polymer loading of 45 ppt. The hydration tests were performed at room temperature using two shear rates viz. 170 s^{-1} and 511 s^{-1}.

The experimental procedure for determining polymer hydration rates and rheology profiling are given as:

- Add required polymer concentrations to a predetermined volume of nanofiltered seawater in a blender.
- Manually set the stirring rate such that a vortex is created with efficient mixing, but maintain the agitation rate sufficiently low to avoid air entrainment in the fluid.
- Add the hydration buffer to facilitate rapid polymer hydration.
- Further mix for 30 seconds before quickly transferring the fluid to the viscometer cup.
- Measure the fluid's viscosity over set time intervals and at a particular shear rate over a 30 minute period using a Model 35 type viscometer equipped with a R1/B1 rotor/bob geometry.

Crosslinked Gel Testing

A Model 50 type high-pressure, high temperature (HPHT) viscometer was used to measure the apparent viscosity of the fracturing fluid samples under different shear rates and temperatures. Tests were performed using a R1/B5 rotor and bob combinations. Viscosity measurements were performed using two shear regimens.

Constant Shear Rate

After formulating the fracturing fluids for the targeted testing temperatures, the rheological properties of the fluid were measured with a Model 50 type HPHT viscometer at a constant shear rate of 100 s^{-1}. The rheological profiles, with and without breakers, were generated at a temperature of 300 °F.

Shear Sweep Testing

Shear sweep testing was conducted to assess the fracturing fluid sensitivity to shear degradation by simulating the shear history during the fracturing operation using the API RP 39[14] schedule under high temperature conditions. The API RP 39 is a well-accepted industry standard for studying the shear response of metal cross-linked fracturing fluids.

The viscosity profiles were generated with and without a breaker at 300 °F. The API RP 39 schedule consists of continuous fluid shearing at a 100 s^{-1} shear rate, and a series of shearing ramps at 100 s^{-1}, 75 s^{-1}, 50 s^{-1}, 25 s^{-1}, 50 s^{-1}, 75 s^{-1}, and 100 s^{-1} once the fluid temperature is within 5 °F of the test temperature and occurring periodically for every 30 minutes.

To ensure the breakdown of fracturing fluid into low viscosity liquid, for effective fracture clean up, upon the conclusion of hydraulic fracturing operation and proppant placement, breaking tests were carried out by adding an in situ breaker to the fluid tested in the rheometer. An oxidative breaker was used in the form of an encapsulated breaker.

Retained Permeability Testing

A coreflooding experiment was conducted to assess the retained permeability in the Berea sandstone core plug, following injection with a filtered broken fracturing fluid. The initial permeability of the core plug was 55 mD, while the porosity was 20.8%. The coreflooding experiment was conducted as per the following procedure:

- Evacuate the core plug samples of air and saturate with a 6 wt% potassium chloride (KCl) brine.
- Load the core plug sample in the core holder.
- Apply 1,000 psi confining pressure and 500 psi backpressure.
- Elevate the oven temperature to 300 °F.
- Inject a 6 wt% KCl brine at different rates to determine the baseline differential pressure.
- Inject nearly 3 PV of broken filtered fracturing fluid at 1 mL/min in the reverse direction.

Table 3 *The water analysis of the typical formation brine used in the test.*

Ions	Values
Barium	3,832 mg/L
Calcium	24,900 mg/L
Magnesium	1,830 mg/L
Potassium	3,889 mg/L
Sodium	78,100 mg/L
Strontium	2,000 mg/L
Chloride	160,000 mg/L
Sulfate	190 mg/L
Carbonate	< 1 mg/L
Bicarbonate	< 1 mg/L
TDS	292,000 mg/L
Total hardness	69,700 mg/L
pH	3.6

- Shut-in the core plug sample for 2 hours.
- Inject a 6 wt% KCl brine and determine the post-treatment differential pressure.

The retained permeability was calculated as: Retained Permeability (%) = [ΔP initial (psi)/ΔP final (psi)] × 100.

Compatibility Testing

The water analysis of a typical formation brine used in the tests is shown in Table 3. The formation brine had near saturation TDS at 292,000 mg/L, and high concentrations of Ba^{2+} and Sr^{2+} ions. The current formation brine can be considered the worst-case scenario brine for the scaling tendency.

Approximately 48 ml (80 vol%) of the nanofiltered seawater and 12 ml (20 vol%) of the formation brine were mixed and placed in the sealed pressure tube. The pressure tubes were placed in an air circulatory oven set at 300 °F for two weeks. The test samples were visually inspected for scaling over a set frequency and at the end of the test.

Results and Discussions

Linear Gel Test

Hydration of the gelling polymer is an essential factor in the development of fracturing fluids. Several tests were conducted to evaluate the hydration behavior of the selected polymer for use in nanofiltered seawater for the targeted hydraulic fracturing conditions. The fluid showed a quick hydration time by achieving a stable viscosity within 3 minutes. Figures 1 and 2 show the viscosity at approximately 100 cP at 170 s^{-1} and approximately 35 cP at 511 s^{-1}, respectively, at ambient temperature.

Fracturing Fluid Rheology Test at 300 °F Using Nanofiltered Seawater

The first set of experiments were performed using synthetic nanofiltered seawater. Initially, experiments focused on utilizing a conventional oxygen scavenger to prevent any thermal degradation of the polymer. When the fluid was subjected to a constant shear regime it was seen that the fluid exhibited an excellent stable viscosity above 300 cP, Fig. 3. Subsequently, as soon as multiple shear regimen was introduced, the fluid undergoes viscosity reduction, Fig. 4. It could be observed that the viscosity of the fluid rapidly decreases within a couple of shear cycles. This could be attributed to high temperature shear degradation of the metal cross-linked fluid.

To mitigate the shear and temperature degradation issue, we introduced a stabilizer package to impart shear resilience to the polymer at high temperatures. The stabilizer package comprised a blend of oxygen scavenger, high temperature stabilizer, and buffer. The stabilizer package controlled the crosslinker reaction rate, thereby imparting the required shear and temperature stability to the fluid. The rest of the fluid development reported herein is comprised of the stabilizer package included in the fluid formulation.

Figure 5 shows that the viscosity of the synthetic nanofiltered seawater-based 50 ppt polymer fluid stayed above 300 cP, at shear rates ranging from 25 s^{-1} and 100 s^{-1} for approximately 110 minutes at 300 °F. A similar fluid with 50 ppt of polymer was prepared with the synthetic nanofiltered seawater, and 6 ppt of encapsulated delayed breaker was added to the fluid. The addition of the encapsulated breaker at 6 ppt effectively reduced the viscosity.

Figure 6 shows the viscosity of the nanofiltered seawater-based fracturing fluid with the breaker. The addition of the breaker reduced the fluid viscosity gradually to less than 30 cP in less than 5 hours, suggesting an excellent break, and therefore cleanup.

In the second set of experiments, actual nanofiltered seawater was utilized. Figure 7 shows that the viscosity stayed above 300 cP (at 100 s^{-1} shear rate) for about 100 minutes at 300 °F using a 47 ppt polysaccharide loading. It can be seen that the fluid also showed a delayed crosslinking behavior with the viscosity starting to rise rapidly at approximately 120 °F.

The third set of experiments were performed with the actual nanofiltered seawater with a 45 ppt polysaccharide loading. The fluid showed a delayed crosslinking tendency as before. It was observed that the viscosity

Fig. 1 *The viscosity of the nanofiltered seawater-based polysaccharide linear gel at 170 s^{-1}.*

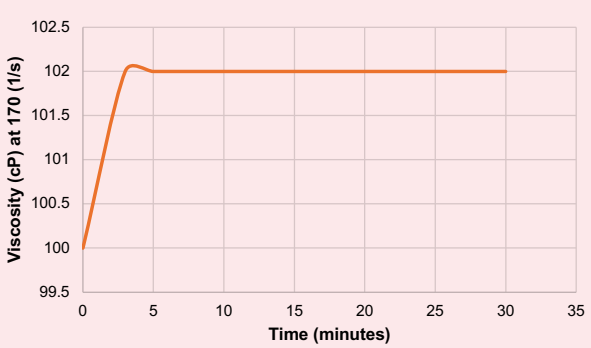

Fig. 2 *The viscosity of the nanofiltered seawater-based polysaccharide linear gel at 511 s^{-1}.*

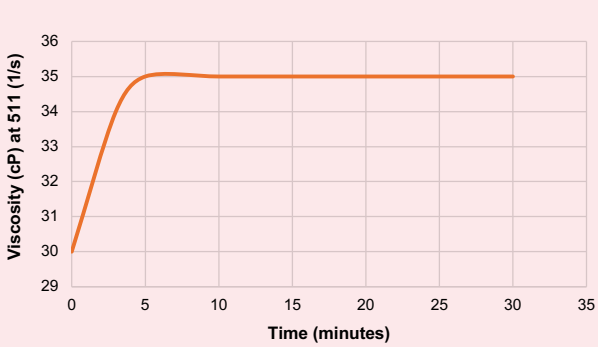

Fig. 3 *The apparent viscosity of the synthetic seawater-based Zr polysaccharide fluid at a constant shear rate, at 300 °F, and without the stabilizer package. The dotted line shows a 300 cP viscosity cutoff.*

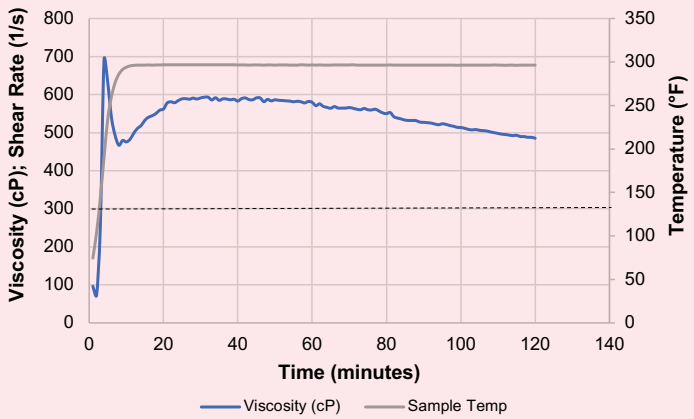

Fig. 4 *The apparent viscosity of the synthetic seawater-based Zr polysaccharide fluid at multiple shear rates, at 300 °F, and without a stabilizer package. The dotted line shows a 300 cP viscosity cutoff.*

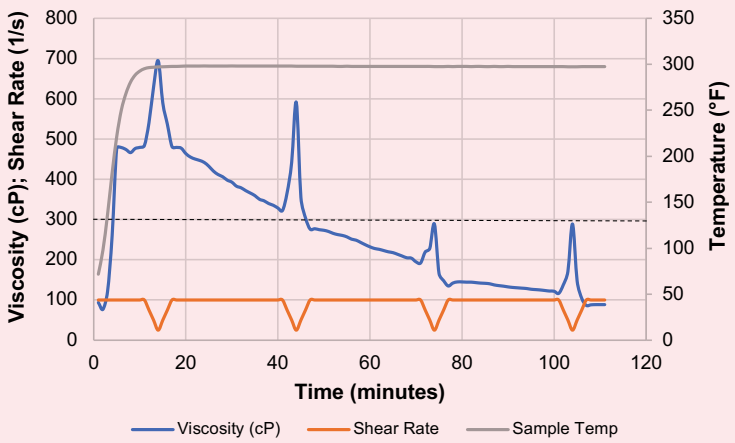

Fig. 5 *The apparent viscosity (50 ppt) of the synthetic seawater-based Zr polysaccharide fluid at multiple shear rates, at 300 °F.*

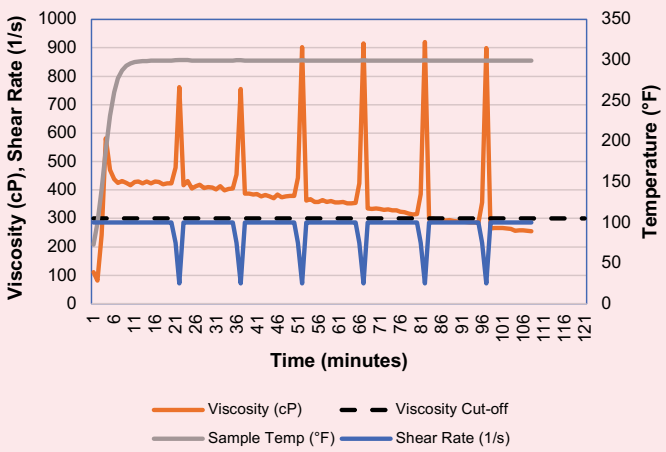

Fig. 6 *The apparent viscosity (50 ppt) of the nanofiltered seawater-based Zr polysaccharide fluid with the addition of 6 ppt of the encapsulated breaker at 100 s^{-1} and 300 °F.*

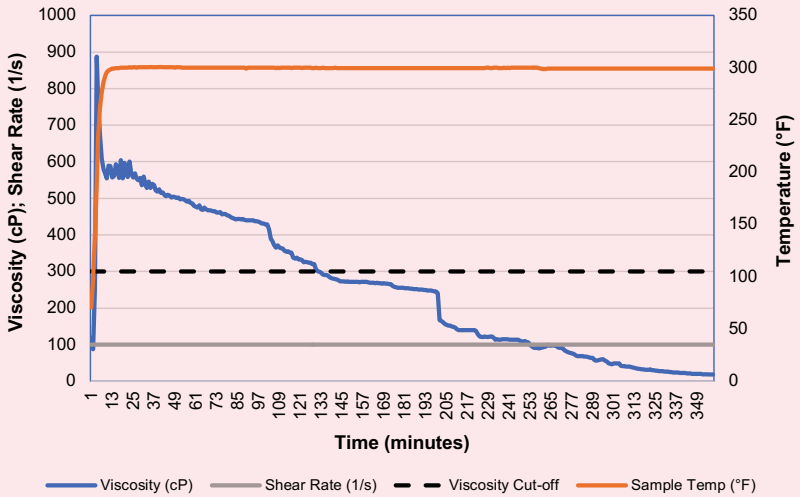

Fig. 7 *The apparent viscosity (47 ppt) of the nanofiltered seawater-based Zr polysaccharide fluid at a constant shear rate, 100 s^{-1} at 300 °F.*

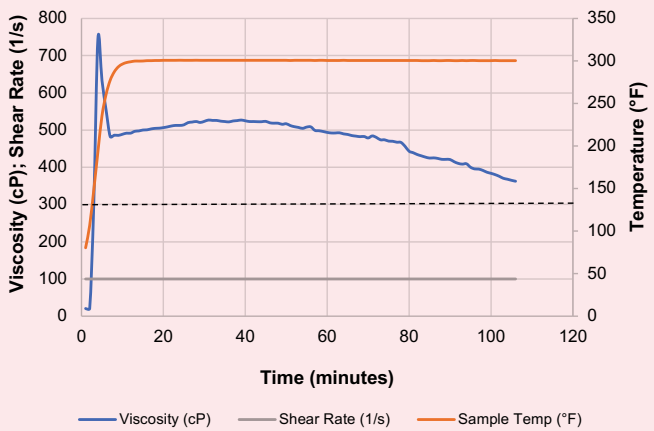

Fig. 8 *The apparent viscosity of the nanofiltered seawater-based Zr polysaccharide fluid at multiple shear rates, at 300 °F.*

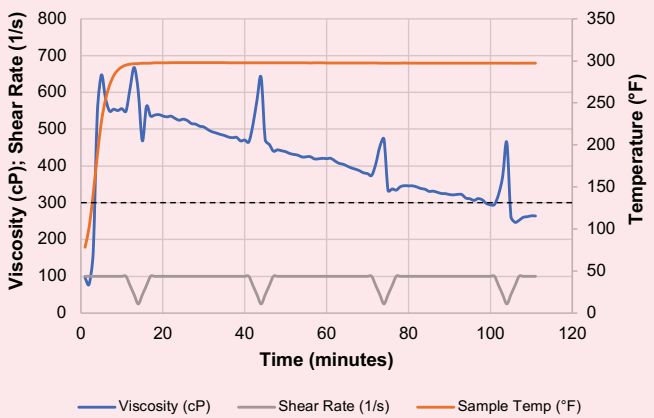

Fig. 9 *The apparent viscosity of the nanofiltered seawater-based Zr polysaccharide fluid with 6 ppt of the encapsulated breaker at multiple shear rates, at 300 °F. The dotted line shows a 300 cP viscosity cutoff.*

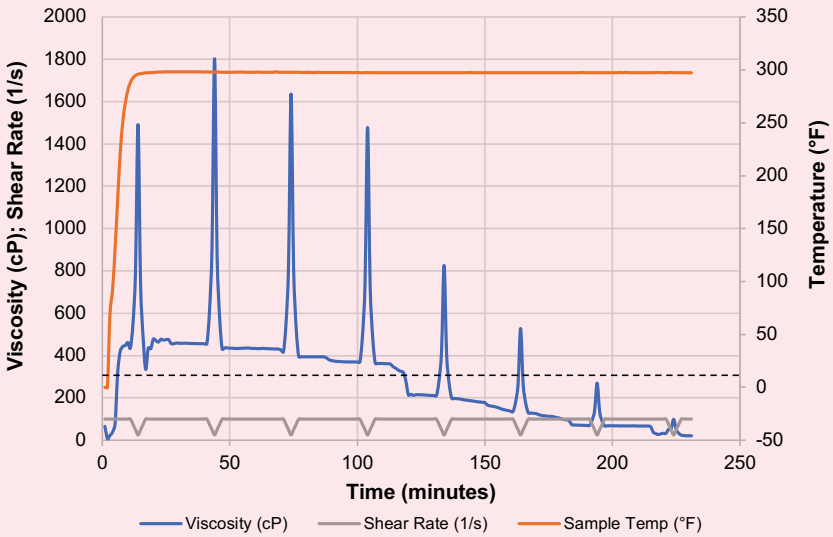

Fig. 10 *The retained permeability of the nanofiltered seawater-based fracturing fluid.*

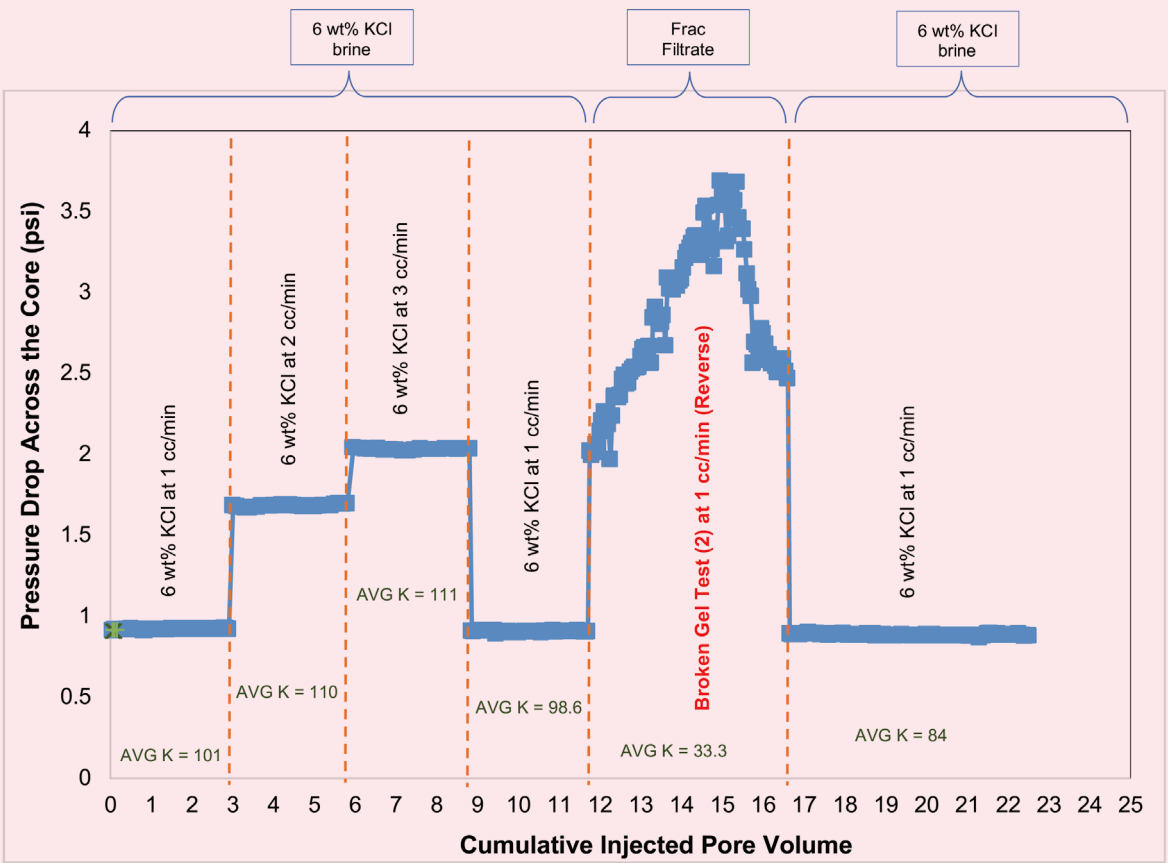

Fig. 11 *The scaling tests at 300 °F for two weeks for the 20 vol% formation brine: 80 vol% the nanofiltered seawater mixture.*

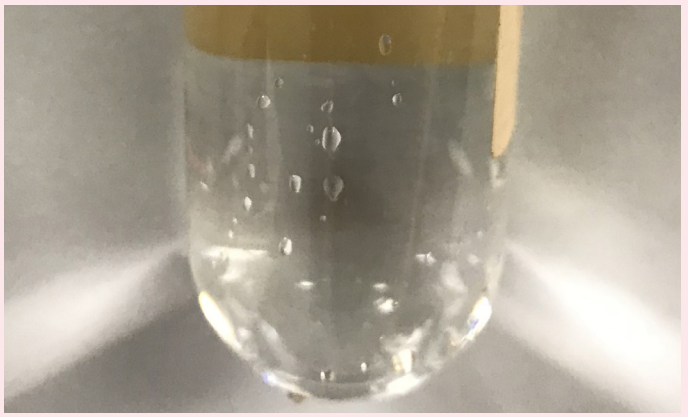

was over 300 cP (at a shear rate ranging from 25 s^{-1} to 100 s^{-1}) for about 100 minutes at 300 °F, Fig. 8. The breaking performance of the fluid was investigated by the addition of a 6 ppt encapsulated breaker. It can be observed from Fig. 9 that there is an effective reduction of viscosity in approximately 3 hours.

Retained Permeability

The retained permeability for the nanofiltered seawater-based fracturing fluid was determined through coreflooding utilizing Berea sandstone core plugs. The testing temperature was 300 °F. During the injection of the fracturing fluid filtrate, the differential pressure across the core plug increased from 0.852 psi to approximately 3.5 psi. When the baseline KCl brine was re-injected, the differential pressure across the core plug decreased and stabilized at nearly 1 psi. The resulting retained permeability is nearly 85.2%, Fig. 10. This regain in permeability indicates excellent fracturing fluid clean-up.

Compatibility Testing

Figure 11 is a photo of the test sample after two weeks of the scaling tests at 300 °F. It can be seen that there is no scale formation after mixing the nanofiltered seawater with high TDS formation water in the ratio of 80:20 by volume.

Conclusions

A new fluid system for hydraulic fracturing applications was successfully developed using nanofiltered seawater.

Based on the lab results, the following conclusions were drawn:

- The nanofiltered seawater-based Zr polysaccharide fluid (45 ppt to 50 ppt) viscosity was > 300 cP at 300 °F over shear rates ranging from 25 s^{-1} to 100 s^{-1} for about 2 hours.
- The addition of a stabilizer package to the fluid provided high temperature and shear stability at temperatures up to 300 °F and multiple shear regimes.
- The addition of an encapsulated breaker at 6 ppt to the 45 ppt and 50 ppt fluids effectively reduced the viscosity.
- The Berea core plugs retained permeability was 85.2% following the injection of the nanofiltered seawater-based Zr polysaccharide fracturing fluid filtrate.

These findings corroborate that the nanofiltered seawater-based fracturing fluid exhibited good stable viscosity, shear resilience, effective breakage, and excellent retained permeability up to 300 °F.

Acknowledgments

The authors would like to thank Fares Alotaibi for his support in conducting the retained permeability experiments.

The article was presented at the Abu Dhabi International Petroleum Exhibition and Conference, Abu Dhabi, UAE, November 15-18, 2021.

References

1. Economides, M.J. and Nolte, K.G.: *Reservoir Stimulation*, 3rd edition, New York: John Wiley & Sons, 2000, 856 p.
2. Economides, M.J. and Martin, T.: *Modern Fracturing: Enhancing Natural Gas Production*, 1st edition, Houston, Texas: Energy Tribune Publishing Inc., 2007, 531 p.
3. Ajayi, B., Aso, I.I., Terry Jr., I.J., Walker, K., et al.: "Stimulation Design for Unconventional Resources," *Oilfield Review*, Vol. 25, Issue 2, Summer 2013, pp. 34-46.
4. Puder, M.G. and Veil, J.A.: "Options, Methods and Costs for Offsite Commercial Disposal of Oil and Gas Exploration and Production Wastes," *SPE Projects, Facilities & Construction*, Vol. 2, Issue 4, December 2007, pp. 1-5.
5. Al-Muntasheri, G.A.: "A Critical Review of Hydraulic Fracturing Fluids for Moderate to Ultra Low Permeability Formations over the Last Decade," *SPE Production & Operations*, Vol. 29, Issue 4, November 2014, pp. 243-260.
6. Bao, C., Han, J., Li, L., Qiao, C., et al.: "A Simulation Study on Mitigation of Water Hardness Damages in Fracturing Fluids," SPE paper 178976, presented at the SPE International Conference and Exhibition on Formation Damage Control, Lafayette, Louisiana, February 24-26, 2016.
7. Glass, J.E., Soules, D.A., Ahmed, H., Egland-Jongewaard, S.K., et al.: "Viscosity Stability of Aqueous Polysaccharide Solutions," SPE paper 11691, presented at the SPE California Regional Meeting, Ventura, California, March 23-25, 1983.
8. Harms, S.D., Gloss, M.L. and Payne, K.L.: "New Generation Fracturing Fluid for Ultrahigh Temperature Application," SPE paper 12484, presented at the Formation Damage Control Symposium, Bakersfield, California, February 13-14, 1984.
9. Satyanarayana Gupta, D.V. and Carman, P.S.: "Methods of Treating a Well with a Gel Stabilizer," U.S. Patent 7,767,630, 2004.
10. Prud'homme, R.K., Ellis, S., Constien, V.G. and Knoll, S.: "Reproducible Rheological Measurements on Crosslinked Fracturing Fluids," SPE paper 18210, presented at the SPE Annual Technical Conference and Exhibition, Houston, Texas, October 2-5, 1988.

11. Prud'homme, R.K., Constien, V. and Knoll, S.: "The Effects of Shear History on the Rheology of Hydroxypropyl Guar Gels," *Advances in Chemistry*, Vol. 223, 1989, pp. 89-112.

12. Kalgaonkar, R. and Patil, P.: "Performance Enhancements in Metal-Crosslinked Fracturing Fluid," SPE paper 152040, presented at the North Africa Technical Conference and Exhibition, Cairo, Egypt, February 20-22, 2012.

13. Kalgaonkar, R. and Patil, P.: "A Novel, Shear-Stable Fracturing Fluid for High Temperature Applications," SPE paper 151890, presented at the SPE Oil and Gas India Conference and Exhibition, Mumbai, India, March 28-30, 2012.

14. API RP39: *Recommended Practices on Measuring the Viscous Properties of a Cross-Linked Water-Based Fracturing Fluid*, 3rd edition, Washington, D.C.: API, May 1998, 32 p.

About the Authors

Dr. Rajendra A. Kalgaonkar

Ph.D. in Polymer Chemistry and Nanotechnology, University of Pune

Dr. Rajendra A. Kalgaonkar is a Petroleum Scientist in the Productivity Enhancement Focus Area of the Production Technology Team at Saudi Aramco's Exploration and Petroleum Engineering Center – Advanced Research Center (EXPEC ARC). He has over 19 years of experience in Research and Development, out of which he spent 11 years in the upstream oil and gas industry.

Prior to joining Saudi Aramco in May 2015, Rajendra worked as a Technology Leader with Halliburton. He has rich experience in areas of nanotechnology; polymer blends and composites while being associated with the National Chemical Laboratory, India, and the University of Western Sydney, Australia.

Rajendra's research is focused on developing new fluids technologies for enhancing hydrocarbon production, including fracturing, sand control, conformance control and acidizing. He has successfully developed new chemistries based on nanomaterials for enhancing hydrocarbon production as well as for drilling fluids.

Rajendra has published 25 patents and patent applications, and 35 peer-reviewed articles, invited book chapters and conference proceedings. He has delivered presentations at Society of Petroleum Engineers (SPE) key advanced technology workshops and forums.

Rajendra received his B.S. degree in Chemistry, an M.S. degree in Polymer Science, and his Ph.D. degree in Polymer Chemistry and Nanotechnology, all from the University of Pune, Pune, India.

Manar M. AlAhmari

M.S. in Biochemistry, Alfaisal University

Manar M. AlAhmari is a Petroleum Scientist in productivity enhancement working with the Production Technology Division of Saudi Aramco's Exploration and Petroleum Engineering Center – Advanced Research Center (EXPEC ARC). She joined Saudi Aramco in October 2019, and her research interests include biotechnology and biochemistry.

Manar's work includes the development of environmentally friendly biotechnological applications to resolve current challenges in vital upstream operations. She is currently working on developing different chemistries, including fracturing fluids and novel chemical methods, for sand control.

Manar is the author/coauthor of a number of scientific publications in international journals and conference proceedings. She is also the inventor/co-inventor of six patents.

Manar received her B.S. degree in Biochemistry from Cardiff University, Cardiff, Wales, U.K. She received her M.S. degree in Biochemistry from Alfaisal University, Riyadh, Saudi Arabia.

Dr. Mohammed A. Bataweel

Ph.D. in Petroleum Engineering, Texas A&M University

Dr. Mohammed A. Bataweel is a Champion for the Productivity Enhancement focus area in the Production Technology Division of Saudi Aramco's Exploration and Petroleum Engineering Center – Advanced Research Center (EXPEC ARC). Mohammed has led his team in the development and deployment of several in-house technologies in Saudi Aramco fields. Throughout his career, he has represented his department on several field development, asset, and multidisciplinary teams.

Mohammed's research interests include formation damage due to drilling and completion fluids, investigation and mitigation of injectivity decline, conformance control, sand production prediction, special core analysis, chemical enhanced oil recovery, productivity enhancement technologies, visualization of fluid flow in porous media, and oil field chemicals.

He is an active member of the Society of Petroleum Engineers (SPE) where he has served on several conferences. Mohammed initiated and co-chaired several SPE advanced technical workshop series in the region. He has published approximately 100 technical papers in local and international conferences and refereed journals, along with a number of patents.

Mohammed received his B.S. degree in Mechanical Engineering from King Fahd University of Petroleum and Minerals (KFUPM), Dhahran, Saudi Arabia, and his M.S. degree in Petroleum Engineering from Harriot-Watt University, Edinburgh, U.K. Mohammed received his Ph.D. degree in Petroleum Engineering from Texas A&M University, College Station, TX.

Mustafa A. Al-Khowaildi

M.S. in Environmental Sciences, King Fahd University of Petroleum and Minerals

Mustafa A. Al-Khowaildi is a Petroleum Engineer in Saudi Aramco's Southern Area Production Engineering Department. He is part of a team that is responsible for gas production engineering and optimization, well completions, well integrity and surveillance, stimulation and well intervention, all while attaining the responsibility to conduct operations in a safe and environmentally sound manner.

In 2015, Mustafa received his B.S. degree in Petroleum Engineering from the University of Oklahoma, Norman, OK, and in 2021, he received his M.S. degree in Environmental Sciences from King Fahd University of Petroleum and Minerals (KFUPM), Dhahran, Saudi Arabia.

Real-Time 3D Anisotropy Analysis Enables Lithology Identification at Distance

Ayman A. Elkhamry, Ahmed Taher, Eduard Z. Bikchandaev and Mohamed M. Fouda

Abstract /

Ultra-deep electromagnetic (EM) inversion is used to resolve multiple layers far from the wellbore. Since it primarily responds to resistivity variations, shale and water-bearing sand layers of similar resistivity values can't be resolved using a traditional resistivity inversion alone. It can be critical to identify the presence of water at a distance, so that a standoff from the oil/water contact can be maintained to optimize production. Analysis of the resistivity alone means that a well path may be optimized to maintain a standoff from any low resistivity zone, to avoid drilling close to a potential water contact.

Identifying the lithology at a distance would remove the uncertainty, allowing a well to be drilled closer to a shale zone or maintaining distance from a water zone to optimize both the well's position and future production. Inversion for resistivity and anisotropy in three dimensions provides a tool that can improve lithological and fluid analysis in real-time, allowing for more sophisticated well placement decisions to be made, and by identifying any critical water-bearing zones at a distance.

Real-time transmission of nine ultra-deep resistivity measurement components allows 3D inversion for both resistivity and anisotropy far away from the wellbore. The interpretation of these inversions is examined in clastic reservoirs where it is critical to differentiate between shale and water-bearing sand layers at a distance from the well trajectory. Although shale zones could have very low resistivity values similar to that seen in water-bearing sand, anisotropy values are generally much higher, due to the laminated nature of the shales. Therefore, mapping resistivity and anisotropy at a distance allows the shale zone to be distinguished from water filled sand in real time, enabling successful geosteering and keeping a desired offset above the water level.

An example is presented where ultra-deep 3D inversion successfully mapped both resistivity and anisotropy. The lithology has a significant impact on the anisotropy; therefore, it was possible to differentiate low resistive shale from the low resistive water-bearing sand at a distance from the well trajectory. This information was used to optimize the geosteering, geomapping, and geostopping processes, and has the potential to be applied to future wells, where applicable. Interpretation results also provide valuable inputs for optimizing completion designs and reservoir management strategies.

This article presents the global first real-time well placement application of 3D resistivity and anisotropy inversions to avoid drilling into a water zone. This novel approach uses ultra-deep azimuthal resistivity technology, which addressed the existing challenge of identifying shale and water filled sand zones of similar resistivities.

Evolution of LWD EM Resistivity

Over the last three decades, the evolution of logging while drilling (LWD) electromagnetic (EM) resistivity has gone through several phases. Since the very early designs, the measurement has depended on firing and receiving EM signals using antennas mounted on the body of the LWD tools. The first LWD resistivity tool was introduced in 1983 with a single frequency, single spacing, and one depth of investigation[1]. After these tools showed reliable results for the formation evaluation[2], further upgrades started to be developed. Rodney et al. (1991)[3] presented one of the first major improvements to the initial design by introducing multiple transmitter-receiver spacing acquiring resistivity measurements at multiple depths of investigation.

Around a decade later, Bittar filed a patent in 2000 about a directional LWD resistivity tool with a tilted antenna to detect anisotropy and formation dip, and another patent in 2002 about a directional resistivity tool for geosteering applications. A few years later, the first deep resistivity geosteering LWD tools came to market[4, 5]. Bittar et al. (2007)[6] describes how the tilted antenna design has helped in geosteering and formation evaluation.

Several years later, the development of ultra-deep resistivity tools capitalized on resistivity tools' evolution and utilized the idea of tilted antennas to build LWD tools with tilted transmitters and receivers. Wu et al. (2018)[7] explained a new multiple collar design used on ultra-deep resistivity tools having longer spacings between transmitters and receivers, a wider range of frequencies and a larger signal-to-noise ratio. This helped

in achieving a much wider range of investigation and enabled inversions of EM measurements to generate wide geological models up to 200 ft from the wellbore (source).

Figure 1 shows the evolution of LWD resistivity measurements.

Component Measurements

The technical innovation achieved through the introduction of tilted transmitters and receivers enabled resolving multiple components of the EM signal. Considering a coordinate system relative to the tool (the tool being along the z-axis), the measured signal can be de-coupled into its constituent parts in every axis of the coordinate system. The impedance marked with Z would have two subscripts identifying each component. The first subscript denotes the transmitter and the second denotes the receiver.

Figure 2 illustrates early versions of LWD EM resistivity, which relied on co-axial transmitters/receivers. This arrangement allowed for only one component of the signal along the tool's axis Zzz and did not have azimuthal sensitivity. Later versions are the LWD EM deep resistivity tools, which had tilted receivers allowing the tool to be sensitive to the x- and z-axis. The sensitivity to the rotational orientation of the tool while drilling allowed one to resolve the y-axis as well.

Figure 3 illustrates the deep resistivity tool's design, which allowed for measuring three components: Zzx, Zzy, and Zzz.

Ultra-deep resistivity tool designs incorporating tilted transmitters as well as receivers allows the tool to acquire a full matrix of nine components, constituting the signal. Figure 4 shows the design of an ultra-deep resistivity tool.

Wu et al. (2018)[7] described the ultra-deep tool design and experimental validation. The field trials of the ultra-deep design allowed showed the tools' capability to provide a 200 ft+ depth of detection of EM signals with a firing signal approximately 1,000 times larger than the non-firing noise.

3D Inversion Using Nine Components

The tilted transmitters and receivers have made it possible to acquire nine components of the EM signal and analyze its sensitivity in all directions of the 3D volume. Utilizing advanced computational techniques, all nine measurement components can be fed in real-time into a 3D inversion algorithm to construct a 3D geological model around the wellbore[8]. Figure 5 shows an example of 3D reservoir visualizations utilizing 3D inversion of the ultra-deep resistivity signal.

Fig. 1 *The evolution of LWD resistivity measurements.*

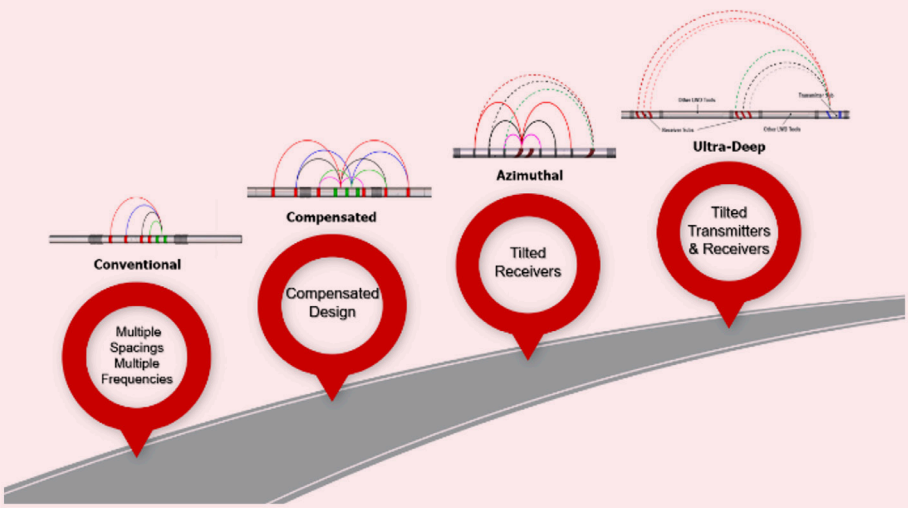

Fig. 2 *The conventional resistivity design and measurement components.*

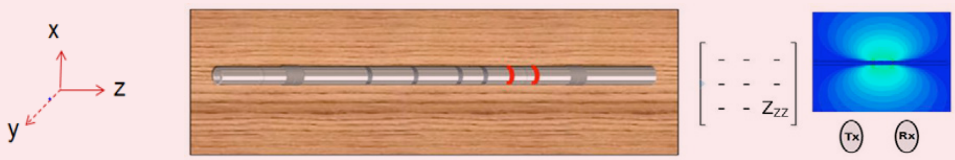

Fig. 3 *The deep resistivity design and measurement components.*

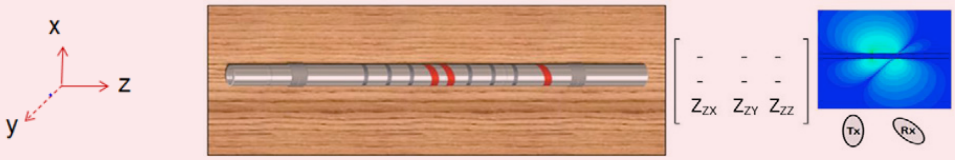

Fig. 4 *The ultra-deep resistivity design and measurement components.*

Fig. 5 *An example of 3D reservoir visualizations utilizing 3D inversion of the ultra-deep resistivity signal.*

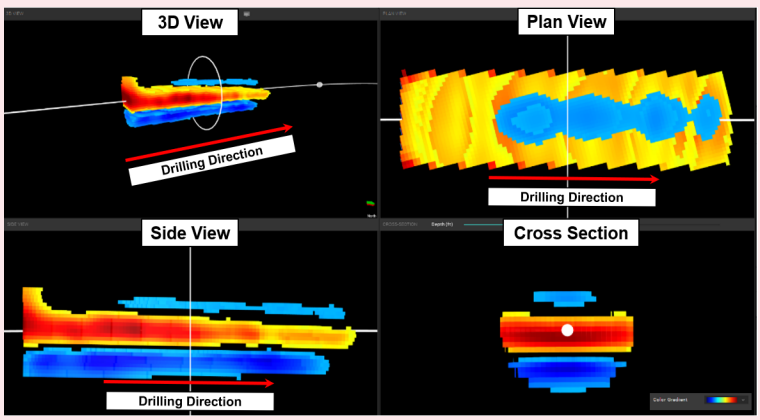

In addition to the 3D reservoir visualization, 3D inversion can be utilized for multiple other real-time applications. The sensitivity toward the three dimensions enables the detection of resistivity boundaries at the right and left of the well path and can therefore be used for geosteering laterally. In addition, 3D inversion allows the mapping of vertical and horizonal resistivity components (Rv and Rh) around the wellbore, which can be used for lithology differentiation at a distance.

3D Resistivity Anistropy Inversion

Shales are known to experience much higher differences between vertical and horizontal resistivity components than sands. Figure 6, by Clavaud et al. (2008)[9], shows how shale and sand zones of very similar resistivity — measured by conventional wireline induction resistivity tools — were differentiated by analyzing the vertical and horizontal resistivities. While sand zones had Rv/Rh values of around l (isotropic), shaly zones had Rv/Rh values up to 4 and above (anisotropic).

Ultra-deep resistivity nine component 3D inversion enables mapping the ratio of vertical and horizontal resistivity components (Rv/Rh) at a distance around the wellbore in the 3D volume and utilized in real-time to differentiate formations of high and low anisotropy even if they have similar values of resistivity. This approach can be used for lithology differentiation and help optimize well placement decisions in real time[10].

This first global geostopping application based on real-time analysis of 3D anisotropy inversion is demonstrated in this article.

Value of Measuring Anisotropy

Understanding lithology will impact well placement decisions, reservoir simulation, and completion design.

Fig. 6 *The shale and sand resistivity anisotropy[9].*

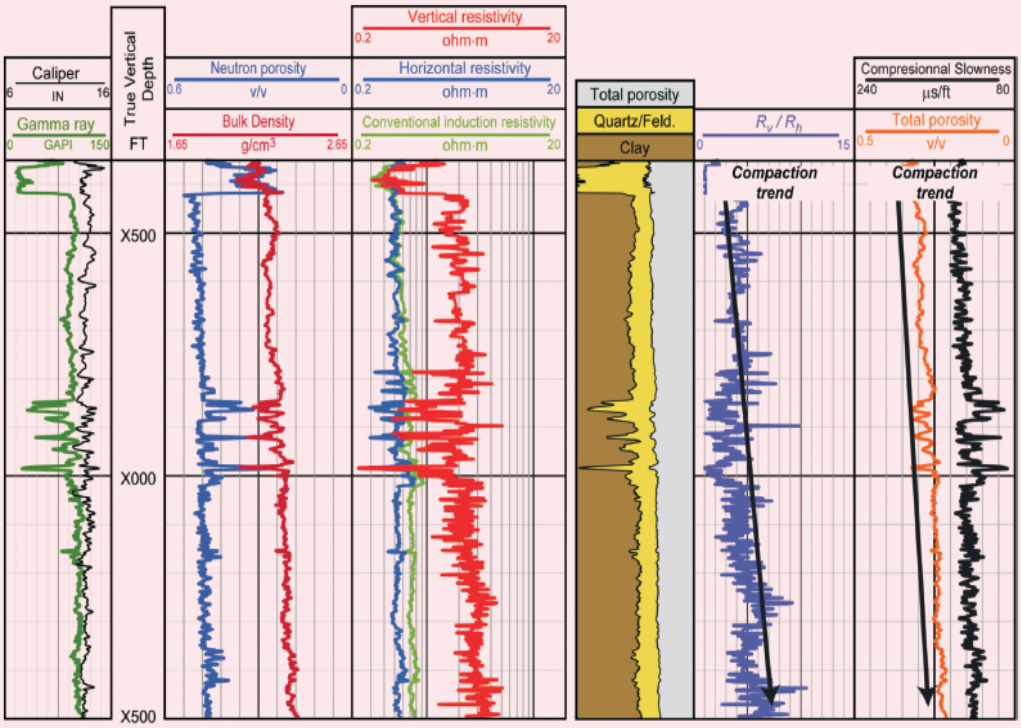

For example, an impermeable shale barrier existing below a horizontal well would prevent water encroachment, which would impact the reservoir productivity; however, a water-bearing sand might be difficult to differentiate from shale that has similar low resistivity without a reliable anisotropy measurement.

Evaluating anisotropy utilizing logging measurements is currently feasible. Such measurements generally have a shallow depth of investigation into the formation, limiting their applications to rock strength and permeability computation. In addition, measurements acquired post-drilling or requiring post-acquisition computation cannot be used for applications requiring real-time decision making.

LWD EM resistivity on the other hand can be used for detecting farther boundaries with resistivity contrast using 2D or 3D inversion mapping, thereby expanding the application to real-time well placement.

The complexity of the geology of meandering sand channels or multilayers of low resistivity contrast is challenging. Combining 3D anisotropy with the 3D reservoir mapping gives a better understanding of the reservoir architecture and fluid at a distance.

Utilizing 3D Resistivity Anisotropy for Well Placement

Globally, the first application utilizing 3D resistivity anisotropy was to avoid drilling into a water zone with a similar resistivity value for the adjacent shale.

The well was an existing producer, and the objective of the horizontal sidetrack was to geosteer in a target hydrocarbon-bearing high resistivity lobe avoiding shale exposure while maintaining a safe distance from possible water contact, Fig. 7. A specified minimum distance had to be maintained from the nearest water contact to ensure a long lifetime for the sidetrack after production starts.

The differentiation between the shale and water-bearing layer was crucial for the well placement strategy and for critical operational decisions when the trajectory approaches the water level. In addition, this is an important input for the completion design.

Offset Well Analysis

Several scenarios utilizing data from offset wells have been reviewed for detailed analysis, Fig. 8. The main scenario was decided based on the most recent data in the area and proximity to the target well.

Triple combo data from the several offset wells were examined, Fig. 9. Due to different times at which the offset wells were logged, most of them had different characteristics from the most recent one, which showed the signature of water present below the target. The water level cannot be accurately mapped in an active production environment.

A deeper investigation of offset wells also showed some uncertainty in resistivity contrast as some shale zones were falling around the resistivity threshold set for the water-bearing layer. This added an additional challenge to geosteering planning as the differentiation between

Fig. 7 *A graph of the location for the target and offset wells.*

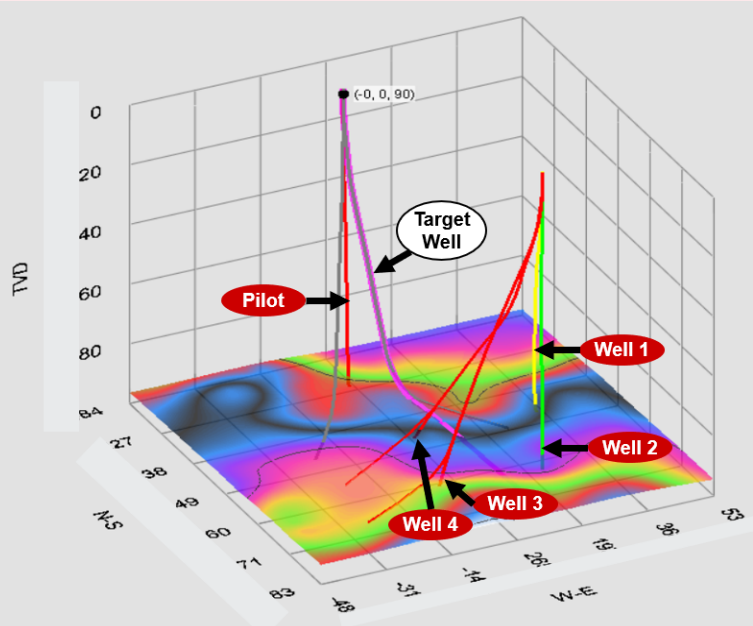

Fig. 8 *Data from the offset wells for analysis.*

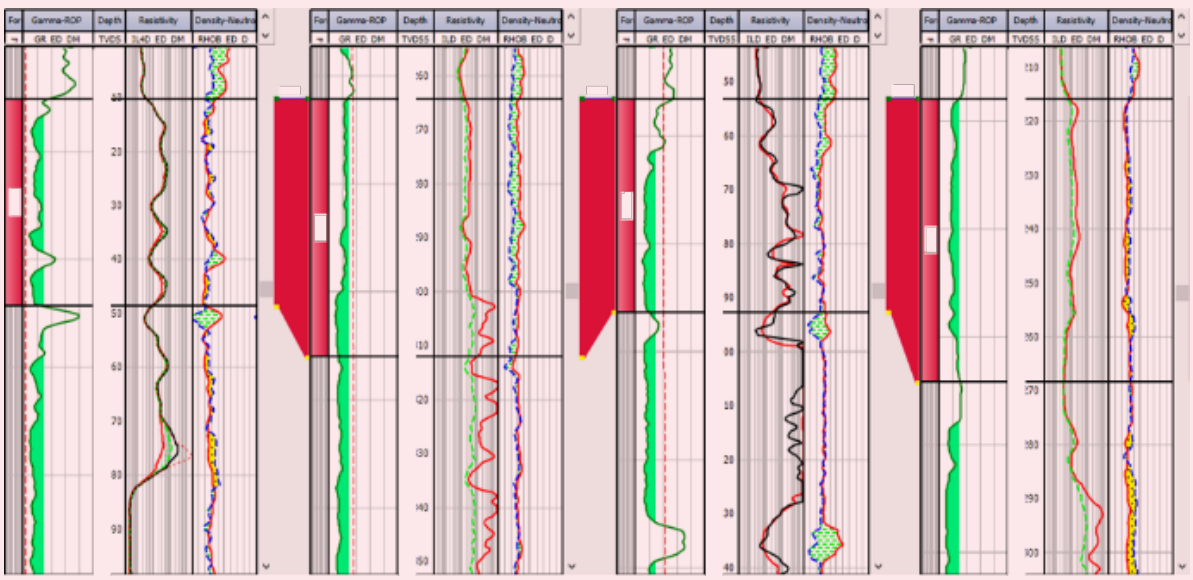

shale and water-bearing zones is crucial while drilling.

Varying Hydrocarbon Water Contact in the Field

Using ultra-deep resistivity data of multiple wells in the same field, an intensive multiwell study has been done to map the water level in the field. Figure 10 is a top view of three wells in the vicinity being drilled horizontally. The black lines represent the well paths and the colors at areas around each well indicate the mapped low resistivity level for every well.

Well Placement Strategy

Considering the complex reservoir characteristics and dynamics, the execution plan was utilizing the following tools while geosteering:

Fig. 9 *The wireline logs from the same field showing shale zones of very low resistivity.*

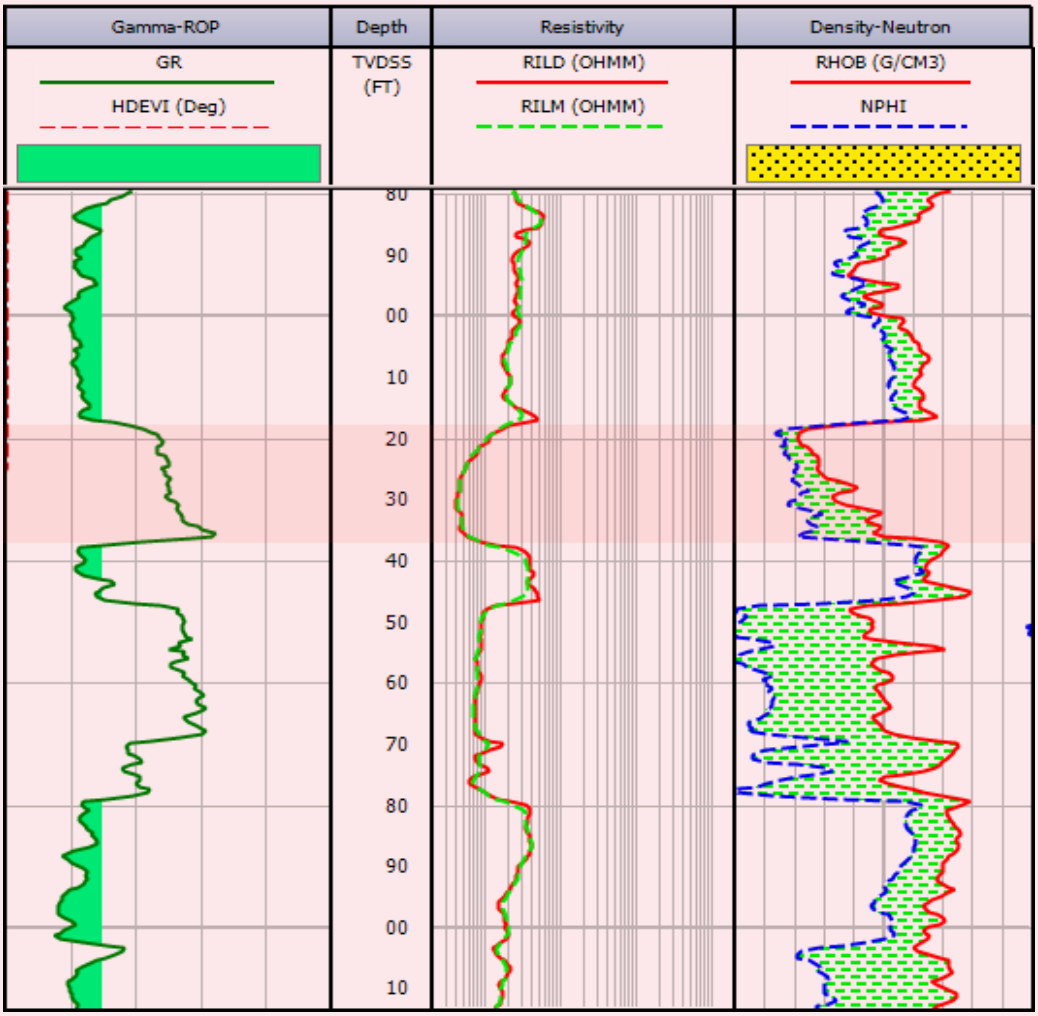

Fig. 10 *A top view of three wells in the vicinity being drilled horizontally. The colored areas around each well indicate the mapped low resistivity level for each well.*

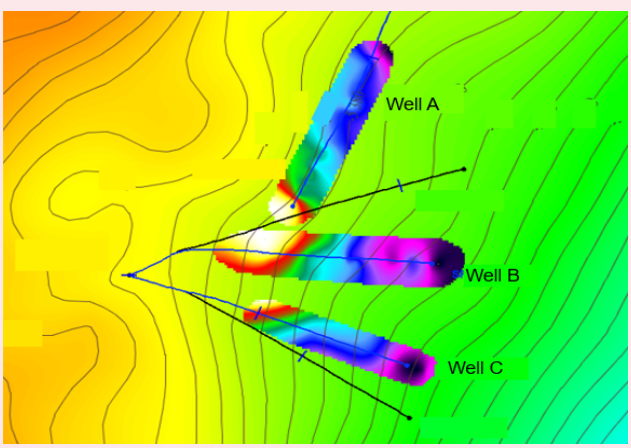

1. LWD triple combo for real-time formation evaluation and well placement.
2. Ultra-deep resistivity with 3D resistivity and anisotropy inversions to:
   - Identify the thickness and formation dip of the resistive target zone.
   - Map the distance to the conductive zones.
   - Confirm if the conductive zones are shale or a water-bearing layer.

The plan has been set to stop drilling if the conductive zone below the target is confirmed to be water-bearing and mapped to be less than a certain distance away from the well path. If the conductive zone, however, is confirmed to be shale, drilling can continue with no limitation on its proximity as the impermeable shale can act as a barrier.

Real-Time Execution

Ultra-deep resistivity inversion was run in real-time

Fig. 11 *The real-time 3D resistivity inversions without filtering.*

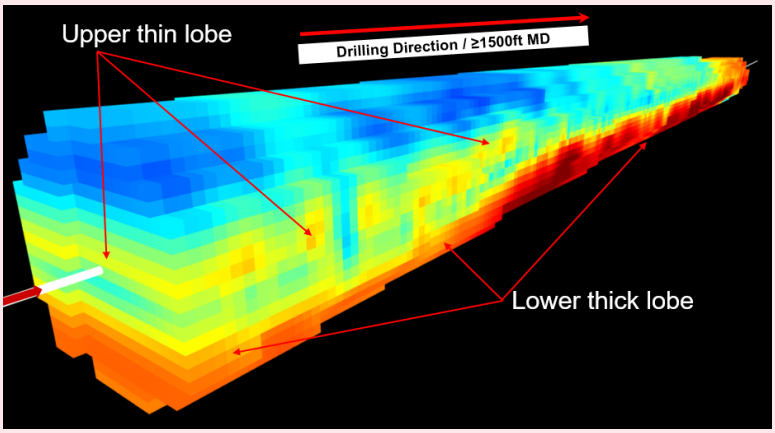

Fig. 12 *The real-time 3D resistivity inversions with filtering.*

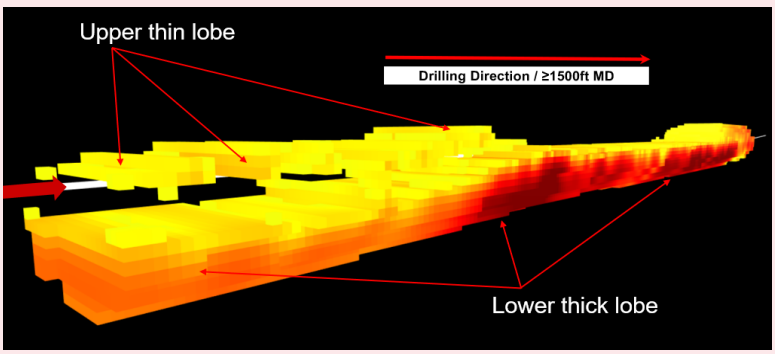

to support geosteering decisions. The well was successfully steered into a resistive zone. The target layer was mapped while drilling and slightly thinning toward the end of the well. The formation dip from the top side was slightly up with some local variations.

Multiple layers of different resistivity were mapped in real-time. In the initial part, the inversion was able to display the pinching out of an upper lobe and the presence of the lower lobe below the well. Another resistive zone was mapped ~20 ft above the target, which has shown a deteriorating quality in the drilling direction, Figs. 11 and 12.

3D resistivity inversion of the volume around the wellbore confirmed and supported the interpretation done using the 1D inversion. Figure 13 shows the real-time 1D and 3D inversion views.

3D anisotropy inversion was successfully used to identify lithology below the well path and confirmed mapping of the conductive water-bearing zone. Meanwhile, the low resistivity, high anisotropy zone on top of the well path was identified as a shale layer. Figures 14 and 15 show the comparison of the 3D resistivity and 3D anisotropy inversions.

Upon entering the anisotropic layer on top, conventional logging tools confirmed the presence of shale based on gamma ray and density/neutron measurements.

Upon entering the target layer, the water level was mapped and drilling stopped upon reaching the minimum specified distance. Geosteering decisions made in real-time while

Fig. 13 *The real-time 1D and 3D resistivity inversions and LWD data.*

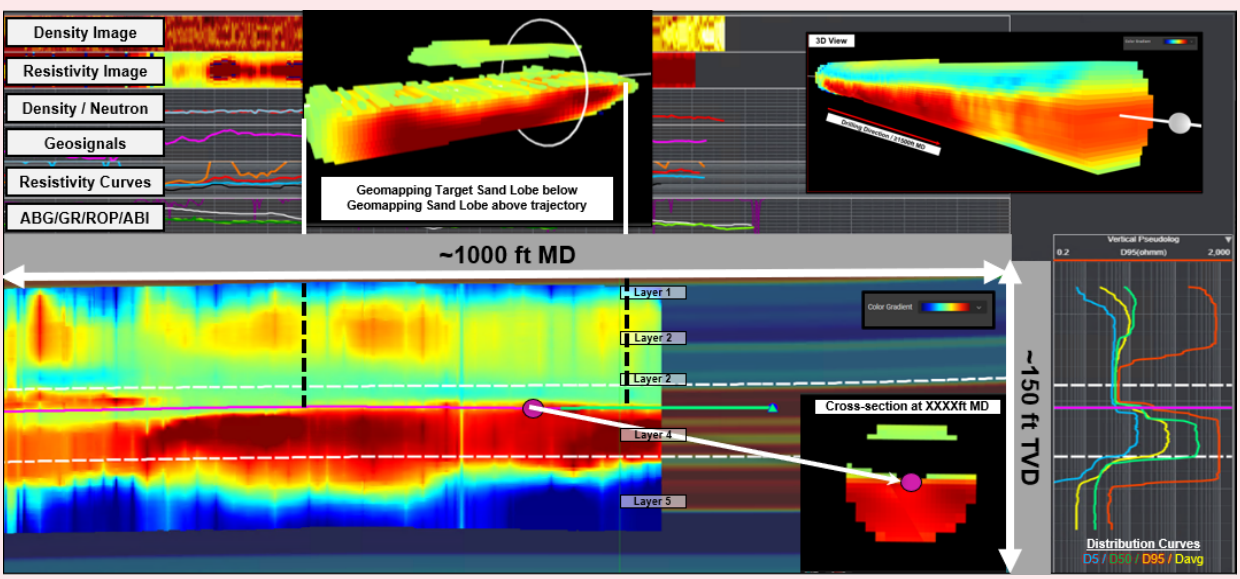

Fig. 14 *The real-time 3D resistivity and 3D anisotropy inversion.*

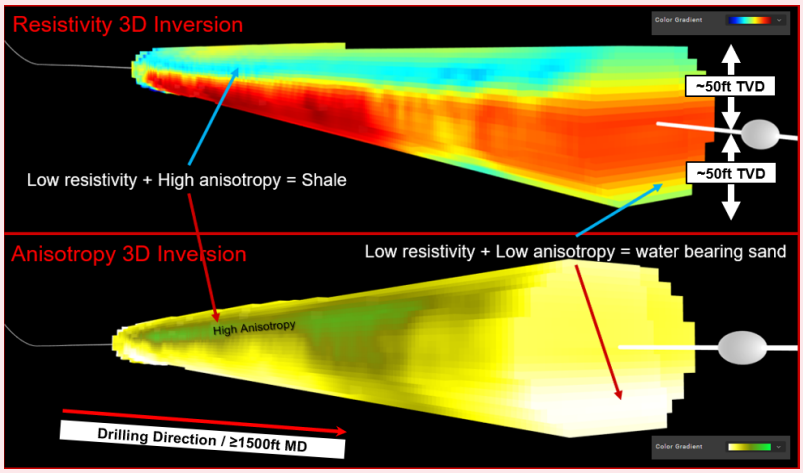

Fig. 15 *The real-time 3D resistivity and 3D anisotropy inversions with tight scale and filtering for multilayering.*

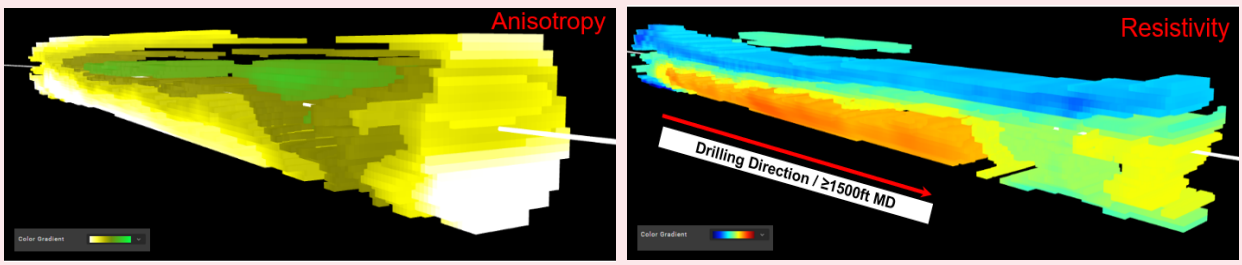

drilling enabled optimum well placement.

Conclusions

The latest evolution of LWD resistivity tools has enabled the use of nine resistivity components for ultra-deep resistivity inversion. This enables multiple advanced solutions such as resolving the reservoir architecture in three dimensions and anisotropy for lithology and fluid differentiation.

3D resistivity and anisotropy inversions were run in real-time and utilized for the first time globally to aid well placement decisions. Successful mapping of the nearby conductive zone and identification of its lithology has enabled a confident decision to stop drilling and place the well at the desired zone.

Acknowledgments

This article was prepared for presentation at the SPWLA 63rd Annual Logging Symposium, Stavanger, Norway, June 11-15, 2022.

References

1. Rodney, P.F., Wisler, M.M., Thompson, L.W. and Meador, R.A.: "The Electromagnetic Wave Resistivity MWD Tool," SPE paper 12167, presented at the 58th Annual Technical Conference, San Francisco, California, October 5-8, 1983.
2. Coope, D.F. and Yearsley, E.N.: "Formation Evaluation Using EWR Logs," SPE paper 14062, presented at the International Meeting on Petroleum Engineering, Beijing, China, March 17-20, 1986.
3. Rodney, P.F., Mack, S.G., Bittar, M.S. and Bartel, R.P.: "An MWD Multiple Depth of Investigation Electromagnetic Wave Resistivity Sensor," SPWLA paper presented at the SPWLA 32nd Annual Logging Symposium, Midland, Texas, June 16-19, 1991.
4. Al-Mudhhi, M.A., Ma, S.M., Al-Hajari, A.A., Lewis, K., et al.: "Geosteering with Advanced LWD Technologies — Placement of Maximum Reservoir Contact Wells in a Thinly Layered Carbonate Reservoir," IPTC paper 10077, presented at the International Petroleum Technology Conference, Doha, Qatar, November 21-23, 2005.
5. Zhang, Z., Gonguet, C., Rajani, V. and Roeterdink, R.: "Directional LWD Resistivity Tools and Their Business Impacts," paper presented at the SPWLA 49th Annual Logging Symposium, Austin, Texas, May 25-28, 2008.
6. Bittar, M.S., Klein, J., Beste, R., Hu, G., et al.: "A New Azimuthal Deep-Reading Resistivity Tool for

Geosteering and Advanced Formation Evaluation," SPE paper 109971, presented at SPE Annual Technical Conference and Exhibition, Anaheim, California, November 11-14, 2007.

7. Wu, H-H., Golla, C., Parker, T., Clegg, N., et al.: "A New Ultra-Deep Azimuthal Electromagnetic LWD Sensor for Reservoir Insight," paper presented at the SPWLA 59th Annual Logging Symposium, London, U.K., June 2-6, 2018.
8. Clegg, N., Parker, T., Djefel, B., Monteilhet, L., et al.: "The Final Piece of the Puzzle: 3D Inversion of Ultra-Deep Azimuthal Resistivity LWD Data," paper presented at the SPWLA 60th Annual Logging Symposium, The Woodlands, Texas, June 15-19, 2019.
9. Clavaud, J-B.: "Intrinsic Electrical Anisotropy of Shale: The Effect of Compaction," *Petrophysics*, Vol. 49, Issue 3, June 2008, pp. 243-260.
10. Alkhars, A., Achong, C., Fouda, M. and Bikchandaev, E.: "3D Inversion and 3D Anisotropy Analysis Improve Real-Time Decision Making Process in Complex Clastic Reservoirs," IPTC paper 22204, presented at the International Petroleum Technology Conference, Riyadh, Saudi Arabia, February 21-23, 2022.

About the Authors

Ayman A. Elkhamry

B.S. in Mechanical Engineering, Ain Shams University

Ayman A. Elkhamry is a Petroleum Engineering Consultant working in Saudi Aramco's Reservoir Description and Simulation Department. He started his career as a Wireline Logging Engineer. Ayman has held several technical and managerial positions before joining Saudi Aramco. His experience includes taking part in various automation, artificial intelligence and remote operation projects, and managing the deployment of several formation evaluation and well placement technologies.

Ayman is a member of a number of professional societies, including the Society of Petroleum Engineering (SPE) and the American Society of Mechanical Engineers (ASME).

He received his B.S. degree in Mechanical Engineering from Ain Shams University, Cairo, Egypt.

Ahmed Taher

M.S. in Petroleum Engineering, Heriot-Watt University

Ahmed Taher is Geoscience Domain Champion and technical team lead at Halliburton Sperry Drilling in Saudi Arabia. He began his career as a logging while drilling (LWD) field and real-time operations engineer, and LWD service coordinator. Ahmed then became the technical advisor for a deepwater project for Saudi Aramco before leading the Geoscience team for Halliburton in Saudi Arabia and Bahrain.

He is a member of the Society of Petroleum Engineers (SPE) and the Society of Petrophysicists and Well Log Analysts (SPWLA).

Ahmed received his B.S. degree in Petroleum Engineering from Cairo University, Giza, Egypt, and his M.S. degree in Petroleum Engineering from Heriot-Watt University, Edinburgh, Scotland, U.K.

Eduard Z. Bikchandaev

Diploma of Economics and Management, Tyumen State Oil and Gas University

Eduard Z. Bikchandaev is Senior Geoscience Advisor for measured/logging while drilling and geosteering at Halliburton Saudi Arabia. He began working with Halliburton in 2007 as a Field Engineer in Russia, then moved to the geosteering domain. Eduard led the geosteering team in Russia, and since 2019, he has been leading the team in Saudi Arabia.

Eduard is a member of the Society of Petroleum Engineers (SPE) and the Society of Petrophysicists and Well Log Analysts (SPWLA).

He received his Diploma of Drilling Engineering and also his Diploma of Economics and Management from Tyumen State Oil and Gas University, Tyumen, Russia.

Mohamed M. Fouda

B.S. in Electrical Engineering, The American University

Mohamed M. Fouda is Geoscientist and logging while drilling (LWD) Technical Advisor at Halliburton Sperry Drilling in Saudi Arabia. He started his career as a software engineer in Egypt. Mohamed then moved to the oil and gas industry as a measured/LWD Field Engineer in Saudi Arabia.

He participated in several assignments in Houston Training, Houston Technology and led the field launch of the Azimuthal Deep Resistivity service in Saudi Arabia and the UAE. Mohamed then took several assignments in Sperry Saudi, such as LWD competency champion, Remote Operations Center senior engineer and service coordinator for different areas in Saudi Arabia and Bahrain.

He is a member of the Society of Petroleum Engineers (SPE) and the Society of Petrophysicists and Well Log Analysts (SPWLA).

Mohamed received his B.S. degree in Electrical Engineering from The American University, Cairo, Egypt.

Developing an Integrated Solution to Remove and Inhibit Asphaltene Deposits through a Laboratory and Field Proven Approach

Hussain A. Almajid, Alaa S. Shawly and Abdullah AlQassem

Abstract /

Asphaltene deposits are considered one of the most common issues facing oil fields with low particle stability that can result in the loss of well potential, jeopardize wellbore accessibility, and cause premature electric submersible pump failures. Traditionally, these deposits are treated with hydrocarbon-based solvents, which have low flashpoints, making them hazardous and expensive.

The objective of this article is to provide a comprehensive solution to effectively remove asphaltene and sand fill accumulation that forms in the near wellbore region. This article will also provide a computational analysis to accurately predict asphaltene precipitation during the production phase for the optimized inhibition process.

A laboratory approach was implemented to test the effectiveness of different water-based solvent types, including aromatic, aliphatic, and heteroatom, instead of the commonly used hydrocarbon solvents, e.g., xylene, to dissolve asphaltene samples collected from the field and placed under anaerobic conditions. A thorough evaluation of fundamental asphaltene properties, including saturates, aromatics, resins, and onset pressure, is incorporated into a computational model to understand and accurately predict asphaltene precipitation behavior.

The newly developed system offers significant advantages compared to the traditional system in terms of treatment effectiveness, deployment cost and health, safety, and environment due to its relatively high flashpoint. The new system utilizes a water-based solvent that leaves the formation in a water-wet state instead of oil-wet, thereby creating a barrier layer that will delay asphaltene accumulation and reduce treatment frequency.

Field implementation and post-job results utilizing this newly developed water-based aromatic solvent will be discussed, including treatment effectiveness to dissolve downhole asphaltene accumulations. Asphaltene inhibition programs have been implemented based on the results acquired from this model, and frequently conducted inspections showed no asphaltene deposition over extended production periods.

This article provides a laboratory proven and field-tested water-based aromatic solvent that is effective in dissolving asphaltene accumulations resulting in improved well potential while reducing the frequency of required treatments, thereby maximizing productivity. This system is unique as it provides a high flashpoint water/solvent mixture with solvency power often greater than xylene with the additional benefit of leaving the formation strongly water-wet. The developed computational model helped to reduce the treatment frequency resulting in reduced expenses and sustained production.

Introduction

Asphaltene deposits are commonly referred to as black and carbonous compounds that usually exist in the form of colloidal, suspended, and solid particles. These solid compounds are normally insoluble in light paraffin hydrocarbon solvents, e.g., pentene or petroleum ether. Asphaltene precipitation is affected by several parameters/wellbore conditions and it typically occurs when the reservoir fluid loses its ability to keep the particles dispersed and suspended. As such, these particles begin to stabilize and asphaltene deposition occurs.

The stability of asphaltene molecules inside the crude oil is affected by several factors, including pressure drop, changes in temperature, oil composition, formation rock properties, and type of deployed completions. A single, or a combination of these factors, can directly impact the suspension forces holding these particles in the crude oil or what is referred to as "resins," and therefore result in asphaltene precipitation. This phenomena can be manifested at any stage during the production phase as the fluid travels from the reservoir section all the way to the surface.

At any point of sudden pressure and temperature changes, asphaltene particles may begin to flocculate from the hydrocarbon fluids and begin to form asphaltene deposits. The existence of emulsified fluids and droplets

can increase the flocculation rate, and consequently, the asphaltene precipitation. As such, the treatment design must take into consideration the existence of emulsified fluids, and additives must be utilized to enhance the separation process to leave the rock surface as water-wet.

The asphaltene composition and precipitation method are key aspects that shall be taken into consideration to achieve effective treatment results and identify the root cause for precipitation and subsequent counter measures. Several solid samples were collected from the field to perform lab analysis and study the compositional content of these samples under anaerobic conditions. Furthermore, crude oil samples were collected from these fields, and changes in pressure and temperature were applied on these samples to understand the precipitation process and rate.

Asphaltene Precipitation Process

A key aspect in the asphaltene precipitation process is the sudden change in thermodynamic conditions as the fluid travels from the reservoir section to the surface. Extensive work has already been conducted to study this chemical interaction to determine the main factors that impact the asphaltene precipitation process, e.g., the thermodynamic changes and the composition of the crude oil that plays a major role in the flocculation rate, solid deposition, and adherence to the completion surfaces.

Also, the amount of low molecular weight resins can affect the asphaltene deposition volume on the rock surface since this can decrease the stabilization within the fluid. The number of polar particles in the asphaltene solids will impact the adherence strength to the rock and completion surface. The existence of emulsified fluids and droplets can adversely impact the particle stability, and thereby increase the flocculation rate.

Asphaltene Prevention Procedure

Two approaches have been explored to determine the best method to delay and if possible prevent asphaltene deposition. Once the precipitation process has been carefully examined, the main elements, which affect the flocculation rate, have been identified. Subsequently, control measures can be employed to effectively delay the precipitation process.

The first approach focused on controlling the thermodynamic conditions since the crude oil goes through several changes in pressure and temperature as it travels from the reservoir section to the surface. Laboratory testing showed that temperature changes had a more severe impact on asphaltene precipitation compared to the pressure drop. The lab test results showed that asphaltene stability and flocculation can occur due to the solubility of these particles in the crude oil. Wells completed with downhole restrictions and throat flow path played a major role on the pressure drop, and consequently, resulted in more asphaltene precipitation.

The composition of the crude oil plays a factor in this process where wells with a high gas volume fraction shows a higher tendency to flocculate asphaltene particles due to the heat capacity and heat coefficient for gas compared to oil. The asphaltene precipitation process is governed by the ratio of paraffin and aromatic in the crude oil. The reservoir changes in the thermodynamic conditions allow the paraffin to expand higher than the aromatic the higher the flocculation rate is, and therefore causes asphaltene precipitation. Achieving the optimum production rate and optimizing the well completion design is essential to reduce thermodynamic changes to minimal.

The flocculation point of crude oil was studied utilizing standard industry inhibition products such as Tarchek. Figure 1 shows the results of these studies.

The second approach focused on modifying the surface coating for the formation rocks and well completion surfaces by changing these surfaces from water-wet to oil-wet. These inhibitors create a film layer that act as a barrier, which serves as a buffer that prevents asphaltene formation. In addition, lab analysis was conducted to study the impact of inhibitor additives that directly disperse paraffin atoms in the crude oil and reverse the flocculation process.

For these inhibitors to be effective, they shall be applied during the early stages of production where minimal asphaltene is present, so it is much easier for these chemicals to adhere to the reservoir rock and completion surfaces. Therefore, a proper wellbore clean out job must be conducted prior to applying these chemicals to ensure a maximum adherence capability, and subsequently, higher efficiency from this treatment.

Thereafter, the inhibition process can be started for both the well tubulars and formation rocks. While it is relatively easy to clean the well tubulars utilizing mutual solvents and then applying the inhibitor, the inhibition process for the formation rocks requires additional work. In other words, a continuous injection process

Fig. 1 *Crude oil flocculation point trend with and without an asphaltene inhibitor.*

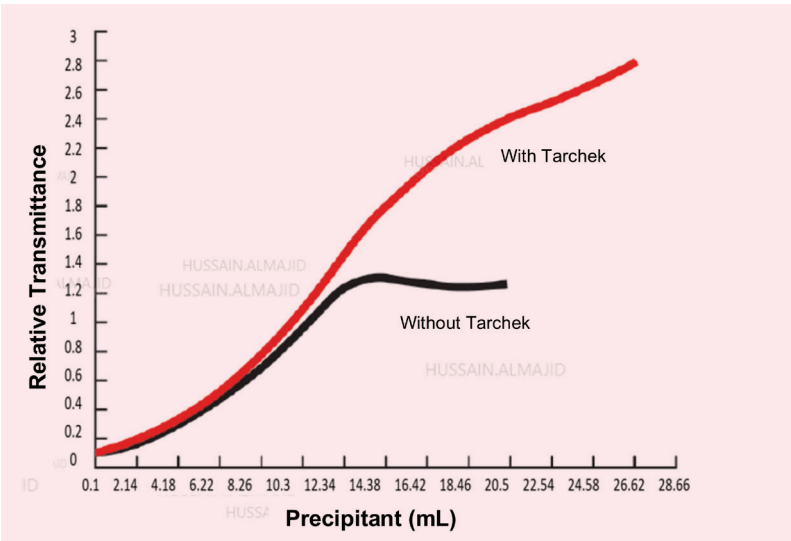

can be conducted for the well tubulars by placing an injection port as close as possible to the production packers. Meanwhile, an inhibition squeeze job followed by overflush fluids must be conducted based on an established frequency to ensure effective inhibition for the formation rocks. Emulsion can have a severe damaging effect on the formation, as has been demonstrated both in the well and in the laboratory; therefore, in general, emulsion should be avoided when possible[1].

Laboratory Procedure and Approach

The ideal approach when removing asphaltene deposition is to ensure that the formation rock and well tubular surface are left in a water-wet state post-treatment completion to delay the re-deposition process as much as possible. This laboratory approach utilized coreflooding experiments along with asphaltene samples collected from the field to test the effectiveness of this novel water-based solvent to remove asphaltene deposition and leave the formation rock in a water-wet state. The dissolution rate and capabilities were an essential objective for this laboratory study, and so different compositions for solid asphaltene samples were tested to measure the dispersion effective for this solvent.

Another key element for this experimental approach was to verify the polar strength for this solvent, which can dissolve and break the molecular bonds for the asphaltene deposits[2]. During the early stages of the removal process, particles with low polar strength will be dissoluted; initially, however, some of the most polar and heavy molecular weight particles will still remain, leaving the surface rock oil-wet and asphaltene re-deposition can occur within a short period. Consequently, the solvent must have enough polar strength to dissolute as much as possible of these deposits and hold them inside the crude oil, thereby preventing the re-deposition process. In short, the goal for this laboratory approach is to develop a solvent that efficiently dissolutes asphaltene while maintaining a high polar strength and can leave the formation pores in a water-wet state, thereby preventing or delaying the re-absorption process as much as possible[3].

The developed solvent must be able to ultimately restore the well productivity and wellbore accessibility while not creating any formation damage in the process. A comparison was conducted to analyze the solubility of the developed water-based solvent against oil-based fluids, Fig. 2.

Several asphaltene samples were collected from the field and synthetically made in the lab to test the effectiveness of the newly developed solvents. It's also worth noting that the composition of asphaltene samples varied from one another in terms of composition and molecular weight. As such, the alkanes' production was utilized to distinguish between them by using a light alkane, e.g., methane and ethane, which tend to precipitate asphaltene with a lower molecular resin. Meanwhile, heavy alkanes, e.g., octane and nonane, tend to precipitate asphaltene with higher molecular resin[4].

Nevertheless, it's important to keep in mind that samples collected from the field differ from the laboratory's synthetically made samples due to the higher fraction of the polar and insoluble asphaltene precipitates. X-ray diffraction (XRD) analysis was conducted on the collected samples to identify the existing quantities of asphaltene, paraffin, organic, and inorganic materials present in these samples.

Several field trials were conducted utilizing oil-based solvents with a high flashpoint, e.g., xylene and toluene, which had only minor success in the dissolution process and created an oil-wet state, therefore,

Fig. 2 *The amount of dissolved asphaltene in oil-based (red) vs. water-based (blue) solvents.*

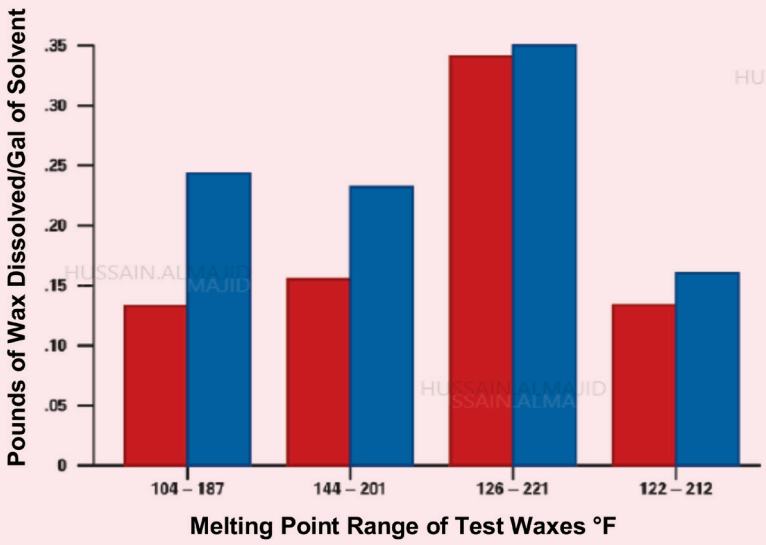

precipitation occurred at a much faster rate[5]. Finally, extra precautions must be considered while carrying out the field execution since uncertainty factors cannot be accounted for in the laboratory results, such as the location where the sample was acquired, the molecular weight for these deposits, the polar magnitude, resin strength, existing pressure, and temperature.

Job Design and Planning

An adequate quantity of the samples was collected from the field to test the effectiveness of this solvent under anaerobic conditions, which are a close representation of the actual well conditions, and then the amount of residue present after applying these solvents was assured. The results showed that hydrocarbon-based solvents with a high flashpoint had much more residue remaining when compared to this water-based solvent[6]. A baseline was established by testing the dissolution strength for the oil-based solvents, and the same samples were subjected to water-based solvents to compare the results for both. The solvent fluid, e.g., pyrrolidone, was added for both the oil and water solvents to further enhance the dissolution process, and then the results were compared for both.

It was evident while conducting the field trial that removing asphaltene deposits with higher molecular polarity using an oil-based solvent had a higher chance to re-precipitate these deposits again. This was confirmed post-pumping of the treatment fluids during the job, and the well was isolated for short periods. Then, an additional run was performed to confirm the maximum reach depth, which showed that the asphaltene had re-deposited again since the oil-based solvent become saturated and resin began to flocculate and fallout. As a result, this proved that the current utilized oil-based solvent had only temporary effects and does not provide a long-term solution.

Therefore, water-based solvents were developed and tested in the field that can achieve efficient dissolution results and prevent the asphaltene deposition process, which showed much better results over extended periods of time. Another important aspect for the field implementation is the relatively low flashpoint for these oil-based solvents, which makes them hazardous and dangerous. These health, safety, and environment challenges were overcome by the utilization of water-based solvents due to their relatively high flashpoint. This become a crucial benefit to have a containment plan to avoid any safety hazards during the summer season. In some cases, this entailed the use of heavy aromatic fluids, e.g., patha solvents, which have a relatively high flashpoint — up to 66 °C.

Job Execution

Field job planning and execution was commenced once the lab testing was concluded and the acquired results were satisfactory, both in terms of the ability of the solution to dissolve the asphaltene deposit while preventing the re-deposition process. The addition of well-balanced surfactants helped to disperse the organic deposits in the water phase, thereby enhancing the efficiency of the water-based solvents in de-flocculating the asphaltene particles in the dissolution fluids. Once dispersed, the asphaltene particles are exposed and the water-based solvents can begin to act in the dissolution process.

This process is normally assisted by the mechanical movement of the utilized clean out assembly, which serves two main purposes. The first function is to help break down some of the hard and consolidated asphaltene deposits so that the solvent fluids can begin the dissolution process. The second function is to provide a circulation method to remove all of these solids and fill accumulation all the way to the surface, which can then be collected for the required lab analysis. Jetting nozzles were utilized to create a turbulent flow regimen that can assist breaking the post-treatment completion. The clean out assembly is run to maximize the reach depth to confirm the wellbore accessibility and verify that no re-deposition action has taken place.

The initial job design included a detailed step by step procedure to perform the clean out operations, which can be classified into three main categories. The first stage is the "pre-flush" fluids in which the well has to be properly conditioned to receive the main treatment fluids. During this phase, surfactants and demulsified fluids are pumped into the wellbore to break down emulsion layers surrounding asphaltene particles while circulation is established to flush out any undesired solids or fill accumulations.

The second stage "main treatment" consisted of pumping the water phase and solvent mixtures at maximum injection rates to achieve high penetration into the formation. The final stage, the "post-flush," consisted of pumping filtered water to achieve a higher penetration into the formation, will increase the adherence of the solvent fluids to the formation rock surfaces and circulating all dissolute asphaltene and unwanted solids to the surface.

The solubility for the developed fluids was governed by three major factors, which are the type and quantity of organic solvent used, amount of water phase, and finally the added surfactants/co-solvents. A clay stabilizer is recommended for the purpose of preventing migration and/or swelling of clays following this treatment, which included the use of diverter additives to control the distribution of treatment fluids inside the uneven permeability across the open hole section.

A test package was also utilized to monitor the return fluids and analyze the collected samples, which consisted of a choke manifold, injection pump, and a patch mixer to facilitate neutralizing the return fluids prior to sending them to the production facility. The utilized treatment recipes consisted mainly of water-based fluids along with an effective solvent fluid. The combination of these two components created a strong detergent fluid that can break oil-water emulsion layers surrounding asphaltene particles, further enhancing the treatment process.

A vital aspect in the recipe development process was to determine the optimum ratio of the water phase to the

Table 1 *The asphaltene solubility in different mixtures of a water phase to solvent volume.*

#	Fluid	Water (%)	Solvent (%)
1	Solvent A	20	30
2	Solvent B	40	40
3	Solvent C	20	40
4	Solvent D	60	20

Fig. 3 *The asphaltene solubility in different water/solvent mixtures.*

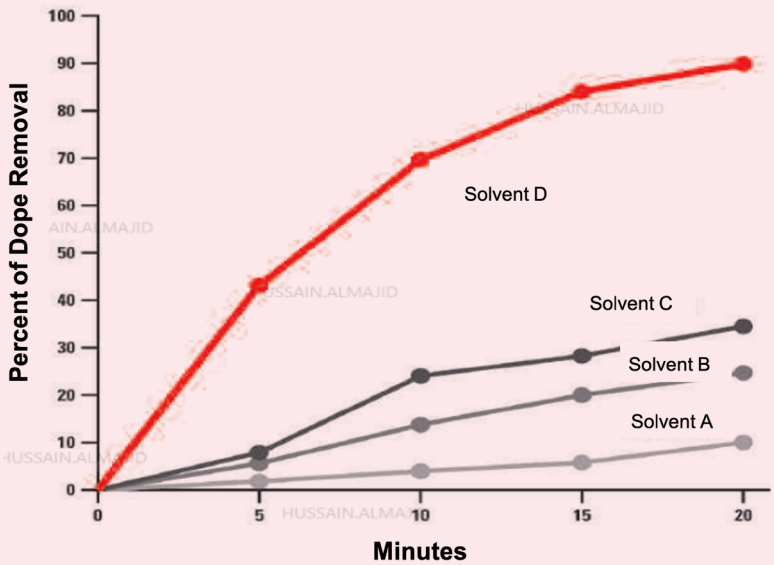

solvent volume to be used in this mixture. The higher volume of the water phase helped to not only reduce the overall cost for the solvent fluid but also increase the penetration depth into the formation.

Table 1 shows the asphaltene solubility in different mixtures of a water phase to solvent volume as depicted in Fig. 3.

Conclusions

This article discussed asphaltene clean out operations utilizing aromatic fluids that will help to prevent the re-deposition process, thereby minimizing the need for future well intervention operations.

The following summarizes the lessons learned resulting from the implemented field applications:

1. The asphaltene precipitation process is governed by the ratio of paraffin and aromatics in the crude oil. Changes in reservoir thermodynamic conditions may allow the paraffin to expand higher than aromatics, as the flocculation rate and asphaltene precipitation will increase.
2. The use of rapid analytical techniques, e.g., XRD mineralogical analysis, to determine the magnitude and potential of formation clay problems can help select the optimal treatment fluids.
3. Mechanical movement of the utilized clean out assembly can help to break down some of the hard and consolidated asphaltene deposits so that the solvent fluids can begin the dissolution process. Also, it can provide a circulation method to remove all of these solids and fill accumulation all the way to the surface, which can then be collected for the required lab analysis.
4. Using updated software with real-time field data, and considering the parameters involved in the sand/well vacuuming process, can help field engineers to design, optimize, and execute the vacuuming process efficiently.
5. A vital aspect in the recipe development process was determined by the optimum ratio of the water phase to the solvent volume to be used in this mixture. The higher volume of the water phase helped

to not only reduce the overall cost for the solvent fluid but also increase the penetration depth into the formation.

6. The solubility for the developed fluids was governed by three major factors, which are the type and quantity of organic solvent used, the amount of water phase, and finally the added surfactants/co-solvents.

7. A clay stabilizer is often recommended for the purpose of preventing migration and/or swelling of clays following an acid treatment in a sandstone formation. Common clay stabilizers, i.e., polyquaternary amines or polyamines, can be used at 0.1% to 0.4%. A clay stabilizer seems to be most effective when added to the overflush only based on the literature[3].

Acknowledgments

This article was presented at the International Petroleum Technology Conference, Riyadh, Kingdom of Saudi Arabia, February 21-23, 2022.

References

1. Soo, H. and Radke, C.J.: "Velocity Effects in Emulsion Flow through Porous Media," *Journal of Colloid and Interface Science*, Vol. 102, Issue 2, December 1984, pp. 462-476.

2. Al-Khaldi, M.H., Nasr-El-Din, H.A., Blauch, M.E. and Funkhouser, G.P.: "New Findings on Damage Potential, Geochemical Reaction Mechanisms, and Production Enhancement Applications for Citric Acid," *SPE Journal*, Vol. 10, No. 3, September 2005, pp. 267-275.

3. Al-Harbi, B.G., Al-Dahlan, M.N. and Al-Khaldi, M.H.: "Aluminum and Iron Precipitation during Sandstone Acidizing Using Organic-HF Acids," SPE paper 151781, presented at the SPE International Symposium and Exhibition on Formation Damage Control, Lafayette, Louisiana, February 15-17, 2012.

4. Crowe, C., Masmonteil, J., Touboul, E. and Thomas, R.: "Trends in Matrix Acidizing," *Oilfield Review*, October 1992, pp. 24-40.

5. Giles, C.H.: "Adsorption at Solid/Liquid Interfaces," in *Anionic Surfactants: Physical Chemistry of Surfactant Action*, (ed.) Lucassen-Reynders, E.H., 1981, 412 p.

6. Hall, A.C., Collin S.H. and Melrose, J.C.: "Stability of Aqueous Wetting Films in Athabasca Tar Sands," *Society of Petroleum Engineers Journal*, Vol. 23, Issue 2, April 1983, pp. 249-258.

About the Authors

Hussain A. Almajid

B.S. in Petroleum Engineering, Louisiana State University

Hussain A. Almajid is a Production Engineer working in Saudi Aramco's Southern Area Production Engineering Department. His work experience includes work in several oil fields, including in North Ghawar and in the Southern Area. During this time, Hussain developed his experience as a skilled Production Engineer dealing with intelligent field equipment, electric submersible pumps, and smart well completions.

He has written and presented several Society of Petroleum Engineers (SPE) papers and presentations. Hussain is a certified SPE engineer.

In 2010, he received his B.S. degree in Petroleum Engineering from Louisiana State University, Baton Rouge, LA.

Alaa S. Shawly

B.S. in Petroleum Engineering, King Fahd University of Petroleum and Minerals

Alaa S. Shawly is a Supervisor of Production Engineering in the Central Arabia Production Engineering Unit in Saudi Aramco's Southern Area Production Engineering Department.

Prior to joining Saudi Aramco in 2006, he worked as a summer trainee with the Ain Dar and Shedgum Unit of the Reservoir Management Department for 8 weeks from July through August 2004. Alaa has 14 years of experience, mainly in acid stimulation and well intervention.

In 2006, he received his B.S. degree in Petroleum Engineering from King Fahd University of Petroleum and Minerals (KFUPM), Dhahran, Saudi Arabia.

Abdullah AlQassem

B.S. in Petroleum Engineering, King Fahd University of Petroleum and Minerals

Abdullah AlQassem is a Halliburton Production Solutions (Coiled Tubing Services) Operations Manager.

He began his career in 2010, starring as an Associate Technical Professional for coiled tubing (CT). Since this time, Abdullah has held various technical, sales, and operational roles throughout Saudi Arabia.

Throughout his career, Abdullah has developed his experience as a technical CT engineer dealing with various fields throughout the Kingdom. Working with Saudi Aramco, he has brought forth the newest technologies to support the CT challenges.

In 2010, Abdullah received his B.S. degree in Petroleum Engineering from King Fahd University of Petroleum and Minerals (KFUPM), Dhahran, Saudi Arabia.

Mineral Dissolution and Cation Exchange in Low Salinity Waterflooding

Dr. Quan Chen, Dr. Moataz O. Abu-AlSaud, Dr. Subhash C. Ayirala and Dr. Ali A. Yousef

Abstract /

Low salinity waterflooding (LSWF) is an emerging improved/enhanced oil recovery (IOR/EOR) technique with an applicability to both sandstone and carbonate reservoirs. The underlying recovery mechanism of LSWF is still not completely understood due to the multiscale complex interactions occurring in crude oil/brine/rock systems. There are several proposed mechanisms, and mineral dissolution is the most prominent among them. The objective is to study the brine-rock interactions, and understand the propagation of mineral dissolution waves in LSWF processes through geochemical modeling.

A reactive transport geochemical model using the PHREEQC (pH-REdox-EQuilibrium in C programing language) simulator has been carried out to understand the interplay of different geochemical effects such as multivalent cation exchange, mineral dissolution during flow and transport in LSWF. The presence of clays and carbonate cements is most common in sandstone reservoirs, while some carbonate reservoirs also contain clay minerals. Therefore, a core-scale geochemical model containing clay and carbonate minerals as active minerals for brine-rock interactions is chosen as a representative analog for both sandstones and carbonates in this study.

The results showed that LSWF disturbs the geochemical equilibrium between formation brine and reservoir rock minerals to cause carbonate mineral dissolution. It was also inferred that without the cation exchange effect of clay minerals, carbonate mineral dissolution effects are local and they occur only close to the inlet of a core plug sample during LSWF. The new equilibrium between brine and rock mineral is then established rapidly. In the presence of clay minerals and cation exchange effect, the clay surfaces were found to preferentially adsorb divalent cations over monovalent cations during LSWF. Such cation exchange process softened the injected low salinity brine to maintain its under saturation with respect to reservoir minerals, and subsequently propagated carbonate mineral dissolution waves across the full length of the core sample.

The novelty of this work is that it proposes and demonstrates a new geochemical-based mechanism for LSWF, i.e., the propagation of mineral dissolution waves driven by the spreading of cation exchange process in the reservoir. The identified mechanism has several practical implications in the field: (1) carbonate mineral dissolution and the associated local pH increase can extend from local to reservoir scale, (2) the resulting mineral dissolution effectively releases the oil attached to the mineral surfaces, and (3) increasing the pH modifies the surface charges of both rock and crude oil more negatively charged. The subsequent electrostatic repulsion between the two interfaces would increase the water wetness of rock surfaces to achieve higher IOR in LSWF.

Introduction

Waterflooding has been the most widely used oil recovery technique in the industry worldwide during the past century. Historically, waterflooding has been considered a physical process for maintaining reservoir pressure and displacing oil from injection wells to production wells. Over the past few decades, very little attention has been paid to the study of the effect of injection water chemistry on the efficiency of oil recovery by the industry. Also, is has been well recognized that a decrease in injection brine salinity can increase oil recovery in waterflooding.

Low salinity waterflooding (LSWF) is an emerging improved/enhanced oil recovery (IOR/EOR) technology with enormous potential for both sandstone and carbonate reservoirs. This technology has received wide spread attention because of its simplicity and cost-effectiveness when compared to other conventional EOR techniques. LSWF also offers other extra benefits such as avoiding scale issues and reducing reservoir souring problems[1, 2]. Many laboratory experiments and field trials of LSWF[3, 4] have been conducted to evaluate the EOR benefit and understand the underlying recovery mechanisms.

Various EOR mechanisms for LSWF have been proposed as follows: clay swelling and resulting in differential

pressure rise[5]; fines release and migration[6, 7]; elevated pH associated mechanisms similar to alkaline flooding[8]; multicomponent ion exchange[9]; double layer expansion[10]; wettability modification[11, 12]; mineral dissolution[13, 14]; and reduction in adhesion forces[15, 16]. The mineral dissolution mechanism was discounted by some studies with the reasoning that mineral dissolution waves cannot spread in the reservoir[17, 18].

The objective of this article is to study the brine-rock interactions, and understand the propagation of mineral dissolution waves in LSWF processes through geochemical modeling. The geochemical software program PHREEQC (pH-REdox-EQuilibrium in C programing language) developed by the U.S. Geological Survey (USGS), has been employed to achieve this objective. PHREEQC is capable of simulating various geochemical reactions, including: calculations of speciation and saturation state, batch reactions, kinetically controlled reactions, transport calculations coupled with various geochemical reactions, and inverse modeling[19].

An advective dispersive transport geochemical model coupled with the equilibria of aqueous species, cation exchange, and carbonate minerals has been established with PHREEQC to investigate the brine-rock interactions during the LSWF process.

Description of Geochemical Model

Clay minerals are present in most sandstone and some carbonate reservoirs. Carbonate minerals are normally the most abundant cements in sandstone reservoirs[20], and therefore a core-scale geochemical rock model, including clay and carbonate minerals as active minerals for brine-rock interactions, can become a good representative of sandstone and some carbonate reservoirs.

The geochemical model was built by coupling the transport process with three main reactions: (1) aqueous reaction, (2) cation exchange, and (3) carbonate mineral dissolution and precipitation. The PHREEQC database, which applies Davies and extended Debye-Hückel equations for the activity coefficient models[19], was employed for the geochemical simulations.

Advection-Reaction-Dispersion Equation

The advection-reaction-dispersion equation is used in the PHREEQC simulator to model the geochemical process involving 1D solute transport of a reactant through a porous medium:

$$\frac{\partial C}{\partial t} = -v\frac{\partial C}{\partial x} - \sum_i \left(\frac{\partial q}{\partial t}\right)_i + D_L\frac{\partial^2 C}{\partial x^2} \quad (1)$$

where C is the ion concentration in water (mol/kgw), t is time (s), v is velocity of water transport or flow through the porous media (m/s), x is distance (m), q is the reacting ion concentration near the solid surface, i represents various geochemical reactions, and D_L is the longitudinal dispersion coefficient in the direction of flow.

There are three terms on the right-hand side of Eqn. 1. The first term describes the advective transport process where the flow of solute along with water is driven by the pressure gradient. The second term represents the reactant concentration change with time due to various geochemical reactions, such as cation exchange, mineral dissolution, and precipitation. The last term represents the dispersive transport process where the solute mixing occurs due to local variation of flow velocity and Brownian motion of molecules in the porous medium.

For waterflooding in reservoirs with Peclet numbers higher than 1, the combined effects of dispersion and molecular diffusion in the parameter of longitudinal dispersion coefficient is given by Eqn. 2:

$$D_L = D_e + a_L v \quad (2)$$

where De is the effective diffusion coefficient of fluid in the porous medium, and α_L is the dispersivity (m)[21].

Cation Exchange

The competition for the exchange sites between the sorbed cations and exchangeable cations in a solution depends on the affinity of each cation for the exchange sites and the ion composition on the exchange sites and in the solution.

In the PHREEQC database[19], following the Gaines-Thomas convention[22], various cation exchange half-reactions are defined under the keyword EXCHANGE_SPECIES. In the model considered for this study, the given cation exchange half-reactions and corresponding mass action equations are included to calculate the equilibrium composition on the exchange sites and in the solution:

$$Na^+ + X^- = NaX \quad (3)$$

$$K_{Na} = \frac{[NaX]}{[Na^+][X^-]} \quad (4)$$

$$K^+ + X^- = KX \quad (5)$$

$$K_K = \frac{[KX]}{[K^+][X^-]} \quad (6)$$

$$Mg^{2+} + 2X^- = MgX_2 \quad (7)$$

$$K_{Mg} = \frac{[MgX_2]}{[Mg^{2+}][X^-]^2} \quad (8)$$

$$Ca^{2+} + 2X^- = CaX_2 \quad (9)$$

$$K_{Ca} = \frac{[CaX_2]}{[Ca^{2+}][X^-]^2} \quad (10)$$

where X^- donates the exchange site with a charge of -1, square brackets in the equations represent activities. The cation exchange coefficients applied for this model are listed in Table 1.

Table 1 *The summary of cation exchange coefficients used in the model.*

$LogK_{Na}$	$LogK_K$	$LogK_{Mg}$	$LogK_{Ca}$
0	0.7	0.6	0.77

The full ion exchange reactions can be generated by combing the half-reaction of Eqn. 3 with the half-reactions of Eqns. 5, 7, and 9, respectively:

$$Na^+ + KX \leftrightarrow NaX + K^+ \quad (11)$$

$$Na^+ + \tfrac{1}{2} MgX_2 \leftrightarrow NaX + \tfrac{1}{2} Mg^{2+} \quad (12)$$

$$Na^+ + \tfrac{1}{2} CaX_2 \leftrightarrow NaX + \tfrac{1}{2} Ca^{2+} \quad (13)$$

Applying the law of mass action for the cation exchange reactions of Eqns. 11, 12, and 13 yields:

$$K_{Na\backslash K} = \frac{[NaX][K^+]}{[KX][Na^+]} \quad (14)$$

$$K_{Na\backslash Mg} = \frac{[NaX][Mg^{2+}]^{0.5}}{[MgX_2]^{0.5}[Na^+]} \quad (15)$$

$$K_{Na\backslash Ca} = \frac{[NaX][Ca^{2+}]^{0.5}}{[CaX_2]^{0.5}[Na^+]} \quad (16)$$

For low salinity water injection using diluted high salinity water with a dilution factor of n, applying the law of mass action to a heterovalent cation exchange reaction such as Ca-Na in the n-times diluted brine gives:

$$K_{Na\backslash Ca} = \frac{[NaX]\left[\frac{Ca^{2+}}{n}\right]^{0.5}}{[CaX_2]^{0.5}[\frac{Na^+}{n}]} \quad (17)$$

$$\frac{[CaX_2]^{0.5}}{[NaX]} = \frac{n^{0.5}[Ca^{2+}]^{0.5}}{K_{Na/Ca}[Na^+]} \quad (18)$$

$$\frac{[CaX_2]}{[NaX]^2} = \frac{n[Ca^{2+}]}{K^2_{Na/Ca}[Na^+]^2} \quad (19)$$

For the dilution factor of n, Eqn. 18 shows that the ratio of $[CaX_2]^{0.5}$ to $[NaX]$ increases by a factor of $n^{0.5}$, and Eqn. 19 shows that the ratio of $[CaX_2]$ to $[NaX]^2$ increases by a factor of n. For heterovalent exchange reactions, the salinity level has an extra effect. The multivalent cations are even more preferentially adsorbed over the univalent cations by the exchanger with a decrease in salinity level.

Solubility of Carbonate Minerals

In the geochemical model of this study, the calcite ($CaCO_3$) mineral equilibrium in a solution is considered. The dissolution of the $CaCO_3$ is expressed as:

$$CaCO_3 \leftrightarrow Ca^{2+} + CO_3^{2-} \quad (20)$$

The saturation state of the solution with respect to the $CaCO_3$ can be determined by comparing the ion activity product, IAP, with the solubility product, K, for the $CaCO_3$:

$$IAP_{calcite} = [Ca^{2+}][CO_3^{2-}] \quad (21)$$

where the square brackets denote activities in the solution,

$$K_{calcite} = [Ca^{2+}][CO_3^{2-}] \quad (22)$$

where the square brackets denote activities at equilibrium condition.

The saturation index, SI, is defined as the ratio of IAP to K:

$$SI = \frac{IAP}{K} \quad (23)$$

For $SI = 1$, it means that the solution is at equilibrium with the mineral. $SI < 1$ indicates that the solution is at subsaturation with respect to the mineral and the mineral could dissolve. $SI > 1$ represents that the solution is at supersaturation with respect to the mineral and the mineral could precipitate.

As demonstrated by Yutkin et al. (2018)[18], the timescale of $CaCO_3$ equilibration with a flowing aqueous phase is significantly less than the fluid residence time within the rock formation, which means the dissolution/precipitation process occurs almost instantaneously on the rock surface. Therefore, the local thermodynamic equilibrium between $CaCO_3$ and the injecting brine is justified during LSWF processes and applied in the simulations of this study.

Model Parameters

In the geochemical model of PHREEQC, the rock core sample contains the reactive minerals of clay and $CaCO_3$. The rock core sample is initially saturated with high salinity formation water. The chemical composition of the formation brine is shown in Table 2. The formation water within the pore space of the rock core sample is in thermodynamic equilibrium with clay and $CaCO_3$. This thermodynamic equilibrium process involves cation exchange on clay surfaces and dissolution and precipitation of $CaCO_3$.

The 1D reactive transport geochemical model built with PHREEQC has 20 cells. For each of the 20 cells, one aqueous SOLUTION data block, one cation EXCHANGE data block, and one EQUILIBRIUM_PHASES data block is defined to calculate the thermodynamic interactions among aqueous solutions, cation exchangers (clay) and minerals ($CaCO_3$). In the model, all 20 cells have the same initial equilibrium

Table 2 *The compositions of the formation brine and injection brine.*

Ions	Na^+	K^+	Ca^{2+}	Mg^{2+}	Cl^-
Formation brine (ppm)	10,822	90	402	49	17,624
Injection brine (ppm)	373	3.1	14	1.7	607.7

Table 3 The key parameters of the geochemical model.

Length of Core Sample (m)	Number of Grid Blocks	Flow Rate (m/day)	Dispersivity (m)	Qv (meq/L PV)
0.076	20 × 1 × 1	0.456	0.02	9

conditions with respect to the aqueous solution (formation water), cation exchange, and carbonate mineral ($CaCO_3$). The TRANSPORT data block includes number of cells, a cell length, a timestep for solution flow through one cell, the number of pore volumes (PVs) of displacing fluid flow through the cells, and dispersivity. Some of the key model parameters are shown in Table 3.

The detailed model parameter values are: the cell length is 0.0038 m, the time step is 720 s, which corresponds to a flow rate of 0.456 m/day of LSWF at a constant temperature of 25 °C. Note that the injection brine is a 29 times diluted version of the formation brine. The low flow rate in comparison with a relatively high dissolution rate of $CaCO_3$ is justified for a local thermodynamic equilibrium condition of $CaCO_3$ dissolution during low salinity brine injection. The cation exchange capacity is 9 meq/L PVs and dispersivity is 0.02 m are used in the model. A total of 65 PVs of low salinity brine is injected.

Results and Discussion

Geochemical Simulation of Coreflood Experiment

The developed PHREEQC geochemical model is first validated to match the data from published coreflood experiment[9]. The geochemical modeling results of effluent Mg^{2+} and Ca^{2+} concentration changes with the injected PV of the low salinity brine are shown in Fig. 1. These simulated results match very well with the trend of effluent concentration changes in the divalent cations reported from the low salinity brine injection coreflood experiment.

The two key features observed during the displacement process of high salinity formation brine by the low salinity brine are: (1) The effluent concentrations of divalent cations drop to a much lower level than the divalent cation concentrations in the injected low salinity brine, and (2) the softening period, where the concentration of each ion drops below the low salinity brine ion concentrations, lasting for several PVs.

It is interesting to note that such a softening period has also been observed during LSWF in the field for Mg^{2+} ions. The Mg^{2+} concentration in the produced brine has dropped below the low salinity brine Mg^{2+} concentration for about 0.3 PV, due to the strong interaction of this divalent ion with the reservoir rock[23].

Salinity Effects on Cation Exchange

The mathematic relationship of heterovalent cation exchange between a divalent cation and a monovalent cation in diluted brine with a dilution factor of n is shown in Eqn. 19, where the ratio of $[CaX_2]$ to $[NaX]^2$ increases by a factor of n.

Fig. 1 The geochemical modeling results of effluent Mg^{2+} and Ca^{2+} concentration changes with injected PVs for LSWF.

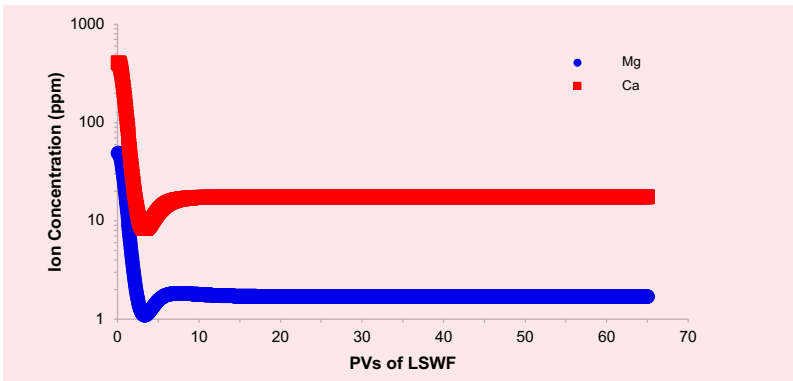

This relationship is also demonstrated by the geochemical modeling results shown in Fig. 2. The results presented in Fig. 2 indicate that the dilution of the high salinity formation water leads to more preferential sorption of divalent cations Ca^{2+} and Mg^{2+} over monovalent cations Na^+ and K^+.

Such preferential sorption of divalent cations over monovalent cations resulting from cation exchange during low salinity brine injection would lead to the development of a "self-softening" zone. In addition, dispersion mixes the injected low salinity brine with the in situ high salinity formation brine. The injected low salinity brine also perturbs the thermodynamic equilibrium between high salinity formation brine and soluble carbonate minerals such as $CaCO_3$, and leads to the dissolution of $CaCO_3$ and increase in pH.

This explanation is supported by the results of the pH evolution during low salinity brine injection, Fig. 3. It is also interesting to note that the observed trend of effluent pH changes goes in the opposite direction of effluent the Ca^{2+} concentration changes shown in Fig. 1.

Propagation of Mineral Dissolution Waves

To provide a better understanding of complex interplay of various geochemical processes, the reactive transport modeling performed in this study is focused on the interactions of cation exchange and $CaCO_3$ equilibrium with the effect of numerical dispersion only. Figures 4 and 5 present the quantities of dissolved $CaCO_3$ along the length of the core sample after 1 PV, 2 PV, 3 PV,

Fig. 2 *The equivalent fractions of exchangeable cations on the exchanger in mixtures of high salinity water and deionized water.*

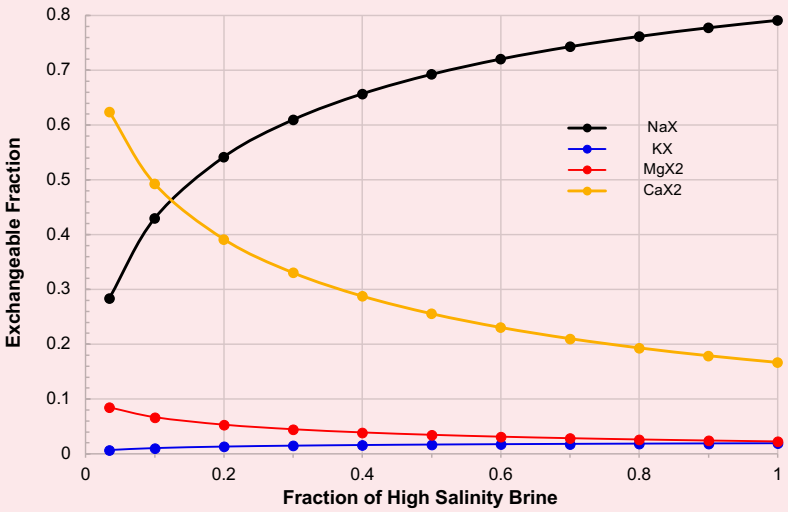

Fig. 3 *The geochemical modeling results of pH evolution in the effluent brine during LSWF.*

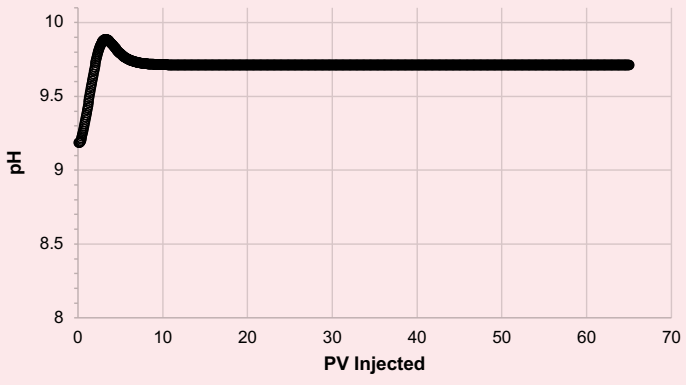

and 4 PV low salinity brine injection for the two cases without and with cation exchange effect, respectively.

Figure 4 shows that without cation exchange effect, the $CaCO_3$ dissolution occurs only in the first grid block near the inlet of the core sample during low salinity brine injection. The reason is that the new thermodynamic equilibrium has been reached between the injected low salinity brine and $CaCO_3$ in the first grid block at the local thermodynamic equilibrium condition, and therefore, the $CaCO_3$ dissolution wave cannot spread. Similar results were reported by other studies, and consequently, the carbonate dissolution mechanism of LSWF was ignored[17, 18].

With the cation exchange effect, the $CaCO_3$ dissolution occurs over the full length of the core sample during low salinity brine injection, Fig. 5. This is because clay minerals act as uniformly distributed water softeners,

Fig. 4 *The dissolved $CaCO_3$ along the length of the core sample after 1 PV, 2 PV, 3 PV, and 4 PV LSWF without cation exchange effect.*

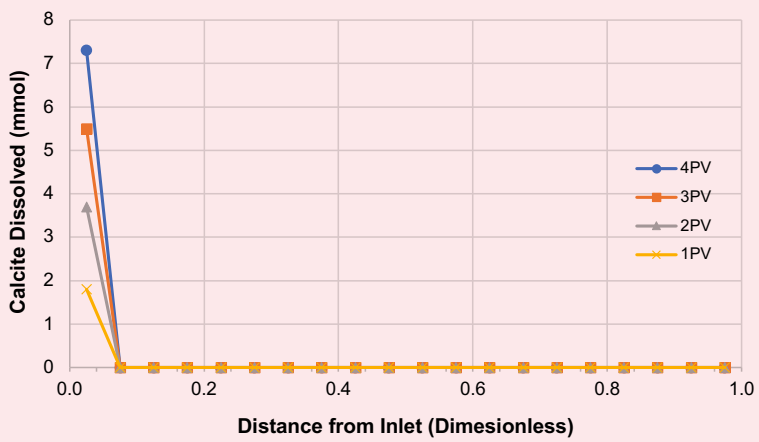

which adsorb divalent cations more preferentially over monovalent cations during low salinity brine injection. As a result, a very small cation exchange capacity of 9 meq/L PV is sufficient to drive the $CaCO_3$ dissolution waves to spread over the entire rock sample for 4 PV LSWF. The spreading of the $CaCO_3$ mineral dissolution waves driven by cation exchange during LSWF processes can be described by the following geochemical reactions:

$$H_2O + CaCO_3 + 2NaX \leftrightarrow CaX_2 + 2Na^+ + HCO_3^- + OH^- \quad (24)$$

$$H_2O + CaCO_3 + 2KX \leftrightarrow CaX_2 + 2K^+ + HCO_3^- + OH^- \quad (25)$$

$$H_2O + CaCO_3 + MgX_2 \leftrightarrow CaX_2 + Mg^{2+} + HCO_3^- + OH^- \quad (26)$$

The Ca^{2+} ions have higher affinity for an exchanger than the other cations, Na^+, K^+, and Mg^{2+}, and therefore displaces other cations from the exchanger during LSWF. As a consequence, the geochemical reactions of Eqns. 24, 25, and 26 are driven to the right-hand side, which leads to $CaCO_3$ dissolution and an increase in pH, bicarbonate concentration, and therefore, alkalinity in the solution. This explains why the data trend of effluent pH changes goes in an opposite direction of the effluent Ca^{2+} concentration changes as previously shown in the Figs. 1 and 3. The alkalinity for modeled geochemical reactions is defined by Eqn. 27:

$$[Alkalinity] = [HCO_3^-] + 2[CO_3^{2-}] + [OH^-] - [H^+] \quad (27)$$

where square brackets denote concentrations in mol/kgw. This alkalinity is also called an acid neutralizing capacity.

Fig. 5 *The dissolved $CaCO_3$ along the length of the core sample after 1 PV, 2 PV, 3 PV, and 4 PV LSWF with cation exchange effect.*

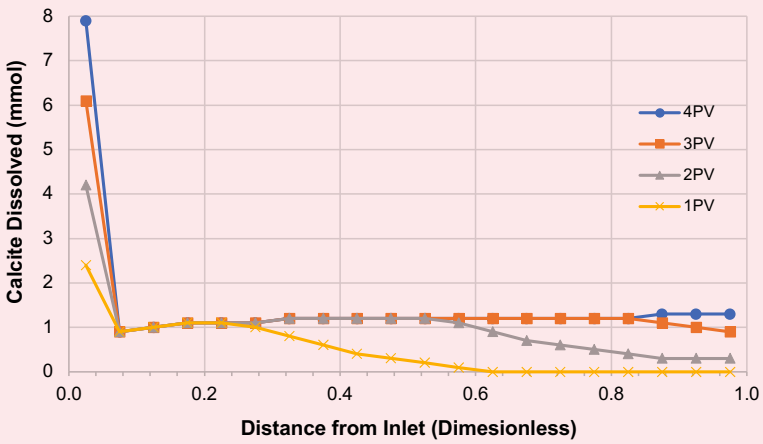

Fig. 6 *The equivalent fraction of NaX and CaX_2 along the length of the core sample after 1 PV, 2 PV, 3 PV, and 4 PV of LSWF.*

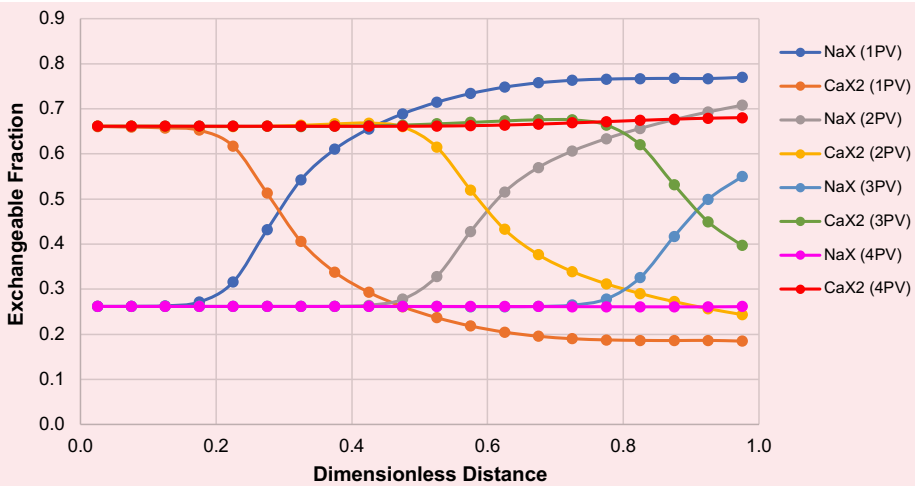

Fig. 7 *The equivalent fraction of CaX_2 along the length of the core sample after 1 PV, 2 PV, 3 PV, and 4 PV of LSWF.*

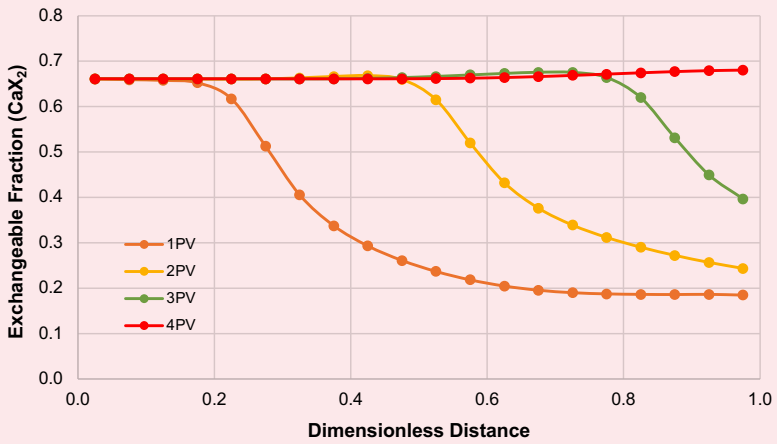

Fig. 8 *The effluent divalent ion concentrations (Ca^{2+}, Mg^{2+}), pH, and alkalinity vs. PV of LSWF for the case with $CaCO_3$ dissolution.*

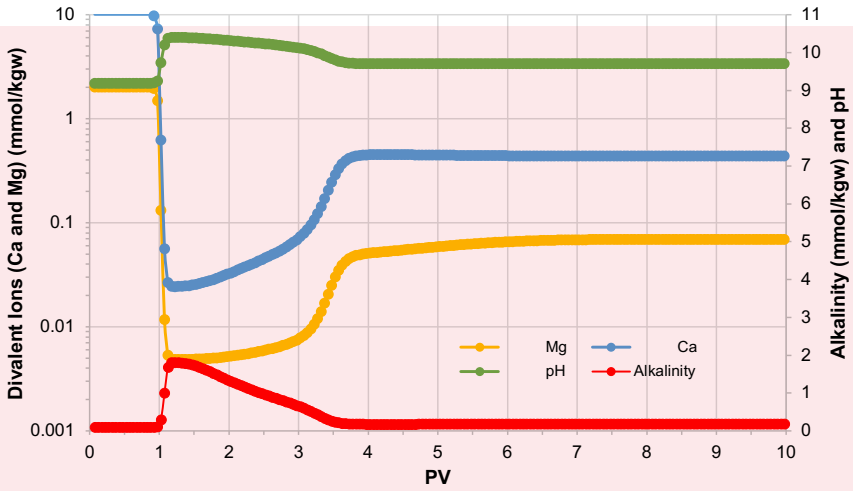

Fig. 9 *The effluent monovalent ion concentrations (Na^+, Cl^-, and K^+) vs. PV of LSWF for the case with $CaCO_3$ dissolution.*

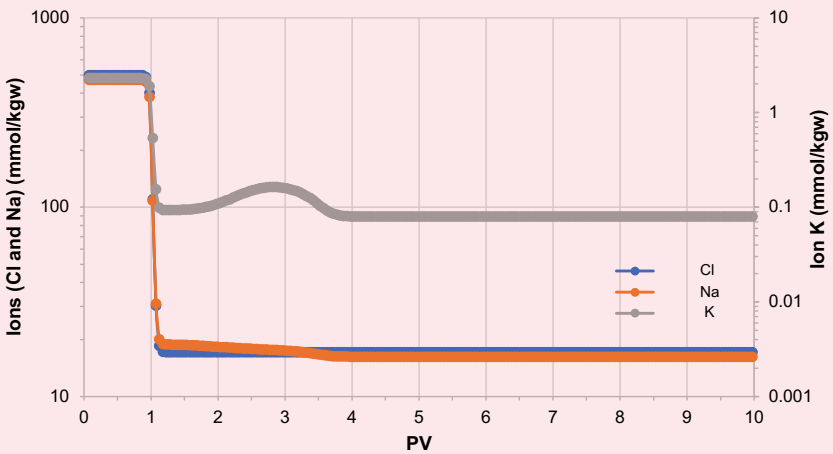

Spreading of Cation Exchange Waves

Figure 6 shows the in situ ion chromatography simulation results describing the fraction of NaX and CaX_2 along the length of the core sample at 1 PV, 2 PV, 3 PV, and 4 PV of LSWF injection. As can be seen, the data trends of the NaX and CaX_2 equivalent fractions form almost a mirror image of each other. Such results are mainly due to cation exchange and $CaCO_3$ dissolution reactions, Eqns. 24 to 26, during the LSWF process.

The spreading of cation exchange, CaX_2, waves at different injected PV of LSWF have similar shapes, Fig. 7. This identical behavior obtained at different PVs can be attributed to the propagation of the $CaCO_3$ dissolution waves as previously shown in Fig. 5. These findings confirm that propagation of the $CaCO_3$ dissolution waves are driven by the spreading of the CaX_2 during LSWF.

Change of pH and Alkalinity

The geochemical reactions of Eqns. 24 to 26 are also demonstrated by the modeling results, Figs. 8 and 9. From Fig. 8, it is quite evident that the decrease of Ca^{2+} concentration is accompanied by the increases of pH and alkalinity in effluents during the LSWF process. Such an increase in effluent pH has also been frequently observed in coreflood experiments during the LSWF processes[8, 24]. Figure 8 also shows that the trends of Ca^{2+} concentration and alkalinity closely follow each other. These trends can be attributed to the geochemical reactions of Eqns. 24 to 26, wherein the adsorption of Ca^{2+} by the exchanger (X) drives the $CaCO_3$ dissolution, and subsequently, results in the increase of alkalinity.

Interestingly, the increase of iron concentration and excess alkalinity in produced water were also reported during the LSWF interwell scale field trial in the Endicott field of Alaska[25]. This change in produced water chemistry is likely caused by the dissolution of the carbonate mineral siderite, driven by the cation exchange during the LSWF, because siderite is the most common cement in the Endicott field, together with a considerable amount of clay minerals (12%) in the pilot area[25, 26].

Figure 9 shows the increase in concentration of monovalent cations such as Na^+ and K^+ with respect to the injected water concentration, which is captured by the geochemical reactions of Eqns. 24 and 25 in the model. Figure 10 presents the geochemical modeling results of the effluent ion concentration for the case without $CaCO_3$ equilibrium.

The comparison of Figs. 8 and 9 with Fig. 10 reveals three major differences: (1) The pH values are constant at 7 for the case without $CaCO_3$ dissolution, but the pH value reaches up to 10.4 for the case with $CaCO_3$ dissolution; (2) the divalent cation concentrations (Ca^{2+} and Mg^{2+}) reached in the initial dilution plateau for the case without $CaCO_3$ dissolution are lower than the lowest divalent cation concentrations (Ca^{2+} and Mg^{2+}) reached for the case with $CaCO_3$ dissolution; and (3) the completion of geochemical reactions is much more rapid for the case with $CaCO_3$ dissolution.

The reasons for these major differences observed between the two cases with and without $CaCO_3$ dissolution are as follows. The $CaCO_3$ dissolution not only causes the increase of pH but also provides the additional source of Ca^{2+}. The increase in Ca^{2+} in the solution displaces other cations from the cation exchanger more rapidly, thereby accelerating the process described by the geochemical reactions of Eqns. 24 to 26.

Fig. 10 *The effluent ion concentrations (Na^+, Cl^-, Ca^{2+}, Mg^{2+}, and K^+) and pH vs. PV of LSWF for the case without $CaCO_3$ dissolution.*

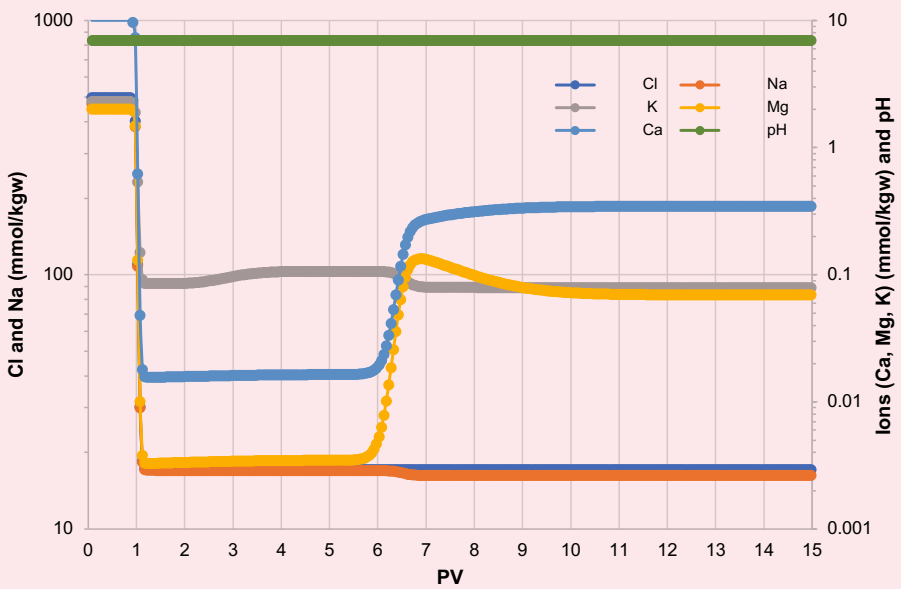

To further demonstrate the effects resulting from the geochemical reactions of Eqns. 24 to 26, pH values along the length of the core sample at 0 PV, 1 PV, and 2 PV of the LSWF are plotted in Fig. 11. Reservoirs often have higher pH buffering capacities with a source of hydrogen ions to consume the hydroxide ions produced by these three geochemical reactions. As a result, a significant pH change may not be observed in the produced water during LSWF. The higher pH buffering capacities in reservoirs will provide a stronger drive for the forward reactions of Eqns. 24 to 26, and therefore could enhance the $CaCO_3$ dissolution to cause a localized pH increase near the $CaCO_3$ surfaces of reservoir rocks.

Change of Crude Oil and Rock Mineral Surface Charges

The polar components of crude oils can have more negative charges at the oil/water interface with an increase of pH in the reservoirs as a result of the dissociation of carboxylic acids of crude oils:

$$RCOOH \leftrightarrow RCOO^- + H^+ \quad (28)$$

The effects of carboxylic acid dissociation reaction in crude oils have been observed during zeta potential measurements as a function of pH for crude oil emulsion[27]. These studies reported more negative zeta potentials at crude oil/water interface with an increase of pH. In addition, the pH effects on the surface charge are more pronounced at low salinity conditions due to the decrease in the electrostatic shielding ability of electrolytes. As a result, a relatively small increase in pH can result in a much more significant increase in the magnitude of crude oil negative zeta potentials.

The rock mineral surface sites act as amphoteric species at water/mineral interface. The surface sites can be protonated or deprotonated and obtain variable charges as a function of pH in the solution. These mineral surfaces can become more negatively charged or less positively charged with the increase in pH due to the following deprotonation reactions at the surface sites, $\equiv S$, of the minerals:

$$\equiv SOH_2^+ \leftrightarrow \equiv SOH + H^+ \quad (29)$$

$$\equiv SOH \leftrightarrow \equiv SO^- + H^+ \quad (30)$$

The results from the deprotonation reaction of Eqn. 30 were observed during zeta potential measurements as a function of pH for Clashach rock particles[28]. More negative zeta potentials are measured at the mineral surface with an increase of pH in this study. A similar trend of zeta potential as a function of pH was also reported for carbonate rock particles[29].

The overall effect of a pH increase during LSWF can lead to a large increase in the magnitude of negative surface potentials at both oil/water interface and water/rock interface, which can cause a significant increase in electrostatic repulsion. Such an increase in electrostatic repulsion at the two interfaces tends to stabilize the water film on the rock surface to increase water wetness, and subsequently improves the oil recovery.

Conclusions

This study proposes and demonstrates a new geochemical reaction mechanism during LSWF, i.e., the propagation of carbonate mineral dissolution waves driven by the spreading of cation exchange in reservoir porous rocks. The major conclusions drawn from this geochemical modeling investigation are as follows:

LSWF leads to subsaturation of carbonate minerals and therefore carbonate dissolution. Without the cation exchange effect of clay minerals, the carbonate minerals can only be dissolved near the inlet of the core sample. In the presence of clay minerals and cation exchange effect, the divalent cations have a much stronger affinity to the exchange sites of clay minerals than the univalent cations in a low salinity environment.

The clay minerals act as uniformly distributed water softeners, which soften the injected low salinity brine from inlet to outlet of the core sample in the LSWF processes. The geochemical reactions responsible for propagation of mineral dissolution waves driven by the spreading of cation exchange process are also discussed.

The spreading of mineral dissolution waves and the resulting local pH increase identified can have several reservoir-scale implications during LSWF:

- The dissolution wave of carbonate minerals and the resulting local pH rise can spread fieldwide.
- The dissolution of carbonate minerals releases oil attached to the mineral surfaces, and subsequently enables better oil mobilization.
- The increase in local pH can increase the magnitude of negative surface potentials at both crude oil/water and water/rock interfaces due to the deprotonation reactions at surface sites. The resulting electrostatic repulsive forces between the two interfaces stabilize the water film to increase the water wetness of the rock surface for higher IOR.

Fig. 11 The variations of pH along the length of the core sample during LSWF.

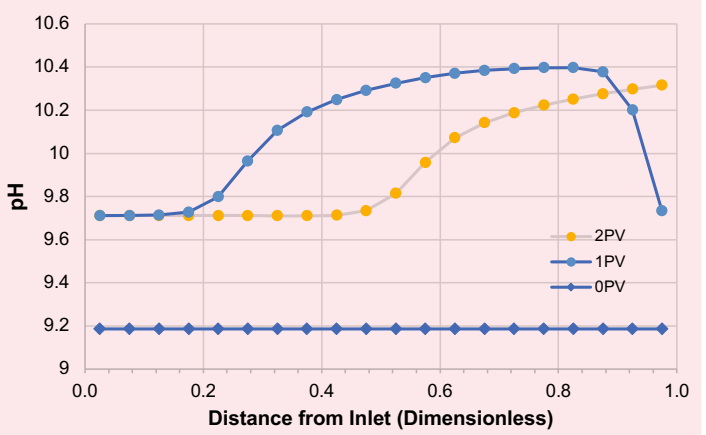

References

1. Collins, I.R.: "Holistic Benefits of Low Salinity Waterflooding," paper presented at the 16th European Symposium on Improved Oil Recovery, Cambridge, U.K., April 12-14, 2011.
2. Sorop, T.G., Suijkerbuijk, B.M.J.M., Masalmeh, S.K., Looijer, M.T., et al.: "Accelerated Deployment of Low Salinity Waterflooding in Shell," paper presented at the 17th European Symposium on Improved Oil Recovery, St. Petersburg, Russia, April 16-18, 2013.
3. Webb, K.J., Black, C.J.J. and Al-Ajeel, H.: "Low Salinity Oil Recovery — Log-Inject-Log," SPE paper 89379, presented at the SPE/DOE 14th Symposium on Improved Oil Recovery, Tulsa, Oklahoma, April 17-21, 2004.
4. Yousef, A.A., Liu, J.S., Blanchard, G.W., Al-Saleh, S., et al.: "Smart Waterflooding: Industry's First Field Test in Carbonate Reservoirs," SPE paper 159526, presented at the SPE Annual Technical Conference and Exhibition, San Antonio, Texas, October 8-10, 2012.
5. Bernard, G.G.: "Effect of Floodwater Salinity on Recovery of Oil from Cores Containing Clays," SPE paper 1725, presented at the Annual California Regional Meeting, Los Angeles, California, October 26-27, 1967.
6. Tang, G-Q. and Morrow, N.R.: "Influence of Brine Composition and Fines Migration on Crude Oil Brine Rock Interactions and Oil Recovery," *Journal of Petroleum Science and Engineering*, Vol. 24, Issues 2-4, December 1999, pp. 99-111.
7. Lebedeva, E., Senden, T.J., Knackstedt, M. and Morrow, N.R.: "Improved Oil Recovery from Tensleep Sandstone — Studies of Brine-Rock Interactions by Micro-CT and AFM," paper presented at the European Symposium on Improved Oil Recovery, Paris, France, April 27-29, 2009.
8. McGuire, P.L., Chatham, J.R., Paskvan, F.K., Sommer, D.M., et al.: "Low Salinity Oil Recovery: An Exciting New EOR Opportunity for Alaska's North Slope," SPE paper 93903, presented at the SPE Western Regional Meeting, Irvine, California, March 30-April 1, 2005.
9. Lager, A., Webb, K.J., Black, C.J.J., Singleton, M., et al.: "Low Salinity Oil Recovery — An Experimental Investigation," paper presented at the International Symposium of the Society of Core Analysts, Trondheim, Norway, September 12-16, 2006.
10. Ligthelm, D.J., Gronsveld, J., Hofman, J.P., Brussee, N.J., et al.: "Novel Waterflooding Strategy by Manipulation of Injection Brine Composition," SPE paper 119835, presented at the EUROPEC/EAGE Conference and Exhibition, Amsterdam, the Netherlands, June 8-11, 2009.
11. Chen, Q., Mercer, D. and Webb, K.J.: "NMR Study of Pore Occupancy and Wettability Modification during Low Salinity Waterflooding," SCA paper 2010-27, presented at the International Symposium of the Society of Core Analysts, Halifax, Nova Scotia, Canada, October 4-7, 2010.
12. Yousef, A.A., Al-Saleh, S.H., Al-Kaabi, A. and Al-Jawfi, M.S.: "Laboratory Investigation of the Impact of Injection-Water Salinity and Ionic Content on Oil Recovery from Carbonate Reservoirs," *SPE Reservoir Evaluation and Engineering*, Vol. 14, Issue 5, October 2011, pp. 578-593.
13. Hiorth, A., Cathles, L.M. and Madland, M.V.: "The Impact of Pore Water Chemistry on Carbonate Surface Charge and Oil Wettability," *Transport in Porous Media*, Vol. 85, 2010, pp. 1-21.
14. Pu, H., Xie, X., Yin, P. and Morrow, N.R.: "Low Salinity Waterflooding and Mineral Dissolution," SPE paper 134042, presented at the SPE Annual Technical Conference and Exhibition, Florence, Italy, September 19-22, 2010.
15. Hassenkam, T., Pedersen, C.S., Dalby, K., Austad, T., et al.: "Pore Scale Observation of Low Salinity Effects on Outcrop and Oil Reservoir Sandstone," *Colloids and Surfaces A: Physicochemical and Engineering Aspects*, Vol. 390, Issues 1-3, October 2011, pp. 179-188.
16. Ayirala, S.C., Saleh, S.H., Enezi, S. and Yousef, A.A.: "Multiscale Aqueous-Ion Interactions at Interfaces for Enhanced Understanding of Controlled Ionic Composition Waterflooding Processes in Carbonates," *SPE Reservoir Evaluation & Engineering*, Vol. 23, Issue 3, August 2020, pp. 1118-1132.
17. Nasralla, R.A., Snippe, J.R. and Farajzadeh, R.: "Coupled Geochemical Reservoir Model to Understand the Interaction between Low Salinity Brines and Carbonate Rock," SPE paper 174661, presented at the SPE Asia Pacific Enhanced Oil Recovery Conference, Kuala Lumpur, Malaysia, August 11-13, 2015.
18. Yutkin, M.P., Mishra, H., Patzek, T.W., Lee, J., et al.: "Bulk and Surface Aqueous Speciation of Calcite: Implications for Low Salinity Waterflooding of Carbonate Reservoirs," *SPE Journal*, Vol. 23, Issue 1, February 2018, pp. 84-101.
19. Parkhurst, D.L. and Appelo, C.A.J.: *Description of Input and Examples for PHREEQC Version 3 — A Computer Program for Speciation, Batch-Reactions, One-Dimensional Transport, and Inverse Geochemical Calculations*, U.S. Geological Survey Techniques and Methods, Book 6, Chapter A43, 2013, 497 p.
20. Pettijohn, F.J., Potter, P.E. and Siever, R.: *Sand and Sandstone*, 2nd edition, Springer: New York, 1987, 553 p.
21. Appelo, C.A.J. and Postma, D.: *Geochemistry Groundwater and Pollution*, 2nd edition, CRC Press, 2005, 683 p.
22. Gaines Jr., G.L. and Thomas, H.C.: "Adsorption Studies on Clay Minerals. II. A Formulation of the Thermodynamics of Exchange Adsorption," *Journal of Chemical Physics*, Vol. 21, Issue 4, 1953, pp. 714-718.
23. Lager, A., Webb, K.J., Collins, I.R. and Richmond, D.M.: "LoSal™ Enhanced Oil Recovery: Evidence of Enhanced Oil Recovery at the Reservoir Scale," SPE paper 113976, presented at the SPE/DOE Improved Oil Recovery Symposium, Tulsa, Oklahoma, April 19-23, 2008.
24. RezaeiDoust, A., Puntervold, T. and Austad, T.: "Chemical Verification of the EOR Mechanism by Using Low Saline/Smart Water in Sandstone," *Energy and Fuels*, Vol. 25, Issue 5, March 2011, pp. 2151-2162.
25. Seccombe, J.C., Lager, A., Jerauld, G., Jhaveri, B., et al.: "Demonstration of Low Salinity EOR at Interwell Scale, Endicott Field, Alaska," SPE paper 129692, presented at the SPE Improved Oil Recovery Symposium, Tulsa, Oklahoma, April 24-28, 2010.
26. Seccombe, J.C., Lager, A., Webb, K.J., Jerauld, G., et al.: "Improving Waterflood Recovery: LoSal™ EOR Field Evaluation," SPE paper 113480, presented at the SPE/DOE Improved Oil Recovery Symposium, Tulsa, Oklahoma, April 19-23, 2008.

27. Buckley, J.S., Takamura, K. and Morrow, N.R.: "Influence of Electrical Surface Charges on the Wetting Properties of Crude Oils," *SPE Reservoir Engineering*, Vol. 4, Issue 3, August 1989, pp. 332-340.

28. Sorbie, K.S. and Collins, I.R.: "A Proposed Pore-Scale Mechanism for How Low Salinity Waterflooding Works," SPE paper 129833, presented at the SPE Improved Oil Recovery Symposium, Tulsa, Oklahoma, April 24-28, 2010.

29. Vdovic, N.: "Electrokinetic Behavior of Calcite — The Relationship with Other Calcite Properties," *Chemical Geology*, Vol. 177, Issues 3-4, July 2001, pp. 241-248.

About the Authors

Dr. Quan Chen

Ph.D. in Nuclear Magnetic Resonance Petrophysics, Chinese Academy of Sciences

Dr. Quan Chen is a Senior Technical Support Engineer at Oxford Instruments Magnetic Resonance, Oxfordshire, U.K. Before moving to his current position, Quan was a Petroleum Engineering Specialist at Saudi Aramco's Exploration and Petroleum Engineering Center – Advanced Research Center (EXPEC ARC), a Reservoir Engineer and Nuclear Magnetic Resonance (NMR) Specialist at BP's Enhanced Oil Recovery (EOR) Technology Flagship Laboratories, a Supervisor of the Advanced Rock Properties (SCAL) Department at Core Laboratories, a Deputy Lab Director and Senior Petroleum Engineer at the Research Institute of Petroleum Exploration and Development, China National Petroleum Corporation, and a Post-Doctoral Fellow and Honorary Research Associate at the MRI Research Center, University of New Brunswick.

His research interests include EOR, NMR, geochemical modeling, special core analysis (SCAL), and CO_2 geological sequestration.

Quan has published over 60 scientific articles, and holds several U.S. and European patents. Some of his inventions have been successfully commercialized.

In 1988, Quan received his B.S. degree in Petroleum Engineering from the Northeast Petroleum University, Daqing, China. In 1991, he received his M.S. degree in Mechanics of Fluid Flow through Porous Media from the Chinese Academy of Sciences and the China National Petroleum Corporation, and in 2001, Quan received his Ph.D. degree in NMR Petrophysics from the Chinese Academy of Sciences.

Dr. Moataz O. Abu-AlSaud

Ph.D. in Energy Resources Engineering,
Stanford University

Dr. Moataz O. Abu-AlSaud joined Saudi Aramco in 2004, and is currently a member of the SmartWater Flooding team in Reservoir Engineering Technology Division, of Saudi Aramco's Exploration and Petroleum Engineering Center – Advanced Research Center (EXPEC ARC). His research interests focus on the fundamental understanding of multiphase flow inside carbonates from the nanoscale to the reservoir scale, as well as digital rock physics.

Moataz has been published in several highly cited journals, and is the author of numerous conference papers. He serves as a Technical Reviewer for the *Journal of Computational Physics*, the *Journal of Energy and Fuels*, and the *Journal of Petroleum Science and Engineering*.

In 2009, Moataz received two B.S. degrees, in Mechanical Engineering and Mathematics, from Rice University, Houston, TX. In 2012, he received an M.S. degree in Mechanical Engineering from King Abdullah University of Science and Technology (KAUST), Thuwal, Saudi Arabia, and in 2017, Moataz received his Ph.D. degree in Energy Resources Engineering from Stanford University, Stanford, CA.

Dr. Subhash C. Ayirala

Ph.D. in Petroleum Engineering, Louisiana State University

Dr. Subhash C. Ayirala is an Improved/Enhanced Oil Recovery (IOR/EOR) Specialist and is currently leading the SmartWater Flooding team in the Reservoir Engineering Technology Division of Saudi Aramco's Exploration and Petroleum Engineering Center – Advanced Research Center (EXPEC ARC), as the Focus Area Champion. He has more than 16 years of reservoir engineering experience in the oil and gas industry and six years in applied research.

Subhash played a major role in the successful execution of the SmartWater flooding multiscale research program, championed the development of the zero liquid discharge produced water management solution, in addition to unraveling the importance of injection water chemistry in the EOR portfolio to develop several novel hybrid recovery technologies.

Prior to joining Saudi Aramco, he worked as a Reservoir Engineer in Shell International Exploration & Production, Houston, TX. Subhash has authored or coauthored more than 90 technical papers, 60 journal publications, and holds 30 granted U.S. patents, and 15 pending patent applications.

He is a Society of Petroleum Engineers (SPE) distinguished member, and serves as executive editor for the SPE *Reservoir Evaluation & Engineering Journal*. Subhash also serves as one of the Executive Editors for the *Journal of Petroleum Science and Engineering (JPSE)*, an Elsevier international journal. He received the SPE Outstanding Technical Editor recognition 10 times in between 2008 and 2021, and is the recipient of the 2017 SPE "A Peer Apart Award." Subhash also received the 2019 SPE Middle East and North Africa Regional Service Award. He recently served as the SPE Distinguished Lecturer on "SmartWater Flooding" during the 2021-2022 lecture season.

Subhash received both his M.S. and Ph.D. degrees in Petroleum Engineering from Louisiana State University, Baton Rouge, LA. He also holds a B.Tech and an M.Tech degree in Chemical Engineering from Sri Venkateswara University, Titupati, and the Indian Institute of Technology, Kharagpur, India, respectively.

Dr. Ali A. Al-Yousef

Ph.D. in Petroleum Engineering, University of Texas at Austin

Dr. Ali A. Al-Yousef is a Chief Technologist of the Reservoir Engineering Technology Division in Saudi Aramco's Exploration and Petroleum Engineering Center – Advanced Research Center (EXPEC ARC). He has more than 27 years of experience in upstream research and technology. Since joining Saudi Aramco, Ali has been involved in applied research projects focusing on improved oil recovery (IOR), waterflooding, enhanced oil recovery (EOR), and advanced reservoir evaluation/monitoring.

He is currently overseeing the implementation of several mega-scale pilots on CO_2 EOR, SmartWater and field deployment of electromagnetic-based technologies, advanced tracers, magnetic nanomappers for IOR/EOR, and reservoir evaluation and monitoring applications, and zero liquid discharge produced water management.

Ali has written over 120 conference papers, 50 journal articles, and has 40 granted patents, with more than 30 pending patent applications. He is an active member of the Society of Petroleum Engineers (SPE) and has chaired several SPE workshops and forums, helped organize several petroleum engineering related conferences, and taught courses on IOR/EOR and waterflooding.

In 2015, Ali received the Saudi Aramco President and CEO Excellence Award in recognition for significant contributions made toward IOR/EOR research. He was the recipient of SPE's prestigious IOR Pioneer Award in 2016 for his significant contributions made to the advancement of recovery technologies.

Ali was recognized by The Custodian of the Two Holy Mosques in 2018 for his pioneering invention on SmartWater flooding technology. He has also been elected as a 2021 Fellow of the Energy Institute, the highest level of EI recognition awarded to energy's leaders and influencers. Ali also received the 2021 SPE Distinguished Member Award.

He received his B.S. degree in Chemical Engineering from King Fahd University of Petroleum and Minerals (KFUPM), Dhahran, Saudi Arabia, and his M.S. and Ph.D. degrees, both in Petroleum Engineering, from the University of Texas at Austin, Austin, TX.

Novel Density-Based Autonomous Inflow Control Device Using Artificial Gravity

Stephen Greci, Dr. Michael Fripp, Ryan McChesney, Ibrahim El Mallawany and Dr. Ahmed Y. Bukhamseen

Abstract /

A new class of autonomous inflow control devices (AICDs) have been developed, which balances production flow and restricts unwanted production fluids, even when there is no viscosity difference in the produced fluids. This novel AICD senses the density difference between oil and water and uses artificial gravity to amplify the buoyancy forces while eliminating the need for downhole orientation in the completion.

AICDs have effectively reduced water production and increased oil recovery since their introduction in the early 2010s. During initial production, AICDs balance the flow across the production zone. In later production, AICDs automatically restrict the rate from zones producing water. Commercially available AICDs primarily operate by sensing the viscosity difference between oil and water. In very light oil reservoirs, such as in parts of the Middle East, there is no significant viscosity difference. Previous density-based AICDs have been rejected because buoyancy forces are often overwhelmed by fluid forces and because they needed to be oriented with respect to Earth's gravity.

Density AICDs use floats that are buoyant in water and sink in oil to control fluid production. The key to the new density AICD is that the floats are housed in a spinning centrifugal rotor. This spinning density selector creates centripetal forces that multiply the buoyancy force, thereby magnifying the difference between oil and water. The magnified buoyancy forces are stronger than fluid friction forces and are sufficient to overcome suction forces on the valve seats. The centripetal acceleration creates an artificial gravity that is much larger than Earth's gravity, eliminating the need to orient the density AICD downhole. The density selector is spun by the production fluid so that larger centripetal forces are created in response to a larger drawdown. The result is a density AICD that will operate in real-world conditions, especially in the light oil formations of the Middle East.

The performance of this novel density AICD has been measured in flow loop testing and demonstrated in computer modeling. The flow loop testing achieved substantial water restriction and continued oil flow using oil and water with identical viscosities.

Introduction

Inflow control devices (ICDs) have been used successfully for the past 30 years as a way to even out the inflow profile of long horizontal completions and to maximize hydrocarbon recovery[1]. Long horizontal wells can suffer from premature water breakthrough due to the relatively thin pay zone being produced. Water breakthrough primarily occurs due to a faster drawdown on one section of the completion. The unbalanced drawdown can occur either from the frictional pressure losses along the completion in a homogeneous reservoir or due to permeability variations found in a heterogeneous reservoir.

The frictional pressure losses occurring along the completion causes higher flow rates to be produced at the heel of the reservoir vs. the toe, and is often referred to as the heel-toe effect. With increased depletion at the heel, the hydrocarbon layer or pay zone at the heel is more quickly depleted in this area, leading to water breakthrough. In heterogeneous formations, the highly permeable sections of the reservoir are depleted first.

The depletion of this high permeability section can lead not only to water breakthrough, but also to an uneven production profile. This phenomenon is exacerbated in naturally fractured reservoirs where the water can be introduced unexpectedly by fractures connecting the water zone to the wellbore. In all these examples, uneven production is a key contributing cause of water breakthrough and ultimately of inefficient hydrocarbon recovery.

ICDs create an additional restriction at the sand face, which helps even out the pressure profile, and therefore, the influx, along the completion. This balancing of the inflow along the completion can negate the heel-toe frictional effect, as well as mitigate high permeability compartments in the well. While ICDs can delay the breakthrough of water, once water eventually breaks through, ICDs are not able to slow the water production. The production of water leads to expensive water disposal costs and less overall production of the remaining hydrocarbons, although there is still greater hydrocarbon production with an ICD completion than a standalone completion.

Autonomous ICDs (AICDs) were introduced in the 2010s as an improvement over traditional ICDs in that they can autonomously create an increased restriction once water is encountered. AICDs provide the same water breakthrough delaying mechanism as an ICD, with an added benefit of significantly restricting water production once breakthrough eventually occurs. This restriction of water is done autonomously, without any operator intervention. When comparing three different completion methods in the same type of reservoir, an AICD decreases water production and increases oil production over an ICD, and an ICD is a significant improvement over stand-alone screens.

In Fig. 1, the size and color of the arrows indicate the relative rate and type of fluid being produced after water has broken through the pay zone and into the completion tubing at the heel.

AICDs have historically functioned based on the viscosity difference between oil and water, however, the narrower this viscosity difference becomes, the more difficult it becomes for the AICDs to differentiate between the two fluids. There are fluidic diode type AICDs that are precise enough that they are able to discriminate between oil and water even when their viscosity difference is similar to the viscosity difference between hot and cold water[2].

While the majority of the reservoirs around the world have a viscosity difference between oil and water that is measurable, there are certain regions of the world, especially in the Middle East, where that viscosity difference is negligible. In these reservoirs, a new class of AICDs were needed that can discriminate between oil and water based on another fluid property besides viscosity.

This article will discuss past attempts and one current method of creating an AICD that functions solely based on the density difference between oil and water.

Floaty Ball AICD

There have been several attempts in the energy industry at creating an AICD that functions based on the density difference between produced fluids. One of the earliest approaches used balls of differing densities. This "floaty ball" density AICD used balls that float in water but not in oil, to rise and to seal off nozzles as the water level in the device rose[3]. The device incorporated bypass nozzles to allow the fluid inside the device to change as the produced wellbore fluids changed, even if all of the active nozzles were plugged, Fig. 2.

One of the major drawbacks of the floaty ball device was that the buoyancy forces acting on the density balls were too small. A floaty ball AICD would not actively toggle back and forth between low restriction in oil

Fig. 2 *The floaty ball AICD uses balls that float in water and sink in oil.*

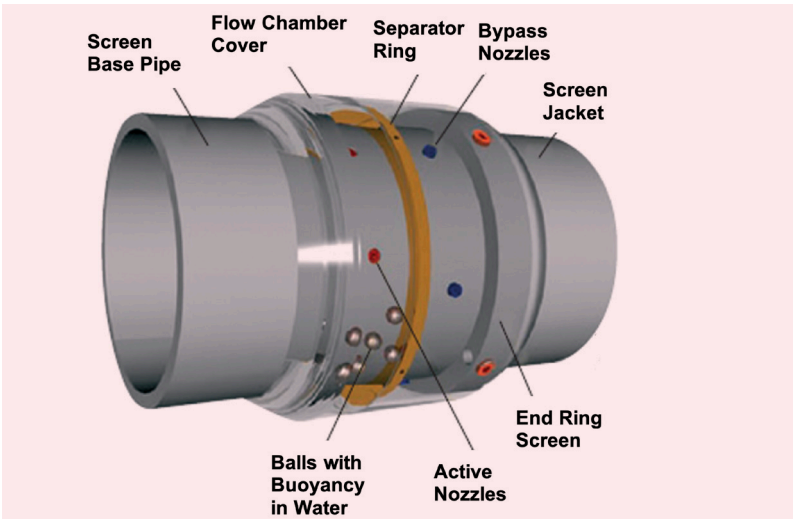

Fig. 1 *A comparison of the production profiles of three different completion designs in a homogeneous reservoir. The blue arrows represent water flow and the brown arrows represent oil flow.*

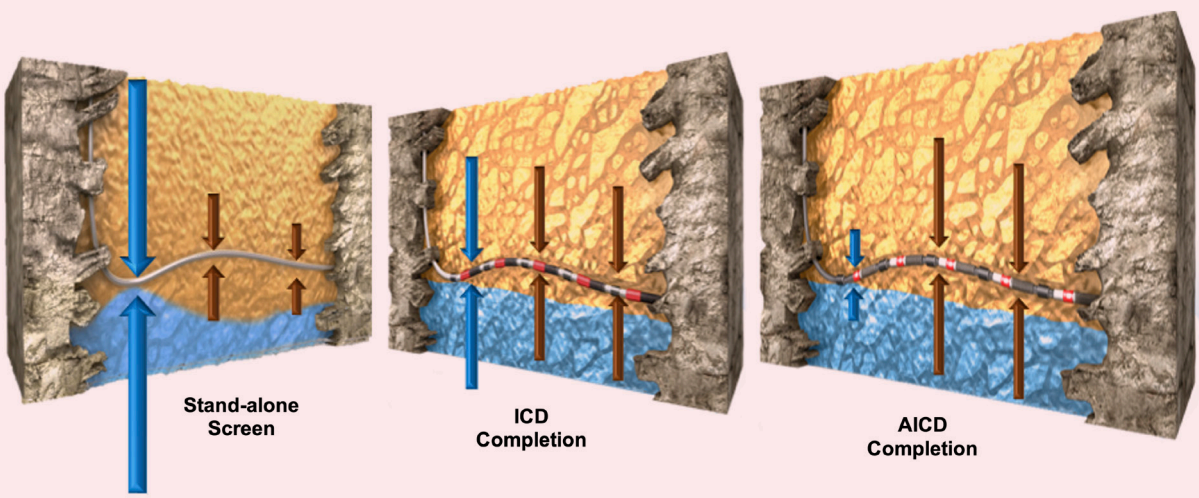

and high restriction in water as the production fluids changed. The inability to toggle the inflow restriction as the fluids change was due to the small buoyancy forces acting on the density balls.

The buoyancy forces acting on the density ball in a floaty ball AICD are inherently small because of the physical limitations on fluids and on size. The net buoyancy force acting on a ball, F_b, is given by:

$$F_b = (\rho_{fluid} - \rho_{ball})\, V_{ball}\, g. \quad (1)$$

where F_b is the buoyancy force in newtons, ρ_{fluid} is the fluid density in kilograms/meter^3 (kg/m^3), ρ_{ball} is the ball density in kg/m^3, V_{ball} is the ball volume in m^3, and g is the gravitational acceleration in meter/second^2.

The buoyancy force depends on the difference between the density of the fluid and the density of the ball. The buoyancy force also depends on the volume of the ball and the gravitational acceleration that is acting on the ball.

For the floaty ball AICD to be able to adjust the amount of restriction as the produced fluids change, the buoyancy force must be larger than the differential pressure forces holding the density ball onto its active nozzle. If the pressure forces holding the density ball on its ball seat is larger than the buoyancy force, then the ball will never come off of the active nozzle as the fluid in the wellbore changes. The pressure force is the differential pressure multiplied by the area of the active nozzle. Low net buoyancy forces acting on the density ball will require a small diameter of the active nozzle.

The net buoyancy force of a floaty ball AICD can be calculated using the force calculation in Eqn. 1. The density of the ball must be less than the density of water and greater than the density of oil, which requires the ball density to be approximately 900 kg/m^3. The density of oil in many formations is approximately 800 kg/m^3. With this design, using a full diameter base pipe and housing, the ball diameter is limited to about 10 mm. If the drawdown pressure is 100 psi, then there will be approximately a 100-psi differential holding the ball on the nozzle seat.

For the buoyancy forces to be larger than the pressure forces holding the ball on the active nozzle, then the nozzle would have to be smaller than 0.03 mm (0.0012") to enable the floaty ball to drop off seat when the fluid switches back to oil from water. This size nozzle is at least 10 times smaller than a typical sand screen opening that the device would be attached to. This size nozzle would plug quickly.

In addition to the challenges of plugging, a floaty ball AICD requires a significant number of perforations to get any appreciable production. With horizontal oil wells commonly having slugs of water being produced, the inability to toggle the restriction as the fluids change without fully shutting down production makes a floaty ball AICD design undesirable.

Another issue found during testing with a floaty ball AICD device is that the net buoyancy forces can be smaller than the hydraulic forces from fluid friction. These hydraulic forces from the flowing fluid can cause the density balls to go on seat prematurely. The density balls can go on seat and can restrict flow without notice during oil production. While regular production shutdowns could reset the devices, this would be time-consuming and inefficient. There is also a risk that cross flow during these shut-ins would prevent roughly half of the balls from ever coming off their seats, even during a shutdown.

Working Principles of a Centrifugal Fluid Selector

The key to a successful density-based AICD is to increase the buoyancy force acting on the floats. When examining the buoyancy equation, Eqn. 1, there are limited options for increasing the buoyancy force. The density difference cannot increase because the density of the produced fluids is fixed. The volume of the floats is limited by the wall space. Instead, the net buoyancy force can be increased by increasing the gravity acting on the floats. The apparent gravitational acceleration can be increased by spinning the floats and the fluid surrounding the floats to create a centripetal acceleration. The rotation creates an artificial gravity acceleration that can be many times larger than Earth's gravity.

The centrifugal fluid selector uses produced fluids to spin the floats. After passing through the screens, the produced fluids are directed toward the fluid selector. The jetting nozzle acts like an ICD and helps to balance the production. This fluid jet spins the centrifugal fluid selector and provides a centripetal acceleration, or artificial gravity, to enhance the buoyancy force on the floats. The artificial gravity felt by the floats can easily be 30 times Earth's gravity. This significantly increases the acceleration felt on the floats and multiplies the buoyancy forces induced by the floats by 30 times. The increased acceleration also makes the 1 g of acceleration from Earth to be negligible, thereby eliminating the need for downhole orientation.

The behavior of the centrifugal fluid selector can be counterintuitive, but understanding its behavior can be facilitated with a simple analogy. Consider two containers where each container is full of a different fluid and each is holding a baseball, Fig. 3. A baseball has approximately a density of 900 kg/m^3 and a volume of 300 cm^3. The container on the left contains freshwater, the container on the right contains oil with a density of 800 kg/m^3. When left alone, the buoyancy force exerted by the ball can be found by using Eqn. 1, which calculates 0.294 newtons of net buoyancy force.

Artificial gravity can significantly amplify the buoyancy forces exerted by the ball. Suppose the containers are swung by a rope, Fig. 4. The same two containers and the same baseballs are now rotated at a rate of two revolutions per second at a distance of 1 m between the ball and the person swinging the container.

The centripetal acceleration due to the rotation of the container, a_c, is given by:

$$a_c = \omega^2 r. \quad (2)$$

Fig. 3 *A float shown in a container of water on the left, and a container of oil on the right; Earth's gravity of 1 g is felt by the float.*

Fig. 4 *A float shown in a container of water on the left, and a container of oil on the right, being rotated around the person.*

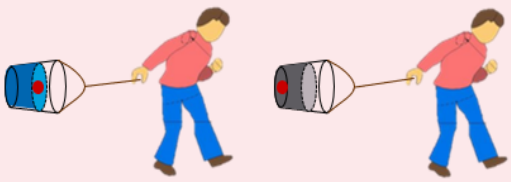

where a_c is the centripetal acceleration due to the rotation of the container, ω is the angular velocity, and r is the distance from the center of the ball to the axis of rotation.

In this rotating scenario, the buoyancy force is dominated by the centripetal acceleration rather than the gravitational acceleration. As a result, the buoyancy force in the centrifugal fluid selector can be approximated as:

$$F_b = (\rho_{fluid} - \rho_{ball})\, V_{ball}\, a_c. \quad (3)$$

Rotating the ball and fluid results in a significant increase in the buoyancy force. In the softball-in-a-bucket example, the centripetal acceleration exerted on the ball results in a net buoyancy force of 4.7 N. This rotation amplifies not only the positive net buoyancy force from the float in water but also the negative net buoyancy force from the float in oil by the amount of the artificial gravity, in this case 16.1 g. With this rotation, the 1 g of acceleration due to Earth's gravity can be considered negligible, and the ball will go toward the axis of rotation when it is in water or any other fluid that is a higher density than the ball. The ball will go away from the axis of rotation when it is in oil or any fluid that is a lower density than the ball.

The floats can be packaged into the centrifugal fluid selector, Fig. 5. The density floats, shaped as balls, are located inside of a rotor. The rotor spins when the production fluid hits the impulse turbine-style blades on the perimeter of the rotor. Just as in the simple example with a baseball in a bucket, these density balls move inward when they are surrounded by the denser water and move outward when the balls are surrounded by the lower density oil.

The floats move radially in their rotating chamber. The floats will block or unblock the flow paths exiting the center of the centrifugal fluid selector. Blocking or unblocking the flow paths passing through the center of the rotor results in the rotor blocking water and allowing the production of oil. The output from the centrifugal fluid selector can be used as a pilot to trigger a secondary valve that can provide more significant choking of the production flow.

The forces acting through the center of gravity of each ball (float) can be represented in a free-body diagram, Fig. 6. The forces acting on the ball are limited to the F_b, and the pressure differential from the flow paths. The buoyancy forces on the float can be increased by increasing the speed of rotation, the diameter of the

Fig. 5 *The density balls move inward when rotating in water (left) and move outward when rotating in oil (right).*

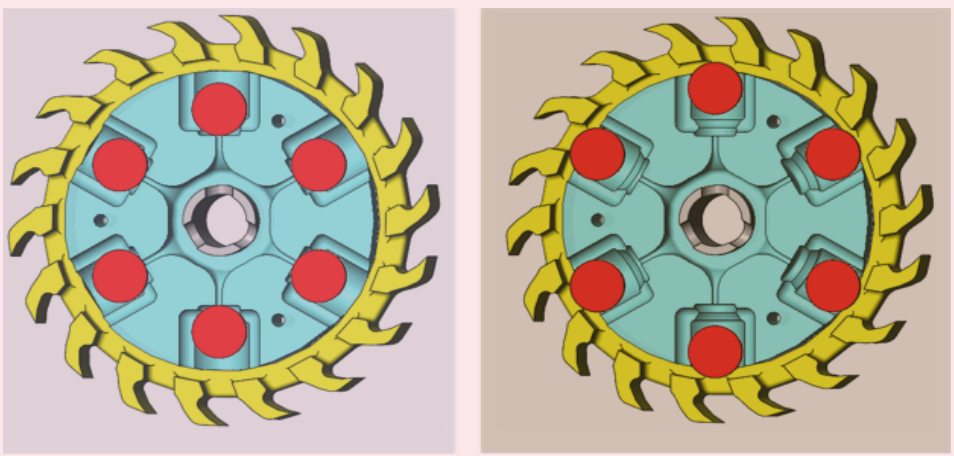

Fig. 6 *A diagram of forces acting on a ball-based rotor design.*

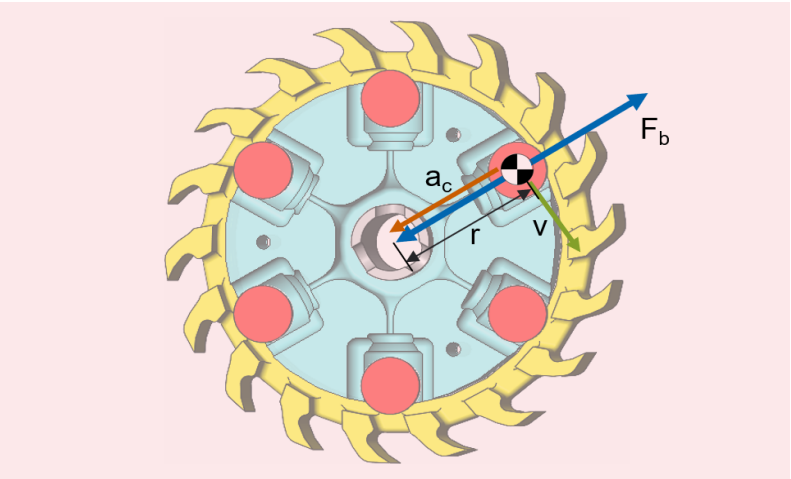

rotor, or the volume of the float. Downhole tools are limited by size and the diameter of the rotor is limited by the available wall thickness of the tool.

The speed of rotation is limited by the drawdown pressure, which is determined by reservoir conditions and by the pressure drop at the nozzle that is needed to balance production along a long horizontal. Increasing the buoyancy float force is important because it increases the allowable diameter of the flow path where the ball can pull itself off once the water has receded and oil is available to be produced again.

The centripetal acceleration from the rotation increases the buoyancy force by a factor of up to 100 over the buoyancy forces in the prototype floaty ball AICD. The outward net buoyancy force is up to 100 times larger when the ball is surrounded by oil and the ball is forced outward in oil. The inward net buoyancy force is also up to 100 times larger when the ball is surrounded by water and the ball is forced inward in water.

When this centrifugal fluid selector is compared to the floaty ball design that has no rotation, the diameter of the flow path that the float is able to pull off of with 100 psi differential is 10 times larger in diameter. In reality, the force calculation is more complicated because the radial distances change as the floats move outward and inward. Changes in the radial distance between the float and the center of rotation result in changes in the induced centripetal acceleration. Dynamic hydraulic forces from the moving fluid are also present and were accounted for in the full analysis.

A larger flow path makes the design more robust against possible clogging with fines or sand. Increasing the flow path necessitates increasing the buoyancy forces. Another avenue for increasing the buoyancy force is to increase the volume of the floats. To allow for larger floats while maintaining the same velocity and diameter of the rotor, the floats needed to evolve beyond the original spherical shape of the floaty ball AICD. In the next design iteration, the floats were

Fig. 7 *The levered floats hinge inward when surrounded by water (top) and hinge outward when surrounded by oil (bottom).*

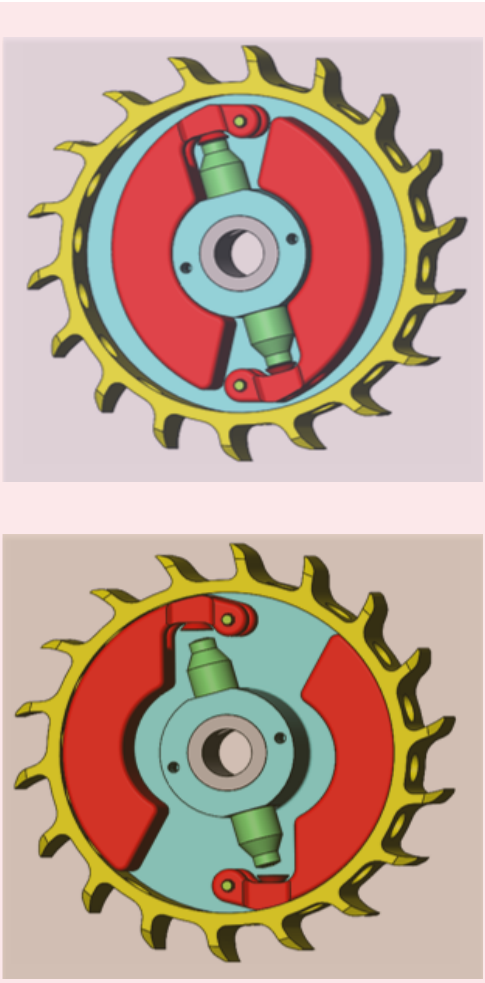

Fig. 8 *A diagram showing the forces acting on a levered float-based centrifugal design.*

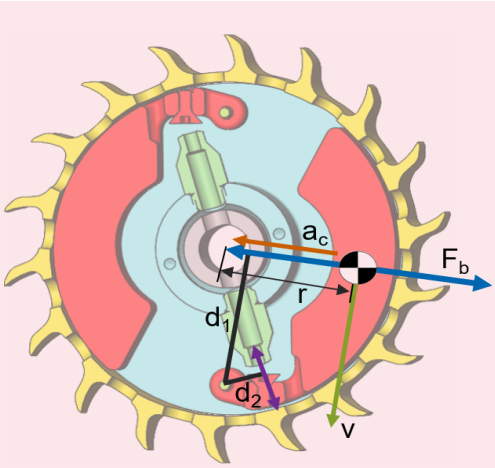

curved to maximize their volume as well as levered to maximize their mechanical advantage, Fig. 7.

The force acting on the levered float design can be represented by a free-body diagram, Fig. 8. The effect of the differential pressure on the floats is reduced by the distance ratio through the mechanical advantage of a lever. The lever distance for the float, d_1, is the perpendicular distance between the fulcrum and the buoyancy force direction acting through the center of gravity of the float. The lever distance for the pressure forces, d_2, is the perpendicular distance between the fulcrum and the pressure suction force direction.

By maximizing the volume of the floats and by using a lever to provide an additional mechanical advantage, the flow path opening that the float is able to pull off of when going from water to oil is significantly increased. This allows for more flow rate through the device and eliminates the risk of plugging. The differential pressure force that the float can overcome, F_b, is given by:

$$F_b = (\rho_{fluid} - \rho_{ball})\, V_{ball}\, a_c\, (d_1/d_2). \quad (4)$$

Using the same calculations for angular velocity and for the density of the fluids, the buoyancy force can be amplified again by using a float that is 10 times larger by volume. The net buoyancy force from the levered centrifugal design is now 10 times larger than the force from the ball-rotor design and 1,000 times larger than the floaty ball design.

The mechanical advantage provided by the levered floats increase the differential pressure that the buoyancy force operates by an additional factor of eight. The centrifugal fluid selector can toggle against flow paths that are thousands of times larger than the flow paths allowed by a floaty ball AICD. The centrifugal design for a density AICD results in an autonomous device that can perform in downhole conditions and will automatically restrict water, automatically allow oil passage, and automatically balance the production along the length of the completion.

Test Data

The centrifugal fluid selector operates with a nearly constant pressure differential across the device even as it switches between restricting water production and encouraging oil production. The rotational speed of the centrifugal fluid selector is determined by the desired drawdown pressure and the entry nozzle size required to balance the horizontal completion. The floats will move in or out depending on the bulk properties of the fluid encountered. The floats moving in one direction will bring the float nozzle plug onto the seat, restricting flow. The floats moving in the opposite direction will pull the float nozzle plug off the seat, increasing the flow rate.

Testing of the fluid selector consisted of holding a constant inlet pressure (formation pressure), while slowly increasing the total drawdown pressure to define a basic operating envelope. At each drawdown pressure step, the test fluid was swapped from 100% oil to 100% water, and the float position and flow rate was recorded. The fluid selector floats were able to open at a low differential drawdown pressure. Higher drawdown pressures increase the speed of the centrifugal fluid selector and make it possible to open at even higher chamber pressures by increasing the force available to pull the floats off the seat. Figure 9 shows the pressure flow results from a typical switching between oil and water, showing substantial changes in the flow restriction.

The centrifugal fluid selector was also tested in conjunction with a full density AICD system. Testing

Fig. 9 *The pressure flow results from a typical switching between oil and water, showing substantial changes in the flow restriction.*

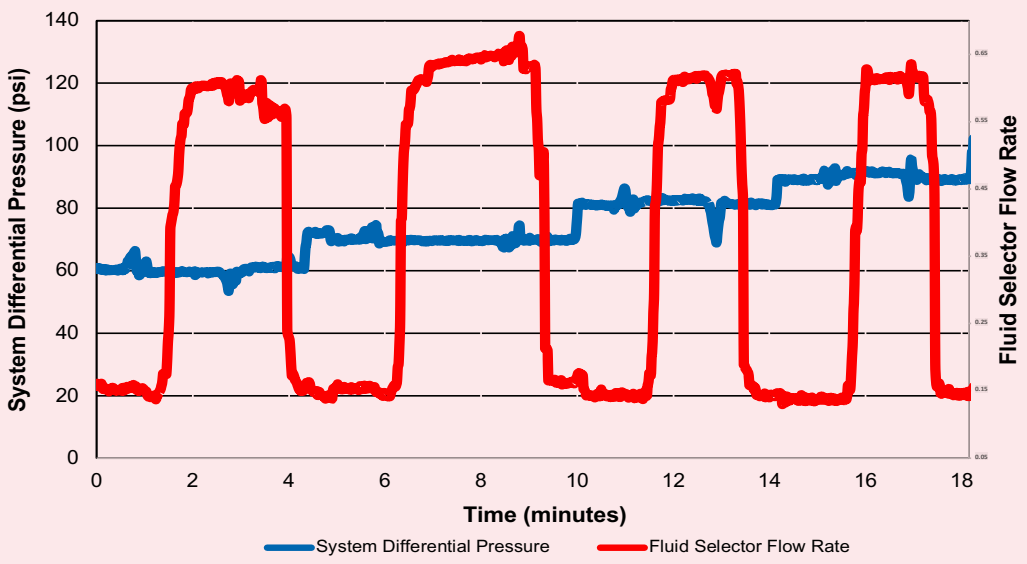

Fig. 10 *The combined system was found to have an oil to water production ratio of approximately 11:1 at 100 psid drawdown.*

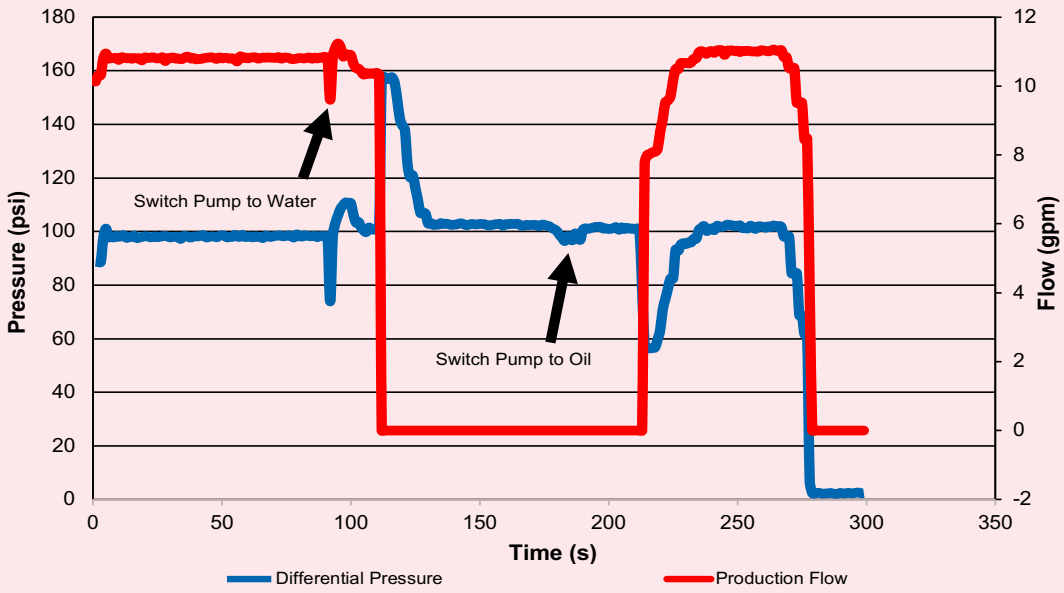

the subsystems together demonstrated that the fluid selector can provide an adequate flow rate to function the system. The combined system was found to have an oil to water production ratio of approximately 11:1 at 100 psid drawdown, Fig. 10.

System testing consisted of cycling the system from oil production to water production, simulating water breakthrough, and then returning to oil production, while maintaining 100 psid. When the system is producing oil, the total production flow rate is the sum of the flow rate through each subsystem. The centrifugal fluid selector always requires a flow rate to rotate the

Fig. 11 *A custom flow loop was created to perform both system testing and fluid selector testing.*

Fig. 12 *The additional custom flow loop created for the bearing test flow loop.*

fluid selector, regardless of the fluid type produced.

A custom flow loop was created to perform both system testing and fluid selector testing, Fig. 11. The flow loop is capable of testing drawdown pressures of up to 225 psi and able to perform single and multiphase flow.

In addition to the system and subsystem testing completed for the density AICD, a component reliability test was completed for the fluid selector bearing. The testing utilized an additional custom flow loop, Fig. 12. The bearing test flow loop can test up to five bearings simultaneously.

By utilizing this flow loop, it was possible to characterize several bearing types and materials. It was also possible to monitor leak rate, speed, and flow rate in real time. In addition to the data collection capabilities, the system provided a method to vary the loading conditions on each bearing to better characterize the long-term reliability of the components.

Conclusions

A new class of density-based AICDs have been developed and tested. These density AICDs autonomously and automatically restrict water production solely based on the density difference between oil and water. A novel centrifugal fluid selector increases the gravitational forces acting on levered floats, which increases the net buoyancy force by thousands of times over a float ball style density AICD.

The tests performed on this novel centrifugal density AICD demonstrate that it is possible to create a reliable device that operates solely off of the density differences in downhole fluids. This device is able to delay water breakthrough by utilizing field proven ICD pressure drops along the horizontal completion while providing a significant autonomous restriction if water eventually breaks through. By using the artificial gravity generated in the centrifugal fluid selector, the new density AICD operates with large flow paths, does not require downhole orientation, and toggles fluid restriction autonomously without needing to pause production.

Nomenclature

a_c = centripetal acceleration (m/s^2)

d_1 = perpendicular distance between the fulcrum and the buoyancy force direction acting through the center of gravity of the float (m)

d_2 = perpendicular distance between the fulcrum and the pressure suction force direction (m)

F_b = buoyancy force (N)

g = acceleration toward gravity (m/s^2)

r = distance from the center of the ball (or float) to the axis of rotation (m)

V_{ball} = ball (or float) volume (m^3)

ρ_{fluid} = fluid density (kg/m^3)

ρ_{ball} = ball (or float) density (kg/m^3)

ω = angular velocity (rad/s)

Acknowledgments

The authors would like to thank Ryan Novelen, Chad Glaesman, Richard Ornleaz and Hadi Arabnejad Khanouki for their time spent in the concept development of the density-based AICD.

References

1. Brekke, K. and Lien, S.C.: "New, Simple Completion Methods for Horizontal Wells Improve Production Performance in High-Permeability Thin Oil Zones," *SPE Drilling and Completion*, Vol. 9, Issue 3, September 1994, pp. 205-209.

2. Corona, G., Yin, W., Fripp, M., Coffin, M., et al.: "Testing of a Novel Autonomous ICD with Low-Viscosity Multiphase Fluids," OTC paper 27789, presented at the Offshore Technology Conference, Houston, Texas, May 1-4, 2017.

3. Freyer, R., Fejerskov, M. and Huse, A.: "An Oil Selective Inflow Control System," SPE paper 78272, presented at the European Petroleum Conference, Aberdeen, Scotland, U.K., October 29-31, 2002.

About the Authors

Stephen Creci

B.S. in Mechanical Engineering, Louisiana Tech University

Stephen Greci is a Technical Advisor working in the Sand Screens technology group of Halliburton's Completion Tool division. He began his career in the oil and gas industry in 2007 when he joined Halliburton. Stephen has worked in various roles in the Sand Screens group, in research, and the Open Hole Isolation groups.

His focus has always been on inventing, testing, and commercializing innovative products primarily for downhole filtration, isolation, and flow control devices.

Stephen holds over 100 granted U.S. patents and has 11 published papers. He was part of the team that received the Hart's Meritorious Engineering Award for Engineering Innovation for work done on Halliburton's EquiFlow® Autonomous Inflow Control Device.

Stephen received his B.S. degree in Mechanical Engineering from Louisiana Tech University, Ruston, LA.

Dr. Michael Fripp

Ph.D. in Aeronautics and Astronautics, Massachusetts Institute of Technology

Dr. Michael Fripp is a distinguished Engineer who has created a broad range of innovations for the energy industry. He holds over 400 awarded and pending U.S. patents, many of which have been commercialized. Michael was the primary inventor of autonomous inflow control devices, dissolving frac plugs, and acoustic wireless telemetry. His innovations have become disruptive improvements in downhole oil and gas production.

Michael has been recognized as an Innovative Thinker by *World Oil Magazine*.

He is a licensed professional engineer, has authored numerous technical papers, and has coauthored four books.

Michael received his B.S. degree in Engineering Science and Technology from Virginia Tech, Blacksburg, VA. He received both his M.S. and Ph.D. degrees in Aeronautics and Astronautics from the Massachusetts Institute of Technology, Cambridge, MA.

Ryan McChesney

B.S. in Mechanical Engineering, Arkansas Tech University

Ryan McChesney is a Principal R&D Mechanical Engineer working within the Halliburton Completion Tools division. He has supported new product development within the sand screens and flow control group since joining Halliburton in 2013. Ryan has also led several different new product development projects since joining the group, ranging from SAGD, deepwater multizone, compliant sand control to downhole power generation and autonomous inflow control efforts. His work spans project initiation and concept development to product validation and commercialization.

Ryan is a licensed Professional Engineer in the State of Texas and has held various roles in the areas of research, operations, and manufacturing within the metal casting, nuclear power, and aerospace industries.

He has also coauthored 15 patents and several technical publications.

Ryan received his B.S. degree in Mechanical Engineering from Arkansas Tech University, Russellville, AR.

Ibrahim El Mallawany

M.S. in Petroleum Engineering, Texas A&M University

Ibrahim El Mallawany is a Principal R&D Engineer working within the Halliburton Completion Tools division in the Dhahran Techno Valley facility in Saudi Arabia. He works on developing new technologies for different completion tool divisions such as autonomous inflow control device technology, multiple logging tools, intelligent completions, sand control tools, unconventional tools, etc.

Ibrahim has received an award for engineering innovation from Hart Energy for his work on the Smartplex System. He has 13 granted U.S. patents and 12 more currently being reviewed. Ibrahim has also coauthored several publications.

He is a member of the Society of Petroleum Engineers (SPE). Ibrahim is a licensed Professional Engineer in the State of Texas.

In 2005, he received his B.S. degree in Mechanical Engineering from the American University in Cairo, Cairo, Egypt, and in 2011 Ibrahim received his M.S. degree in Petroleum Engineering from Texas A&M University, College Station, TX.

Dr. Ahmed Y. Bukhamseen

Ph.D. in Petroleum Engineering, Stanford University

Dr. Ahmed Y. Bukhamseen is a Petroleum Engineer working with the Production Technology Team of Saudi Aramco's Exploration and Petroleum Engineering Center – Advanced Research Center (EXPEC ARC). His extensive experience includes reservoir engineering, production operations and completions research and development. Ahmed's current research activities cover smart well completions, production optimization, fiber optic sensing and multiphase flow metering.

He has published several technical papers and holds three patents.

Ahmed received his B.S. degree from the Colorado School of Mines, Golden, CO, and both his M.S. and Ph.D. degrees from Stanford University, Stanford, CA, all in Petroleum Engineering.

A Novel Sulfide Scale Inhibitor for Squeeze Treatment of Ultra-Tight Sandstone

Dr. Cyril Okocha, Dr. Tao Chen, Dr. Alex Thornton and Dr. Qiwei Wang

Abstract /

Sulfide scaling can manifest both downhole and topside in sour production scenarios. The topside development can be mitigated via continuous strategic application of an appropriate sulfide scale inhibitor package; however, downhole sulfide scaling presents a more complex challenge. The continuous downhole application of sulfide scale inhibitors via capillary string and valve, or by being routed to the valve via existing gas lift architecture, are two common delivery options available to the operator, but are unfortunately both limited to providing scale control at injection valve depth and up-string.

More recent options for sulfide scale control from the reservoir to the wellhead include chemical impregnated proppant for prop-frack and gravel packed wells, however, these approaches present a partial solution, and require topping up of an active inhibitor chemical once the emplaced inhibitor becomes exhausted. Scale squeezing is the industry recognized chemical technology for providing proactive scale control from reservoir to the wellhead, however, for sulfide scale control scenarios, this technology option is currently poorly served as the industry lacks effective and robust sulfide squeeze scale inhibitors (S-SQSI).

A new squeezable polymeric sulfide scale inhibitor has been developed and engineered with optimum desirable scale squeeze characteristics, and then further tailored for application in high temperature, high salinity sour gas ultra-tight sandstone/chalk formations. The new molecule uses the basic structure of an existing novel class of a sulfide scale inhibitor, however, the sequence and nature of functional groups across the polymer's backbone were extensively modified and optimized to improve: (1) polymer retention and release character for extended squeeze lifetime, (2) thermal stability, (3) high calcium brine compatibility, and (4) low formation damage potential.

Prior to upscaling for bulk manufacture and subsequent field application, the new polymeric S-SQSI was formation damage coreflood tested using target well field conditions and an ultra-tight sandstone field core. The results of this remarkable coreflood investigation are presented, where core permeabilities of sub -0.001 mD were the norm. The flood was performed without interruption or issue, and achieved consistent and continuous formation damage data assessment throughout the 5-week post-squeeze shut-in flow back period at very low flow rates.

A sulfide scale inhibitor residual assay observed consistently elevated concentrations of scale inhibitor across the coreflood flow back "plateau phase," and indicated that the squeeze treatment could generate a significant squeeze lifetime, and this is further borne out by mass balance performed after deliberate premature termination of the coreflood, indicating that an excess of 90% of the injected scale inhibitor remained within the core.

Monitoring showed sandstone core permeability recovering rapidly following the start of backflow, with no evidence of any significant formation damage. Post-flood data indicated no loss of core plug integrity, and a mineralogical assay confirmed unchanged material composition. The formation damage sandstone coreflood results clearly demonstrated the suitability and robustness of this new sulfide scale inhibitor for squeeze application under extremely challenging conditions.

Introduction

Oil field sulfide scale formation (iron sulfide, zinc sulfide, and lead sulfide) is peculiar to sour production scenarios, and for many oil and gas fields the issue of sulfide scale management downhole presents a field challenge. Historically, sulfide scaling down well have featured reactive chemical dissolver interventions to recover well production once sulfide scale has deposited, and operators have published extensively on their experiences, i.e., coiled tubing deployed dissolver technologies used in well clean out treatments[1-4].

Unlike common carbonate and sulfate scales, there is no proactive squeeze scale inhibitor (SQSI) alternative for control and management of sulfide scale from the producer well's wellbore and upstream/downstream, therefore, the reliance and dominance of sophisticated reactive chemical dissolver-based interventions[5, 6]. There are few sulfide scale inhibitor options available generally to the industry as a whole, and this is due primarily to the ultra-low solubility of sulfide scales, and the rapidity with which sulfide scales form and precipitate from solution.

A new and novel polymeric scale inhibitor was developed and introduced to the industry in 2014[5, 7], which gained industry acceptance for topside and downhole application via continuous injection. Although highly effective and novel in its action for control of all sulfide scales, the polymer coreflood test performance precluded it from being deployed as a stand-alone SQSI, however, it did excel when deployed downhole as an additive in complex frack treatments in sour wells.

In 2017, a joint development initiative focused on reengineering the original active water-soluble polymer to tailor it for squeeze application in hot, tight, gas formations for the prevention of sulfide scale. Molecular engineering resulted in the creation of in excess of 100 viable sulfide scale inhibitor squeeze product variants. Extensive systematic performance ranking studies determined the most suitable scale squeeze product[8].

Proof of Concept Formation Damage Assessment

Proactive scale squeezing for control of downhole scaling is preferred to reactive remedial chemical application in the majority of cases, with treatment efficiency, longevity, economics, safety, and integrity benefits being cited[9]. In most SQSI application scenarios, the formation damage potential of the proposed treatment needs to be clearly understood, and will often provide final ranking discrimination between candidates.

The three best candidate variants underwent final ranking via their performance in formation damage coreflood tests using outcrop chalk cores. The best performing candidate required proof of concept (PoC) coreflood testing using real field conditions and real field core before it would be considered for upscaling to bulk manufacture and field trial.

Coreflood Study Objectives

This article describes the PoC coreflood experiment and the results obtained from application of sulfide SQSI (S-SQSI) into an ultra-tight sandstone field core. The primary objectives were: (1) minimal permanent impact on core permeability to gas and gas condensate, (2) significant scale inhibitor retention, (3) a useful average return residual scale inhibitor (RSI) during flow back, and (4) the potential for useful squeeze lifetime and/or extended squeeze lifetime.

Experimental Procedure

The coreflood experiment is designed to simulate a SQSI chemical treatment in field rock material. The formation damage potential of the treatment was assessed by comparing core permeability to oil/brine/gas before chemical pill application and then post shut-in and treatment flow back.

The target well is a significant gas and condensate producer, therefore, gas and liquid hydrocarbon permeabilities were considered key to determining the success or failure of the formation damage coreflood. Reduction in permeability to field brine while maintaining significant hydrocarbon permeabilities was considered to be desirable.

Field Core

Several pre-cut sandstone field cores were generously supplied by the field operator for the experiment, and after intensive mineralogical and integrity screening, one core stub was selected for the PoC coreflood. The core plug was shorter in length than desired and exhibited permeabilities to liquid and gas < 0.5 mD at 1,500 psi, Table 1, and mineralogical assay in Table 2.

Coreflood Test Brines

The target well produced water (PW) ion composition was adjusted and simplified to be comprised of sodium, calcium, magnesium, and chloride ions only, Table 3. Sodium chloride (NaCl) was used to adjust the ion balance. Prior to use, the brine was filtered (0.45 µm) and vacuum degassed.

The S-SQSI slug was prepared in 6% NaCl.

Gas

Oxygen free nitrogen was used as a gas analogue. The gas was humidified via flowing through a bubble cell at the test temperature and pressure. Humidification was included to minimize brine evaporation into the gas phase, as this could result in accidental salt precipitation within the core and potentially impact the

Table 1 *The key information for the sample field core plug.*

Confining Pressure	PV	Porosity Fraction	Permeability Klinkenberg	Permeability K_{N2}	Grain Volume	Grain Density	Dry Weight	Plug Length	Plug Diameter
(psi)	(cm^3)		(mD)	(mD)	(cm^3)	(g/cm^3)	(g)	(cm)	(cm)
800	4.246	0.115	0.420	0.606	32.655	2.67	87.166	3.427	3.850
1,500	4.070	0.111	0.260	0.422	32.655	2.67	87.166	3.427	3.850

Table 2 *The mineralogical assay of the core sample.*

Whole Rock Mineralogy Weight %								Clay (Phyllosilicates) Weight %	
Quartz	K-Feldspar	Plagioclase	Calcite	Dolomite	Siderite	Pyrite	Total Clay	Illite & Mica	Chlorite
91.9	2.5	0	0.4	0	0.5	0	4.7	4.1	0.6

Table 3 *The PW brine ion composition.*

Salt	PW (g/L)
NaCl	31.15
$CaCl_2.2H_2O$	42.63
$MgCl_2.6H_2O$	13.89

formation damage assessment.

Gas Condensate

Isopar™ was used to represent the field condensate as it was a good viscosity analogue. Measures were taken to ensure that the Isopar™ viscosity was maintained at the supplied viscosity.

PoC Coreflood Test

The PoC coreflood procedure is detailed in Table 4, and the test conditions and viscosities are listed in Tables 5 and 6, respectively.

Results

Permeabilities

Liquid permeabilities were assessed continuously throughout the coreflood, and core permeability to gas was determined on the cleaned core before and after the coreflood experiment, Table 7.

The core permeability to brine at residual gas condensate saturation, prior to inhibitor pill injection, was determined as 0.011 mD, and declined to 0.0004 mD during injection of the scale inhibitor pill. Following the shut-in period, injection of backflow brine witnessed steady increases in both core permeability to brine, and allowed (safe) brine flow rate, Fig. 1. The coreflood backflow period achieved 425 pore volumes

Table 4 *The coreflood treatment sequence.*

	Action	Medium	Measure	T (°C)	CP*/BP** (psi)	
1	Clean core plug and dry	Nitrogen	K_{N2}/Φ	RT	2,000	
2	Evacuate air from plug and saturate	PW	—	RT	2,000	
3	Load into coreholder, apply CP and BP	—	—	RT	1,500/500	
4	Flow PW at 1 mL/min and increase to target temperature	PW	ΔP and K_W	140	1,500/500	*FWD*
5	Flow gas condensate through core at 1 mL/min	Isopar™	ΔP K_o at S_{wi}	140	1,500/500	*FWD*
6	Flow PW through core at 1 mL/min	FW***	ΔP K_W at S_{or}	140	1,500/500	*FWD*
7	Flow PW + tracer at 1 mL/min	FW + [Li+]	ΔP PV	140	1,500/500	*FWD*
8	Flow PW at 1 mL/min	FW	ΔP	140	1,500/500	*FWD*
9	5 PV of 3% S-SQSI in 6% NaCl at 1 mL/min	SI Pill	ΔP	140	1,500/500	**REV**
10	Shut-in for 24 hours		ΔP	140	1,500/500	
11	Backflow PW at 0.1 mL/min for 1,000 PV	FW	ΔP	140	1,500/500	*FWD*
12	Flow (gas condensate) at 0.1 mL/min	Isopar™	ΔP K_o at S_{wi}	140	1,500/500	*FWD*
13	Flow PW at 0.1 mL/min	FW	ΔP K_W at S_{or}	140	1,500/500	*FWD*
14	Clean core plug (dry)	Nitrogen	K_{N2}/Φ	RT	2,000	

*CP = confining pressure **BP = back pressure ***FW = formation water

Table 5 *The coreflood test parameters.*

Parameter	Unit	Value	Comment
Test Temperature	°C	140	Reservoir Temperature
Injection Temperature	°C	140	Injection of Inhibitor Slug
Pore Pressure	psi	500	
Overburden Pressure	psi	1,500	
Overburden (confining) Pressure	psi	2,000	
Fluid Flow Rate	mL min^{-1}	0.1 – 1	
Shut-in	Hours	24	

Table 6 *The fluid viscosity at temperature.*

No.	Fluid	T (°C)	Viscosity (cP)
1	PW	140	0.213
2	PW + Lithium tracer (C_0 = 50 mgL^{-1})	140	0.213
3	Maintreatment (3% S-SISQ in 6% NaCl)	140	0.186
4	Isopar™	140	0.366

Table 7 *The PoC permeability measurements.*

Test Phase	Permeability	Additional	Flow Direction	Flow Rate (cm^3/min^{-1})	K (mD)
K_{N2}	Matrix-gas (before flood)	Room T			0.422
K_w	Matrix-brine	Test T&P	Production	0.1	0.0694
K_o at S_{wi}	Matrix-gas condensate at residual brine	Test T&P	Production	1.0	0.0968
K_w at S_{or}	Matrix-brine at residual gas condensate	Test T&P	Production	0.28	0.0115
K_{w+Li} at S_{or}	Matrix-brine + [Li+] at residual gas condensate	Test T&P	Production	0.28	0.0110
K_{INH} at S_{or}	Matrix-3% S-SISQ at residual gas condensate	Test T&P	Injection	0.02	0.00036
Shut-in for 24-hour soak period					
K_o at S_{wi}	Matrix-brine at residual gas condensate	After SISQ	Production	0.02	0.00255
K_W at S_{or}	Matrix-brine at residual gas condensate	End of Backflow	Production	0.02	0.03367
K_o at S_{wi}	Matrix-gas condensate at residual brine (end)	End of Backflow	Production	0.20	0.01350
K_W at S_{or}	Matrix-brine at residual gas condensate	End of Backflow	Production	0.08	0.0024
K_{N2}	Matrix-gas (after flood)	Room T			0.310

Fig. 1 *The PV vs. permeability plot detailing the key coreflood stages.*

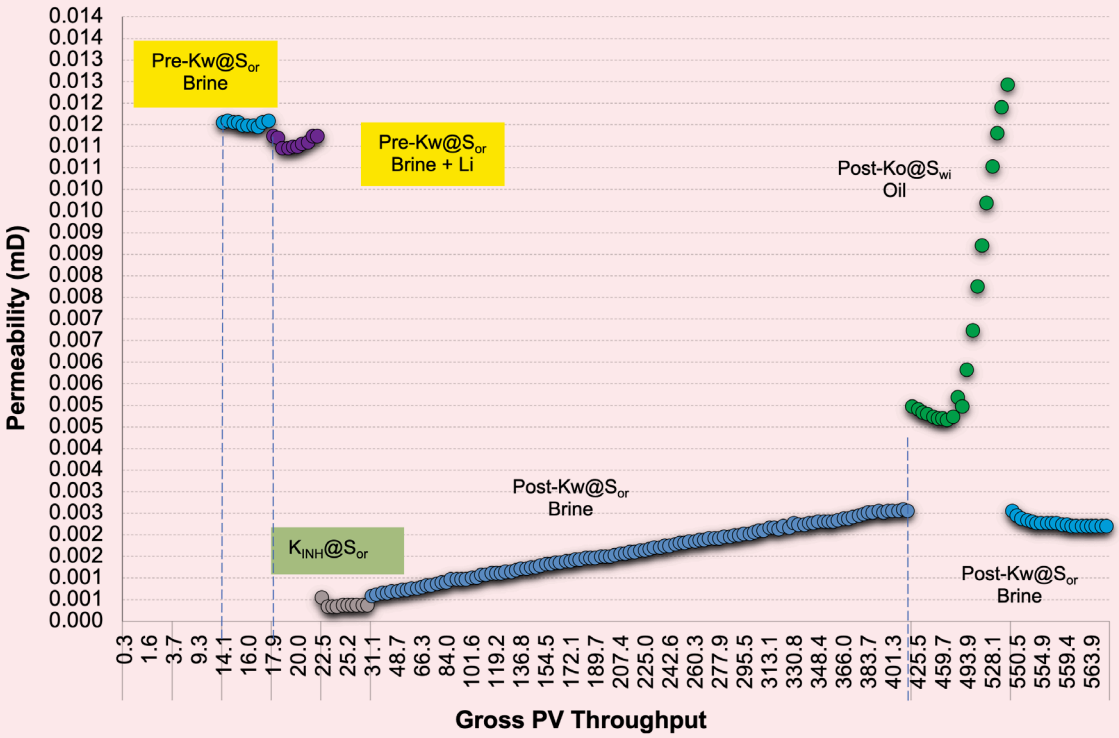

(PV) — total volume of fluids passing through the core — after approximately 5 weeks of continuous flow, and at this point it was agreed that continuing the flood to the original target of 1,000 PV would provide no additional benefit, as permeability and flow rate trends had been consistent across the 5-week backflow period. The coreflood was therefore prematurely ended at 425 PV total flow.

Post-flood permeabilities to gas condensate and brine confirmed observations from earlier permeability assessments that the core responded extremely well to introduction of gas condensate, and clearly preferred hydrocarbon transmission to brine transmission.

Following final permeability assessments, the core was cooled, and Dean-Stark assayed prior to final gas permeability determination. The permeability to gas was calculated as 0.310 mD, which represented a 26.5% reduction in core permeability to gas through squeeze treating of the core with S-SQSI. The reduction is believed to be misleading as the core permeability was continually recovering with time, indicating progressive release of the scale inhibitor molecules from the core.

The core still retained a large quantity of polymer that would not easily be mobilized during post-flood cleaning either by hydrocarbon or aqueous solution flushing. Had the coreflood proceeded to the original 1,000 PV backflow target, then existing trends suggested that the recovery of K_W@Sor would have continued as the large polymeric molecules were returned from the core.

Mass balance evaluation of S-SQSI indicated that approximately in excess of 90% of the inhibitor polymer injected into the sandstone core was still retained within the core at end of the flow back period.

Inhibitor Profiles

The S-SQSI molecule is amenable to conventional residual analysis techniques, however, the very large number of sample analyses required during the product development program required a faster analytical method. Since all brine samples were subject to multiple element analysis via inductively coupled plasma (ICP), it was decided to focus on the significant elemental sulfur content of the active polymer, and therefore, ICP [S] was employed for S-SQSI residual analysis.

To avoid issues of free sulfate ion adding to the total sulfur assay via ICP, all brines were adjusted, and their sulfate ion contents replaced by NaCl equivalents. All virgin brines, and all brines that had passed through the sandstone core were analyzed for the presence of elemental sulfur, and spot checked for free sulfate — via ion exchange chromatography — that may have been eluted from trace minerals within the core. The background dissolved sulfur/sulfate concentrations were determined to be very low, and therefore, believed would pose no issue with respect to an accurate assay of the scale inhibitor at low concentration.

The scale inhibitor return profile for the flood is presented in Fig. 2, and is typical for this class of novel polymer S-SQSI. The decay profile resembles a

Fig. 2 *The RSI values for S-SQSI in effluent samples during the coreflood backflow.*

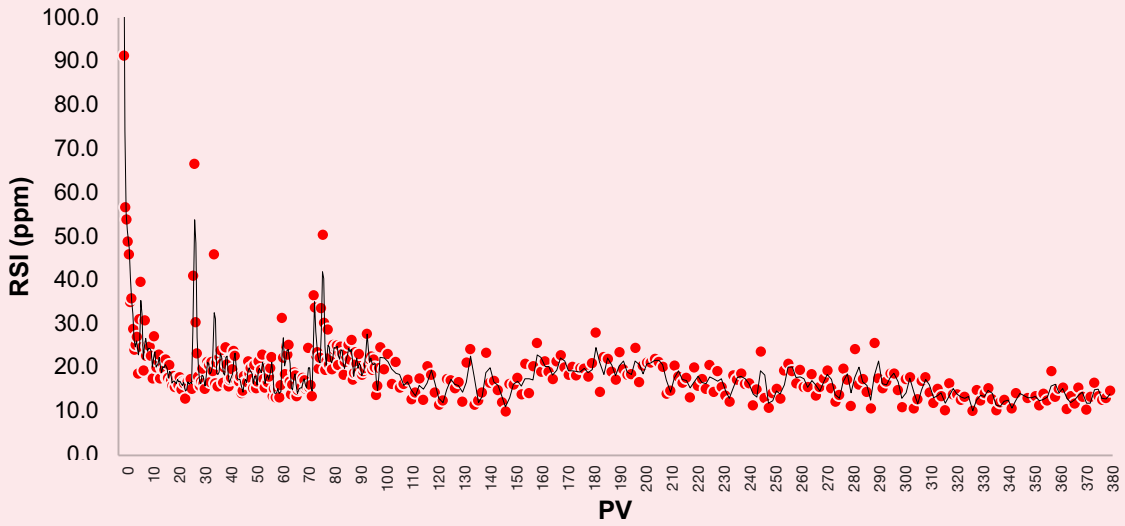

dispersion/precipitation type RSI return profile rather than a conventional adsorption squeeze RSI return.

The mixed retention behavior demonstrated in the RSI returns profile is understandable considering the size of the polymer molecule and the finite available free volume within the ultra-tight field core. It is believed that the polymer is likely to adopt a 3D space filling conformation while within the narrow confines of the pore channels. The polymer is configured with multiple anchoring groups throughout its structure and will adsorb with some facility onto available surface locations when entering the pore channels.

Additional molecules entering the core are then likely to be retained via physical interaction between the adsorbed and bulk flowing phase molecules resulting in their impeded progress and accumulation within the main pore chambers. At shut-in, it is envisaged that the bulk of the available free core PV in the ultra-tight core will contain inhibitor accumulations suspended in pore chambers and vugs awaiting the opportunity to enter the slowly flowing central fluid stream.

The core permeability to inhibitor solution was observed to decrease from 0.0111 mD (pre-slug injection K_w@Sor) to 0.00035 mD following injection of 5 PV of inhibitor solution in 6% NaCl, however, it had increased to 0.0025 mD by the time of the first post-slug K_w@Sor test. The RSI profile indicated that much material has been retained within the core as the usual initial expected high concentration slug of scale inhibitor in the first 5 PV to 10 PV backflow was largely absent.

The highest measured residual value was 3,177 ppm S-SQSI, which is approximately 11% of the input concentration. The mass balance calculation performed for the injection of 5 PV of 3% solution indicated that ~90% of the injected inhibitor was still within the core volume at the end of the backflow. A series of significant inhibitor spikes is noted at 25 PV to 30 PV and 75 PV to 80 PV, Fig. 2. It is suspected that these surges correlate with coreflood flow back injection rate increases causing a momentary surge of free inhibitor from the PV passing into the flowing stream in the center of the pore spaces.

The core ΔP dictates the safe backflow flow rate for the ultra-tight core. The flow backflow rate values are presented in Table 7, and it can be seen that during early backflow, the rate was approximately 0.02 mL/min, which increased by a factor of 10 to 0.2 mL/min by the end of the backflow period. After the RSI spikes, the flow back profile appears to stabilize suggesting conditions for surges in scale inhibitor from the core are no longer met.

The scale inhibitor concentration gradually decays from 18 ppm/20 PV to 14 ppm/388 PV. Extrapolation of the gradient beyond the 388 PV throughput value provides an estimated concentration of approximately 9.5 ppm at 1,000 PV.

Calcium and Magnesium Ion Concentrations

The backflow ion concentration profiles for magnesium and calcium are presented in Fig. 3 and essentially overlay one another perfectly across the duration of the flow back period. The profiles are also symmetrical with the reference sodium ion, suggesting no significant loss of metal ions occurred across the backflow period, and no significant divalent metal ions were gained across the backflow period.

The data confirmed that the inhibitor was not being retained as a calcium-polymer precipitate, and therefore, the precipitation mechanism considered for S-SQSI retention in the sandstone core was less relevant.

Digital Rock Characterization

The field core was assayed via high frequency computerized tomographic (HF-CT) analysis both before and after S-SQSI chemical application. The technique

Fig. 3 *The backflow core effluent calcium and magnesium ion concentrations.*

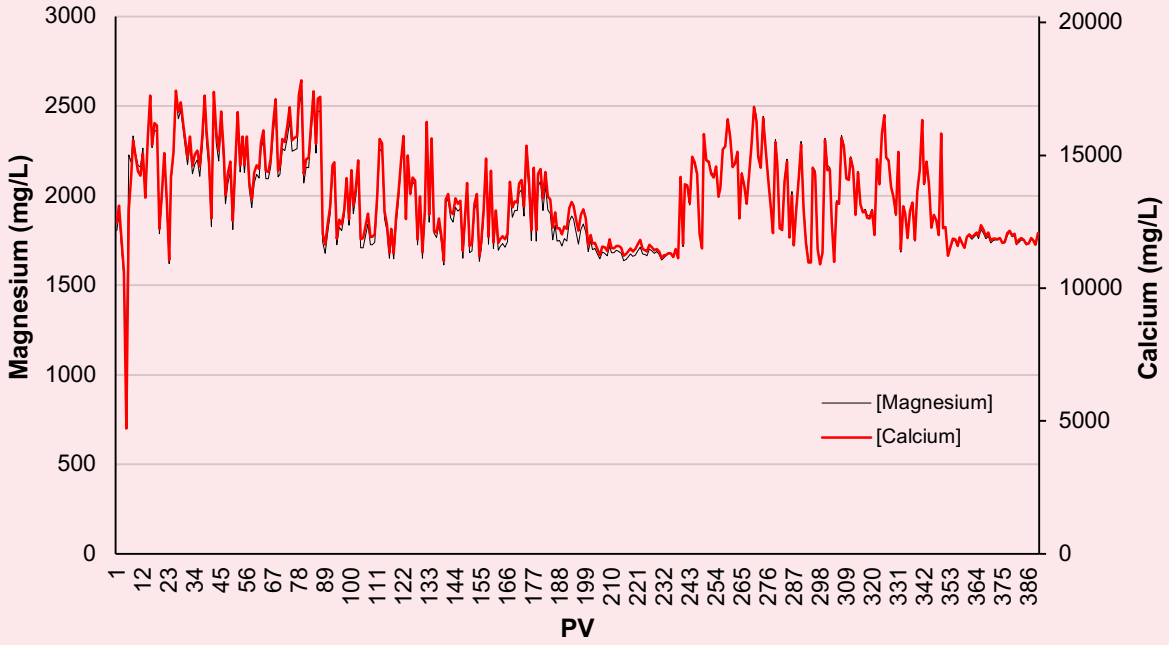

provides cross-sectional images from the core front (face) to the core rear (face), at predetermined distances between the image slices.

The collected image scan set can then be inspected from front to back, presenting a continuous 3D image representation of the core's internal structure and presence of mineral developments and structural irregularities. The image set presented in Fig. 4 display the core plug before and after coreflooding from the top cross and vertical section perspectives.

White deposits representing alternative higher density mineral species are spotted throughout the plug in both the pre- and post-coreflood images. It was assumed that the core plugs have not previously been exposed to laboratory coreflood experimentation and that the mineral species are natural mineral constituents of the field cores.

Discussion

The coreflood study was undertaken to determine whether the newly developed S-SQSI product can be safely squeeze deployed into a sour gas well with an ultra-tight sandstone well horizon. The field squeeze treatment was simulated in the laboratory via a PoC formation damage coreflood experiment performed under field conditions and using a real field core. The coreflood was performed successfully and all results clearly indicated that the new chemistry could be safely deployed into ultra-tight formations for control of sulfide scale. The squeeze lifetime longevity was considered to be very significant, and in the coreflood experiment, even after 5 weeks of backflow, greater than 90% of the scale inhibitor remained within the core, ready to perform scale inhibitor service.

The key to the assessment was the comparison of the pre- and post-treatment core plug gas permeabilities.

Core Permeability Gas

The coreflood results identified a 26.5% reduction in gas permeability as a consequence of deploying the chemical treatment into the core. The core was not damaged, and the reduction in gas permeability was temporary, and observed to be steadily declining as the coreflood flow back period progressed. The lower post-squeeze gas permeability was due to the available free volume space within the ultra-tight core being taken up with retained high molecular weight polymeric scale inhibitor. The inhibitor was effectively retained during polymer slug injection, and permeability testing performed throughout the flood clearly indicated the core δP decreased with time and elution of the polymer.

By the end of the flow back period, the core permeability to liquid transmission had essentially returned to the pre-treatment values, and if the flood had not been stopped prematurely, then the trends suggest that continued elution would have resulted in a further decrease in core δP and the knock-on effect of this would be a marked reduction in the net gas permeability loss.

Rock Matrix

The selection of a target gas well sandstone horizon rather than an ultra-tight chalk presented a new challenge. Additionally, all work performed up to this point had considered very high salinity and high calcium ion load PWs, therefore, the much lower salinity — almost 50% less saline — target well brine added another new dimension to the study.

The study up to this point had featured a number

Fig. 4 *The top axial sectional area and the vertical HF-CT of the plug before and after coreflooding.*

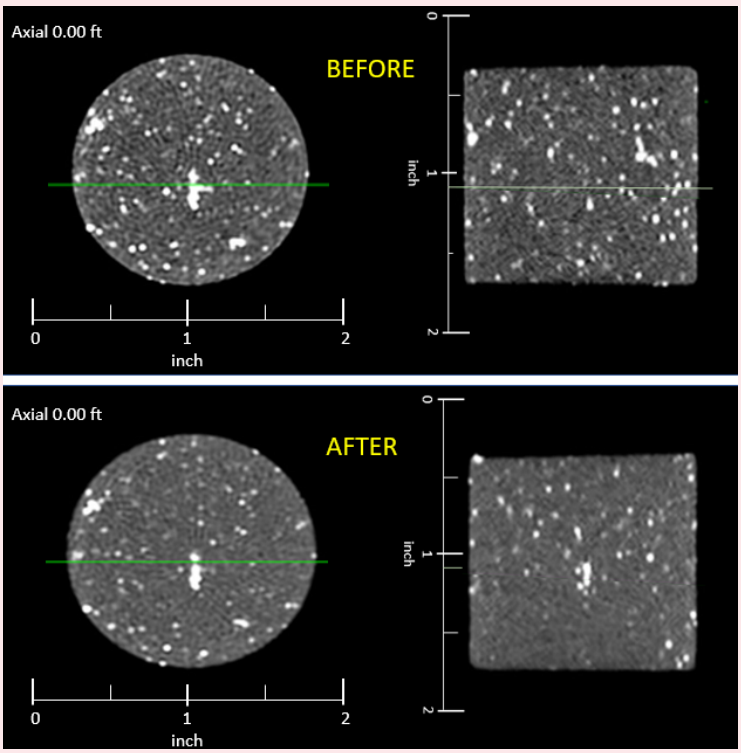

of chalk analogue corefloods as well as a high salinity ultra-tight sandstone coreflood using the new product, therefore, confidence was high for successfully squeeze treating an ultra-tight sandstone horizon.

RSI Retention Mechanism

The very low core permeability combined with the high molecular weight scale inhibitor resulted in an unusual RSI return profile that resembled a precipitation type return profile rather than an adsorption type. The precipitation type mechanism — very low initial returns and a long plateau phase — was quickly discounted once the backflow brine ion analysis and post-treatment HF-CT analyses were obtained, which suggested that no calcium inhibitor precipitation had occurred and deposited within the core.

The mechanism that fitted the accumulated data set was an adsorption/dispersion combination where the key factors were the very large polymer size and the very small and finite internal fluid conduit volumes within the sandstone core piece.

Other Observations

1. The core pressure remained constant during scale inhibitor injection as no increase was measured for over 18 hours at 0.02 mL/min per minute. The pre-squeeze liquid permeability of 0.01 mD was reflected in the very low core flow back flow rate of 0.01 mL/min.
2. The core greatly preferred the hydrocarbon fluid transmission over the brine transmission. It is suspected that the presence of hydrocarbon, rather than brine, causes adjustment of the spatial arrangement of the polymer resulting in a partial collapse of the 3D structure.
3. The high molecular weight polymer appeared to be retained via adsorption/dispersion and accumulate within the core PV.
4. The reduced net gas permeability of 26.5% is misleading. There was no evidence of formation damage and all effects observed were easily attributed to the narrow core pore channels being loaded with high molecular weight polymeric scale inhibitor.
5. At the time of the flood termination, mass balance calculations indicated that ~90% inhibitor was still retained within the sandstone core.
6. The HF-CT scans indicated no visible changes occurred with respect to core integrity before/after flooding.
7. The sandstone core contained a multitude of higher density accumulations throughout. Quartz density is 2.65 g/cm^3, and the mineralogical assay indicated that the most abundant higher density component was mica (2.88 g/cm^3) followed by siderite (3.96 g/cm^3); the other minerals identified tended to be almost indistinguishable density-wise from quartz.

Conclusions

The PoC coreflood indicated that the new S-SQSI product could be safely and effectively deployed in sour gas wells with an ultra-tight sandstone horizon. The residual decay profile for the new product indicated that the polymer was effectively retained within the ultra-tight core, and by the end of the 5-week coreflood backflow period, mass balance estimates indicated that at least 90% of the injected scale inhibitor still remained within the core to perform scale control duty. The squeeze lifetime predicted from the coreflood result is anticipated to be very long, and presented additional deployment considerations for field trial application.

Acknowledgments

The authors would like to provide a special mention to Scale Inhibitor Development Team members Lena Petrozziello and Christoph Kayser of Clariant Frankfurt and Jonathan Wylde in Clariant Houston, and Jairo Leal and Mohammed Bataweel, of Saudi Aramco, Kingdom of Saudi Arabia. Not forgetting our untiring Innovation Group Scale Technology Support Specialist Marjery Dela Cruz (Houston) and also the analytical support teams in both Frankfurt and Houston. Last but definitely not least, our thanks go to Dan Scott and his Specialty Core Flooding Team at Core Laboratories (Houston) who really broke new ground with these floods.

References

1. Green, T.A., Leal, J.A., Ginest, N.H., Al-Bu Ali, M.S., et al.: "Challenging HPCT Scale Removal Operations in High H_2S Environment Successfully Completed with Interdisciplinary Job Design and Execution," SPE paper 172129, presented at the Abu Dhabi International Petroleum Exhibition and Conference, Abu Dhabi, UAE, November 10-13, 2014.
2. Wang, Q., Chen, T., Chang, F.F., Al Nasser, W., et al.: "Iron Sulfide Scale Dissolver for Downhole Application: Where Are We Now?" SPE paper 184513, presented at the SPE International Conference on Oil Field Chemistry, Montgomery, Texas, April 3-5, 2017.
3. Wang, Q., Chen, T., Chang, F., Al-Nasser, W., et al.: "Searching for Iron Sulfide Scale Dissolver for Downhole Applications," paper presented at the CORROSION 2018, Phoenix, Arizona, April 15-19, 2018.
4. Buali, M., Ginest, N., Leal, J.A., Sambo, O., et al.: "Extreme Challenges in FeS Scale Cleanout Operation Overcome Using Temporary Isolation, High-Pressure Coiled Tubing, and Tailored Fluid Systems," SPE paper 169759, presented at the SPE International Oil Field Scale Conference and Exhibition, Aberdeen, U.K., May 14-15, 2014.
5. Wylde, J.J.: "Sulfide Scale Control in Produced Water Handling and Injection Systems: Best Practices and Global Experience Overview," SPE paper 169776, presented at the SPE International Oil Field Scale Conference and Exhibition, Aberdeen, Scotland, U.K., May 14-15, 2014.
6. Okocha, C., Thornton, A. and Wylde, J.J.: "Novel Sulfide Scale Inhibitor Successfully Averts Challenging Sulfide Scale Deposition in Permian and Williston Unconventional Basins," paper presented at the SPE/AAPG/SEG Unconventional Resources Technology Conference, virtual, July 20-22, 2020.
7. Savin, A., Adamson, B., Wylde, J.J., Kerr, J.R., et al.: "Sulfide Scale Control: A High Efficacy Breakthrough Using an Innovative Class of Polymeric Inhibitors," SPE paper 169777, presented at the SPE International Oil Field Scale Conference and Exhibition, Aberdeen, Scotland, U.K., May 14-15, 2014.
8. Petrozziello, L., Kayser, C., Okocha, C., Chen, T., et al.: "Iron Sulfide Scale Inhibition: Squeeze Life Extension through Improved Interaction between Scale Inhibitor and Rock," SPE paper 200709, presented at the SPE International Oil Field Scale Conference and Exhibition, virtual, June 24-25, 2020.
9. Okocha, C., Sorbie, K.S. and Boak, L.S.: "Novel Inhibition Mechanism for Sulfide Scales," SPE paper 112538, presented at the SPE International Symposium and Exhibition on Formation Damage Control, Lafayette, Louisiana, February 13-15, 2008.

About the Authors

Dr. Cyril Okocha

Ph.D. in Petroleum Engineering, Heriot-Watt University

Dr. Cyril Okocha is a Scientist working at the Clariant Global Innovation and Application Development Center in Houston, TX.

He primarily works as part of the global innovation team that focuses on the development, enhancement and application of novel oil field chemical technologies.

Cyril's research interests include the development and application of novel chemical application technologies, sulfide scale inhibitor development, scale inhibitor squeeze technology, sour gas production, flow assurance, heavy oil production, water treatment technologies, and production enhancement.

He is the author and coauthor of several Society of Petroleum Engineers (SPE) conference papers and patents.

Cyril has a background in Geochemistry from Newcastle University, Newcastle upon Tyne, U.K.

He received his Ph.D. degree in Petroleum Engineering from Heriot-Watt University, Edinburgh, Scotland, U.K.

Dr. Tao Chen

Ph.D. in Chemical Engineering, Heriot-Watt University

Dr. Tao Chen is a Petroleum Engineering Consultant working with the Production Technology Team of Saudi Aramco's Exploration and Petroleum Engineering Center – Advanced Research Center (EXPEC ARC). His interests are production chemistry and flow assurance in the oil and gas industry, specializing in oil field scale management.

Prior to joining Saudi Aramco in 2014, Tao spent more than 15 years on oil field scale management and worked at Clariant, Champion Technologies, Nalco Champion, and LR Senergy in Aberdeen, Scotland, U.K.

He has authored and coauthored over 120 technical publications and 20 U.S. patent applications.

Tao is an active member of the Royal Society of Chemistry (RSC), the Society of Petroleum Engineers (SPE) and the Association for Materials Protection and Performance (AMPP). He has been an active Fellow of the Royal Society of Chemistry (FRSC) since 2018.

Tao received both his B.S. and M.S. degrees in Chemical Engineering from Dalian University of Technology, China, and his Ph.D. degree in Chemical Engineering from Heriot-Watt University, Edinburgh, Scotland, U.K. Tao also received an MBA from Warwick University, Coventry, U.K.

Dr. Alex Thornton

Ph.D. in Applied Chemistry, Heriot-Watt University

Dr. Alex Thornton is the Global Head of Scale Technology at Clariant Oil and Mining Services based in Houston, TX, and manages a specialist scale innovation team focused on the development, enhancement, and application of oil field chemical technologies for local, regional, and global interests, while providing problem solving expertise globally.

He has amassed significant field application experience, both offshore and onshore, for new/novel scale control technologies across the globe, and in his 30 years of industry experience, Alex has been instrumental in enhancing Clariant's reputation as a leader in the scale field.

His research interests include a multitude of scale types, application technologies, support service enhancement, and treatment design optimization.

As the author and coauthor of a number of scale papers, patents, and articles, Alex has covered many topics on new and novel scale control and removal technologies.

He received his Ph.D. degree in Applied Chemistry from Heriot-Watt University, Edinburgh, Scotland, U.K. Following this, Alex spent a short time as a Research Associate, before moving to Clariant Oil and Mining Services (then TROS).

Dr. Qiwei Wang

Ph.D. in Oceanography, Texas A&M University

Dr. Qiwei Wang works in Saudi Aramco's Research & Development Center as a Research Science Consultant. Since joining Saudi Aramco in 2011, he has played a key role in all major scale mitigation activities in companywide operations and led the completion of over 100 projects. Before joining Saudi Aramco, Qiwei worked with Nalco Champion as a R&D Coordinator on flow management and as a Senior Specialist on scale management. He has over 25 years of R&D and technical support experience in oil field production chemistry, scale management, and water treatment.

Qiwei is an active member of the Society of Petroleum Engineers (SPE) and National Association of Corrosion Engineers (NACE). He has organized workshops, served on technical committees, and has chaired several conferences for both organizations.

Qiwei is the recipient of the 2021 NACE Technical Achievement Award, in recognition for his sustained and outstanding contributions in technical advancements for oil field scale management.

He has authored and coauthored over 180 publications and 30 U.S. patent applications.

Qiwei received his B.Eng. degree in Chemical Engineering from Taiyuan University of Science and Technology, Taiyuan, China; an M.Eng. degree in Material Sciences from Harbin Institute of Technology, Harbin, China; an M.S. degree in Chemistry from the University of Ryukyus, Okinawa, Japan; and a Ph.D. degree in Oceanography from Texas A&M University, College Station, TX.

Innovative Disorder Seismic Attribute for Reservoir Characterization

Dr. Qiang Fu and Dr. Saleh A. Al-Dossary

Abstract /

Although most of the regions of seismic data usually are stratific, coherent, and continuous, there are areas in seismic data that look chaotic, i.e., high randomness zones. The randomness of seismic data is mainly due to three reasons: (1) energy of random reflections or refractions from certain subsurface geological structures, e.g., fraction zone, gas chimney, karst collapse, and terminated unconformity; (2) suboptimum acquisition and consequential low data quality, e.g., all kinds of noise; and (3) imperfect data processing/imaging procedure, e.g., inaccurate migration velocity, imaging artifacts, and operator aliasing.

Therefore, a reliable method to estimate the spatial distribution of the randomness level in seismic data is essential and indispensable for reservoir characterization. Estimation of randomness spatial distribution with high resolution will assist reservoir characterization in multiple ways, including: (1) identify certain geological features such as: fracture zones, gas chimneys, karst collapse, terminated unconformity or other random reflection/refraction related features; (2) indicate seismic data quality and random noise level, e.g., recognizing boundary problem between merged surveys; and (3) provide covariance matrix for seismic inversion or uncertainty index for interpretation and reservoir simulation.

There have been numerous early attempts at estimating the randomness level in seismic data, among them are cross correlation-based algorithms, structure tensor-based algorithms, gray level co-occurrence matrix (GLCM) based algorithms, etc. Differing from all aforementioned algorithms, the disorder seismic attribute is a convolutional filtering-based algorithm designed using an optimization approach. By design, the attribute is insensitive to faults, channel edges, unconformities, and other linear discontinuities of geological features.

In this article, we demonstrate the application of disorder seismic attribute on three field examples to show the advantages of the disorder seismic attribute over other algorithms.

Introduction

Seismic exploration has been the most important approach for hydrocarbon exploration; it uses seismic energy (data) to probe the subsurface structure and locate potential hydrocarbon reservoirs. Although most of the regions of seismic data are stratific, coherent, and continuous, there are high randomness zones in seismic data that look chaotic. Therefore, the randomness level measurement, especially randomness level spatial distribution estimation, is an essential task in seismic data processing/imaging.

The randomness of seismic data is mainly due to three reasons:

1. The energy of random reflections or refractions from certain subsurface geological structures, e.g., fraction zone, gas chimney, karst collapse, and terminated unconformity.
2. The suboptimum acquisition and consequential low data quality, e.g., all kinds of noise.
3. The imperfect data processing/imaging procedure, e.g., inaccurate migration velocity, imaging artifacts, and operator aliasing.

Subsequently, a reliable method to estimate the spatial distribution of the randomness level in seismic data is essential and indispensable for reservoir characterization. High quality estimation for randomness will assist reservoir characterization in multiple ways, including:

1. Identify certain geological features such as: fracture zones, gas chimneys, karst collapse, terminated unconformity or other random reflection/refraction related features.
2. Indicate seismic data quality and random noise level, e.g., recognizing boundary problem between merged surveys.
3. Provide covariance matrix for seismic inversion or uncertainty index for interpretation and reservoir

simulation.

Numerous attempts have been made at estimating the randomness level in seismic data. Dash and Obaidullah (1970)[1] proposed to use cross correlation to describe noise for seismic traces. Their approach is similar to early coherence algorithms and doesn't work well in faulted areas because faults are accentuated over randomness. Bahorich and Farmer (1995)[2] extended the cross correlation technique and developed the first coherence attribute to highlight discontinuities in exploration seismic data. Randen et al. (2001)[3] introduced the chaos attribute based on structure tensor, which is an eigen analysis of a 3 × 3 gradient component covariance matrix.

High chaos values indicate low data directionality. Similar to eigen coherence, this method is used mainly for fault extraction rather than noise description. In zones near fault planes, seismic data are discontinuous in one direction and continuous in other directions. Faults may also be associated with fracture zones; therefore, local randomness measures may be useful for identifying fracture zones, although this capability has not been tested.

Consequently, all aforementioned methods seem ill suited for distinguishing faults from data randomness. The gray level co-occurrence matrix (GLCM) based algorithms are from a neural network approach[4-6]. The co-occurrence matrix can distinguish the energy from coherent patterns (lines, curves, blocks, etc.) and from chaotic areas. Based on this matrix, the GLCM entropy is calculated and it can estimate the level of randomness in the data. A large value means a higher randomness level in the seismic data and vice versa.

Al-Dossary et al. (2014)[7] proposed a disorder seismic attribute that differs from its forerunners. The method is based on a convolutional filtering method and uses a second order differential operator designed using an optimization approach, which is sensitive to a chaotic and noisy areas, but not an organized area. We will see this optimization procedure next, and then we will understand why it is only sensitive to chaotic and noisy areas. By design, the disorder seismic attribute is insensitive to faults, channel edges, unconformities, and other linear discontinuities of geological features.

One potential issue of disorder seismic attribute is its amplitude sensitivity, meaning it is affected by the amplitude of input data and will produce low values for a chaotic zone with low amplitude in seismic data. To compensate this issue, Chopra and Marfurt (2016)[8] proposed to scale the disorder seismic attribute value by the root mean squarer (RMS) amplitude in a sliding window in the input data to mitigate the amplitude sensitivity issue.

Theory

Al-Dossary et al. (2014)[7] derive the disorder filter based on an optimization procedure, which removes simple non-random structures such as constant values, slope, and axial steps. For the 3D seismic data cube, a 3D disorder filter will be a 3D convolutional filter. Assuming the randomness energy has a zero mean, this filter will have zero sum of all its coefficients. From the symmetry along the axial directions, the coefficients of this filter should be axisymmetric. And since horizontal or vertical constant values, slope, and steps are non-random features, they should yield zero output of this filter. Therefore, the summation of each column or row of the coefficients of this filter is zero.

Now let's follow at how to determine the coefficients of a 3 × 3 × 3 3D disorder filter — a larger filter size is possible but is usually unnecessary and computational expensive, so 3 × 3 × 3 is a normal size for 3D disorder filter. A general 3 × 3 × 3 3D filter has 27 coefficients and using the symmetric property previously mentioned, only four unique coefficients need to be specified, while the remaining are predetermined by symmetry. The four unique to-be-determined coefficients are: (1) a, at the filter center; (2) b, at six face centers; (3) c, at 12 edge centers; and (4) d, at eight filter vertices.

The 3D disorder filter with to-be-determined coefficients is illustrated in pictorial form as:

$$\left[\begin{bmatrix} d & c & d \\ c & b & c \\ d & c & d \end{bmatrix}, \begin{bmatrix} c & b & c \\ b & a & b \\ c & b & c \end{bmatrix}, \begin{bmatrix} d & c & d \\ c & b & c \\ d & c & d \end{bmatrix}\right] \quad (1)$$

The summation of the coefficients from each column or row should be zero, which guarantees to filter out the non-random structures in the input data, such as constant values, constant slopes, and steps in axial directions.

This leads to another set of linear equations:

$$\begin{cases} a + 2b = 0 \\ b + 2c = 0 \\ c + 2d = 0 \end{cases} \quad (2)$$

This linear equation set is undetermined. To solve this issue, the coefficient d can be arbitrarily set to avoid fraction coefficient, and then the solution becomes:

$$\begin{cases} a = -8 \\ b = 4 \\ c = -2 \\ d = 1 \end{cases} \quad (3)$$

In pictorial form, the 3D disorder filter is:

$$\left[\begin{bmatrix} 1 & -2 & 1 \\ -2 & 4 & -2 \\ 1 & -2 & 1 \end{bmatrix}, \begin{bmatrix} -2 & 4 & -2 \\ 4 & -8 & 4 \\ -2 & 4 & -2 \end{bmatrix}, \begin{bmatrix} 1 & -2 & 1 \\ -2 & 4 & -2 \\ 1 & -2 & 1 \end{bmatrix}\right] \quad (4)$$

Because the sign of the filtered data is not significant in randomness estimation, we define the power of the filtered value as the disorder seismic attribute. Alternatively, the absolute value may be used if preferred.

Chopra and Marfurt (2016)[8] proposed one extra step to attenuate the input amplitude sensitivity of the disorder filter by scaling the disorder value by the RMS amplitude in the vicinity of the sample location of the input data:

$$\textbf{disorder} = \frac{u}{\bar{d} + \varepsilon} \quad (5)$$

where u is the unscaled disorder attribute value, $\tilde{d}$ is the RMS amplitude in a sliding window in the vicinity of the sample location of the input data, and ε is a small additive constant that prevents division by zero in the computations.

Examples

Next, we demonstrate the application of disorder seismic attribute on three field examples to show the advantages of a disorder seismic attribute over other algorithms.

Example 1

Figure 1 shows a seismic section with noise estimated using the classic trace correlation method[1], the chaos seismic attribute, and disorder seismic attribute (this study). Several faults are clearly visible in the seismic section, Fig. 1a. The correlation approach and chaos attribute mainly identify those faults rather than the randomness. In contrast, the disorder seismic attribute, in this thin fault case, is not strongly influenced by the existence of faults.

Figure 2 illustrates the same data in a 3D view. The near surface is very noisy as indicated by high disorder values; the middle is less random. In this example, the disorder seismic attribute, Fig. 2c, is better at extracting

Fig. 1 *(a) A vertical slice of the input seismic amplitude volume. This slice shows several large, easily visible faults; (b) the noise attribute using trace correlation technique[1]; (c) the chaos attribute; and (d) the disorder seismic attribute. In this example, disorder is less influenced by faulting and better indicates the randomness of the input data.*

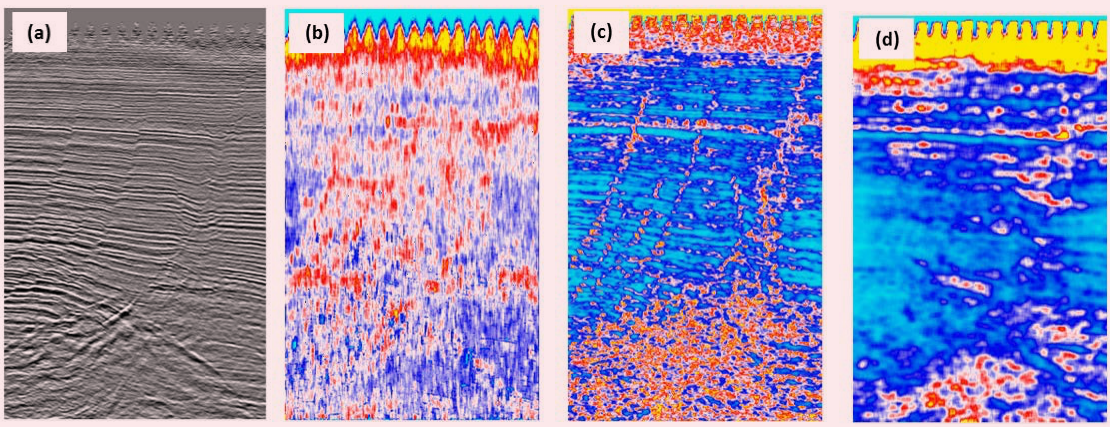

Fig. 2 *A 3D view of the same data shown in Fig. 1. The correlation noise and chaos attributes are more strongly influenced by faulting compared to disorder.*

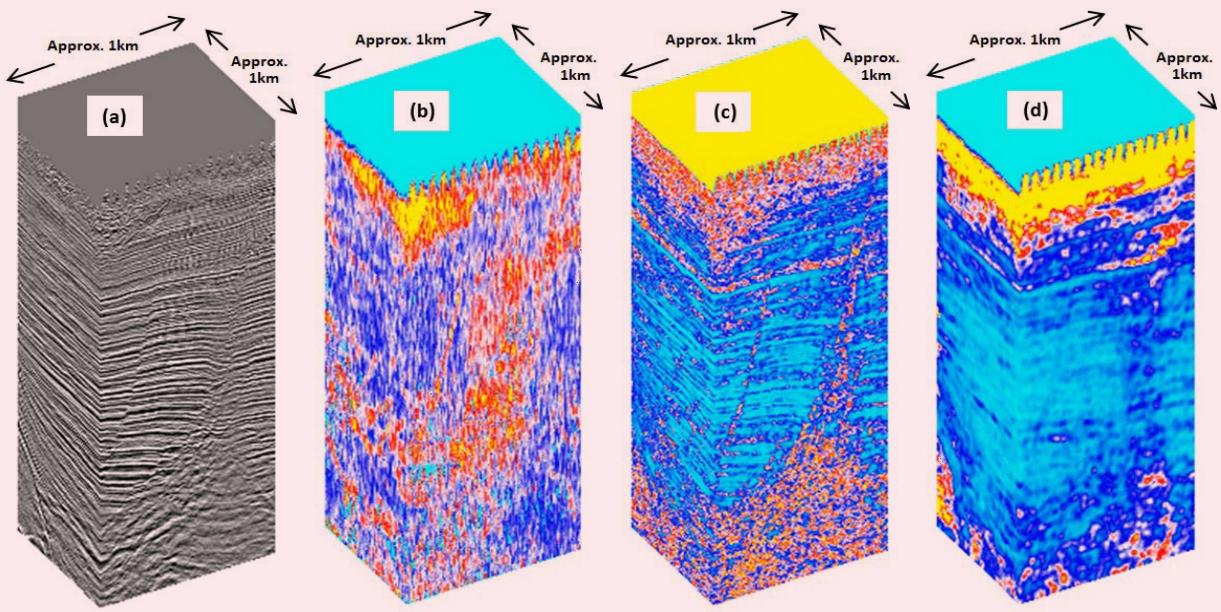

randomness than either correlation noise, Fig. 2a, or chaos attributes, Fig. 2b.

Example 2

Figure 3 displays a horizontal section of a geologically complex area. High disorder values (green ellipse) correspond to a weak signal-to-noise ratio, and low values (purple ellipse) are associated with strong reflectors. The circled vertical column of high disorder (white ellipse) hints at a possible gas chimney.

This attribute may help interpreters assess the reliability of data and derived attributes, as well as indicate geologic features such as gas chimneys or large-scale fracture zones. We observe that the disorder seismic attribute sometimes relates to faults or channel systems.

Figure 4 shows such an example. A survey boundary and a channel system are visible in both the disorder, Fig. 4a, and dip-guided edge attributes, Fig. 4b.

Example 3

Figure 5a shows an interpreted time structure map of a horizon in a marine seismic exploration survey. The missing picks (two blank holes) in the southern part are due to two salt domes. Figures 5b to 5d shows corresponding coherence, GLCM entropy, and disorder attributes, respectively, extracted along the horizon.

Figure 6 shows the corresponding vertical slices of seismic amplitude, coherence, GLCM entropy, and disorder attribute along cross-section AA'.

Note that the coherence highlights faults and other discontinuities, but fails to delineate the very hard-to-pick region between two salt domes. For this data volume, GLCM entropy is so sensitive to textural difference that it misleadingly considers easy-to-pick areas as noisy. Only the disorder attribute correctly represents the horizon picking confidence. By construction, it is also insensitive to faults.

Fig. 3 *A horizontal section of a geologically complex area: (left) the seismic amplitude volume; (right) the disorder attribute volume. Low disorder values (purple ellipse) correspond to strong reflectors, and high disorder values are related to noise (green ellipse). The vertical column of high disorder value (white ellipse) hints at a possible gas chimney.*

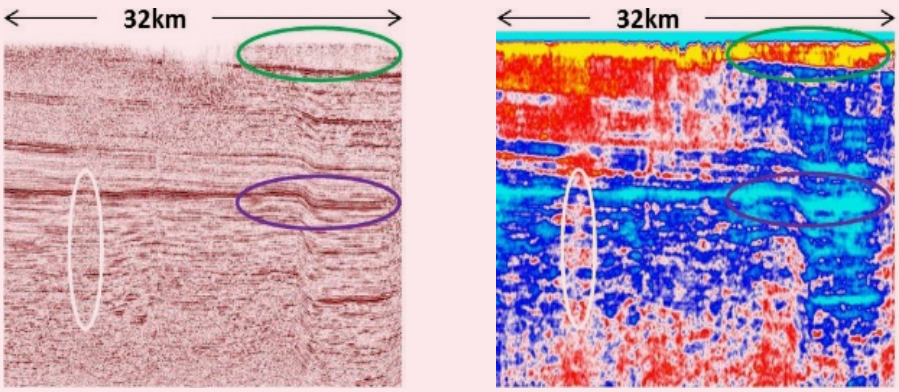

Fig. 4 *The disorder seismic attribute (a) illustrates features similar to dip-guided edge detection (b). An acquisition survey boundary (green ellipse) and a channel system (blue ellipse) are visible in both the disorder and edge detection plots.*

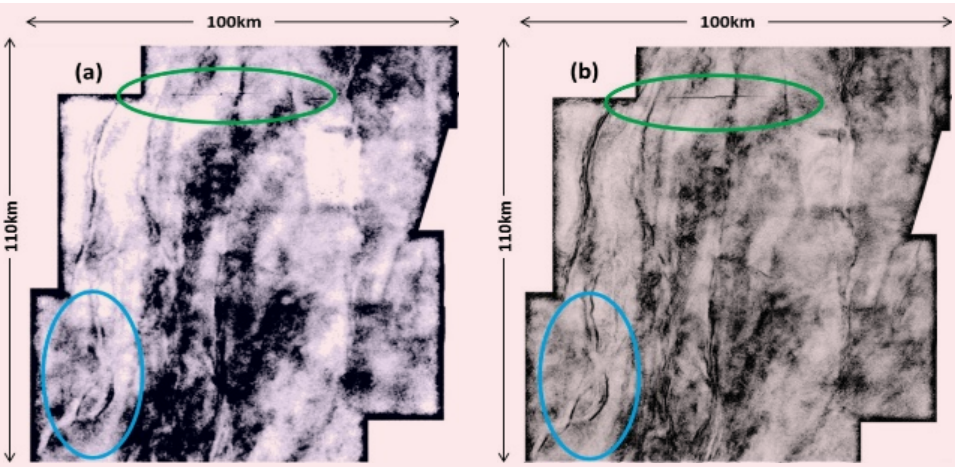

Fig. 5 *(a) An interpreted time structure map of a horizon in a marine seismic exploration survey; (b) A horizon slice through coherence, delineating the faults as well as noise in the northern part of the survey; (c) A horizon slice through the GLCM entropy volume showing easy-to-pick areas as having low entropy; and (d) A horizon slice through the disorder volume.*

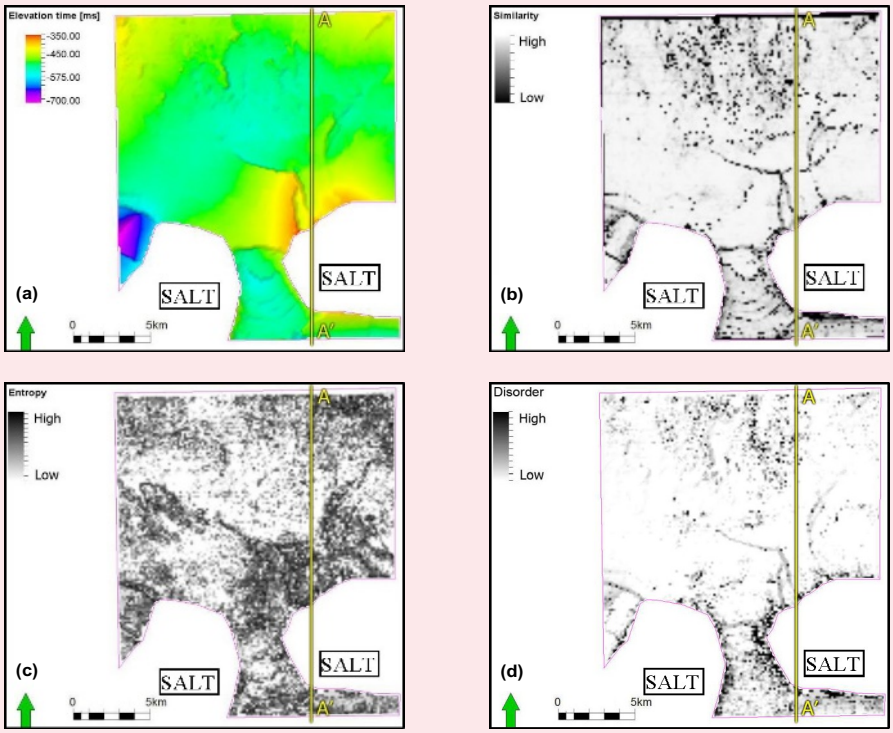

Fig. 6 *(a) The vertical slice AA′ through the amplitude volume; and (b) The vertical slice AA′ through the coherence volume. Note both the salt and a mass transport complex (MTC) appear with low coherence. Several faults are also highlighted; (c) The vertical slice AA′ through the GLCM entropy volume; and (d) The vertical slice AA′ through the disorder volume. Note that the two faults are no longer highlighted.*

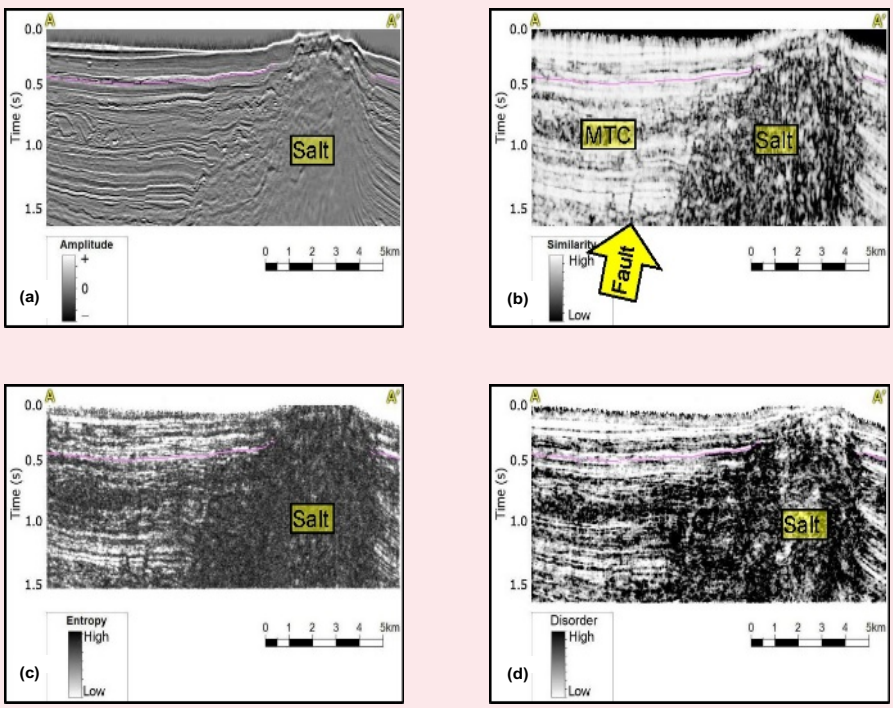

Conclusions

Disorder is a powerful innovative seismic attribute that estimates the spatial distribution of data randomness. It can assist reservoir characterization by: (1) Identifying certain geological features such as fracture zones, gas chimneys, karst collapse, terminated unconformity or other random reflection/refraction related features; (2) Indicating seismic data quality and random noise level; and (3) Providing covariance matrix for seismic inversion or uncertainty index for interpretation and reservoir simulation.

Disorder attribute is superior than other algorithms in estimating spatial distribution of randomness in seismic data for it is less biased by faults, channel edges, unconformities, and other linear discontinuities of geological features.

References

1. Dash, B.P. and Obaidullah, K.A.: "Determination of Signal and Noise Statistics Using Correlation Theory, *Geophysics*, Vol. 35, Issue 1, February 1970, pp. 24-32.
2. Bahorich, M. and Farmer, S.: "3D Seismic Discontinuity for Faults and Stratigraphic Features: The Coherence Cube," *The Leading Edge*, Vol. 14, Issue 10, October 1995, pp. 1053-1058.
3. Randen, T., Pedersen, S.I. and Sønneland, L.: "Automatic Extraction of Fault Surfaces from Three-Dimensional Seismic Data," *SEG Technical Program Expanded Abstracts 2001*, pp. 551-554.
4. West, B.P., May, S.R., Eastwood, J.E. and Rossen, C.: "Interactive Seismic Facies Classification Using Textural Attributes and Neural Networks," *The Leading Edge*, Vol. 21, Issue 10, October 2002, pp. 1042-1049.
5. Gao, D.: "Volume Texture Extraction for 3D Seismic Visualization and Interpretation," *Geophysics*, Vol. 68, Issue 4, July 2003, pp. 1294-1302.
6. Chopra, S. and Alexeev, V.: "Applications of Texture Attributes to 3D Seismic Data," *CSEG Recorder*, Vol. 30, Issue 7, September 2005, pp. 28-32.
7. Al-Dossary, S., Wang, Y.E. and McFarlane, M.: "Estimating Randomness Using Seismic Disorder," *Interpretation*, Vol. 2, Issue 1, February 2014, pp. SA93-SA97.
8. Chopra, S. and Marfurt, K.J.: "Understanding the Seismic Disorder Attribute and its Applications," *The Leading Edge*, Vol. 35, Issue 8, August 2016, pp. 695-702.

About the Authors

Dr. Qiang Fu

Ph.D. in Physics, University of Houston

Dr. Qiang Fu is a Geophysicist working in the Geophysical Applications Division of Saudi Aramco's Exploration Application Services Department (EASD). His current focus is on developing new innovative algorithms to solve emerging challenging issues in field exploration production.

Qiang started his career with the Geophysical Team in Saudi Aramco's Exploration and Petroleum Engineering Center – Advanced Research Center (EXPEC ARC). After participating in several research projects, he decided to pursue postgraduate degrees in the U.S. to improve his research skills. After successfully receiving two degrees and completing postdoctoral research experience in academia, Qiang returned to Saudi Aramco and joined his current department.

He is the author of several technical papers and three pending patents. Qiang also serves as the Patent Innovation Coordinator in EASD.

He is an active member of the Society of Exploration Geophysicists (SEG) and has served as a technical reviewer and technical program section chairman for multiple SEG annual conferences.

In 2012, Qiang received his M.S. degree in Geophysics from Stanford University, Stanford, CA, and in 2016, he received his Ph.D. degree in Physics from the University of Houston, Houston, TX.

Dr. Saleh A. Al-Dossary

Ph.D. in Geophysics, University of Houston

Dr. Saleh A. Al-Dossary works in Saudi Aramco's Exploration Application Services Department, developing new seismic processing and attributes algorithms.

He holds 10 patents, and has filed an additional five patents in seismic detection technology.

Saleh is a member of the Society of Exploration Geophysicists (SEG), the European Association of Geoscientists and Engineers (EAGE) and the Dhahran Geosciences Society (DGS). He is the author and coauthor of several articles published by the SEG.

Saleh received the Outstanding Student Award from the University of Houston in 2003, and a Saudi Aramco Excellence Award in 2015.

In 1991, he received his B.S. degree in Computer Science with a minor in Geophysics from the New Mexico Institute of Mining and Technology, Socorro, NM. Saleh received his M.S. degree in 1997 from Stanford University, Palo Alto, CA, and in 2004, he received his Ph.D. from the University of Houston, Houston, TX, both in Geophysics.

Have an article you would like to publish? Here are our guidelines.

These guidelines are designed to simplify and help standardize submissions. They need not be followed rigorously. If you have any questions, please call us.

Length

Average of 2,500-4,000 words, plus illustrations/photos and captions. Maximum length should be 5,000 words. Articles in excess will be shortened.

What to send

Send text in Microsoft Word format via email. Illustrations/photos should be clear and sharp. Editable files are requested for graphs, i.e., editable in Excel.

Procedure

Notification of acceptance is usually within three weeks after the submission deadline. The article will be edited for style and clarity and returned to the author for review. All articles are subject to the company's normal review. No paper can be published without a signature at the manager level or above.

Format

No single article need include all of the following parts. The type of article and subject covered will determine which parts to include.

Working Title
Lorem Ipsum here.

Abstract
Usually 150-300 words to summarize the main points.

Introduction
Different from the abstract in that it sets the stage for the content of the article, rather than telling the reader what it is about.

Main body
May incorporate subtitles, artwork, photos, etc.

Conclusion/Summary
Assessment of results or restatement of points in introduction.

Endnotes/References/Bibliography
Use only when essential. Use author/date citation method in the main body. Numbered footnotes or endnotes will be converted. Include complete publication information. Standard is *The Associated Press Stylebook*, 52nd ed. and *Wesbter's New World College Dictionary*, 5th ed.

Acknowledgments
Use to thank those who helped make the article possible.

Illustration/Tables/Photos and explanatory text

If the files are large, these can be submitted separately, due to email size limits. Initial submission may include copies of originals; however, publication will require the originals. When possible, submit original images. Color is preferable.

File Format

Illustration files with .EPS extensions work best. Other acceptable extensions are .TIFF/.JPEG/.PICT.

Permission(s) to reprint, if appropriate

Previously published articles are acceptable but can be published only with written permission from the copyright holder.

Author(s)/Contibutor(s)

Please include a brief biographical statement.

Submission/Acceptance Procedures

Papers are submitted on a competitive basis and are evaluated by an editorial review board comprised of various department managers and subject matter experts. Following initial selection, authors whose papers have been accepted for publication will be notified by email.

Papers submitted for a particular issue but not accepted for that issue may be carried forward as submissions for subsequent issues, unless the author specifically requests in writing that there be no further consideration.

Submit articles to:

Editor
The Saudi Aramco Journal of Technology
C-10B, Room AN-1080
North Admin Building #175
Dhahran 31311, Saudi Arabia
Tel: +966-013-876-0498
Email: *william.bradshaw.1@aramco.com.sa*

Submission deadlines

Issue	Paper submission deadline	Release date
Spring 2023	November 7, 2022	March 31, 2023
Summer 2023	February 1, 2023	June 30, 2023
Fall 2023	May 9, 2023	September 30, 2023
Winter 2023	August 3, 2023	December 31, 2023

There is more.

Fracture Permeability Estimation Under Complex Physics: A Data-Driven Model Using Machine Learning

Xupeng He, Marwah M. AlSinan, Dr. Hyung T. Kwak and Dr. Hussein Hoteit

Abstract / The permeability of fractures, including natural and hydraulic, are essential parameters for the modeling of fluid flow in conventional and unconventional fractured reservoirs. Traditional analytical (Cubic Law-based) models used to estimate fracture permeability show unstable performance when dealing with different complexities of fracture cases. This work presents a data-driven, physics included model based on machine learning as an alternative to traditional methods.

The workflow for the development of the data-driven model includes four steps.

Electric Submersible Pump Design Enhancements for H_2S Harsh Environments

Mohammed A. Al-Khalifah, Rui F. Pessoa and Derek M. Sinclair

Abstract / The electric submersible pump (ESP) remains the preferred artificial lift method for high rate production when technically viable. ESPs, on the other hand, are sensitive to downhole conditions and pumped fluid. Sour fields, in particular, are considered a major challenge for producing facilities and well completion elements. Reservoirs producing fluids with hydrogen sulfide (H_2S) present a special challenge to ESP systems.

A New Oriented Perforation Strategy for Hydraulic Fracturing Treatment in Deep and Tight Reservoirs

Dr. Kaiming Xia, Dr. Yufeng Cui and Dr. Tariq Mahmood

Abstract / Hydraulic fracture initiation can be a challenging issue for fracturing deep and tight gas reservoirs, which generally requires a high breakdown pressure for clustered perforation hydraulic fracturing treatment. Oriented perforation represents a potential solution to this issue, which can not only lower breakdown pressure but also deliver a better oriented fracture geometry.

In this article, we present a new strategy to tackle this issue, which includes a framework to calculate the optimum perforation direction, and a new perforation cluster layout design. The optimum perforation direction is defined as the one, along which hydraulic fractures can be initiated with the lowest breakdown pressure for a perforation cluster. It can be used to control the perforation device rotating and fired in the right direction in the subsurface. Further, we present a new perforation cluster layout design, which can alleviate the near wellbore fracture tortuosity and deliver a better fracture initiation when it is aligned along the optimum perforation direction in the subsurface.

To read these articles and others, go to www.saudiaramco.com/jot

أرامكو السعودية
saudi aramco

Aramco
Journal
of Technology

Liked this issue? Sign up. It's free.

To begin receiving the *Aramco Journal of Technology* please complete this form, scan and send by email to ***william.bradshaw.1@aramco.com.***

Got questions?

Just give us a call at +966-013-876-0498 and we'll be happy to help!

Scan the QR code to go straight to your email and attach the form!

Subscription Form

Name

Title

Organization

Address

City

State/Province

Postal code

Country

Email address

Phone number

Number of copies